

UCSF

UC San Francisco Electronic Theses and Dissertations

Title

Structural Characterization of Nucleotide Driven Morphological Changes of TubZ Filaments

Permalink

<https://escholarship.org/uc/item/1rz1c0ns>

Author

Montabana, Elizabeth Ann

Publication Date

2013

Peer reviewed|Thesis/dissertation

Structural Characterization of Nucleotide Driven Morphological
Changes of TubZ Filaments

by

Elizabeth A. Montabana

DISSERTATION

Submitted in partial satisfaction of the requirements for the degree of

DOCTOR OF PHILOSOPHY

in

Biophysics

in the

GRADUATE DIVISION

of the

UNIVERSITY OF CALIFORNIA, SAN FRANCISCO

Copyright 2013

by

Elizabeth Montabana

Acknowledgements

I could not have accomplished the bulk of the work presented here without the help of large number of people. First and foremost, I would like to acknowledge past and present members of the Agard lab, whose camaraderie and intellectual prowess have fueled me for the long days, months and years of graduate school – from debates over Electron Microscopy to off-topic journal club presentations to the competitive nature of lab potluck food, I have been privileged to interact with such an amazing set of people. Thank you.

I had an amazing group of mentors in the lab, starting with Dr. Luke Rice and Dr. Michelle Moritz as rotation advisors, who introduced me to the wonderful world of tubulin with skill and sarcasm. Dr. Dan Southworth was a patient advisor for all things biochemistry, and he inspired many of the experiments that were done in this dissertation. I am extremely indebted to Dr. Justin Kollman, for teaching me what I could absorb about electron microscopy and helical reconstruction, pioneering the technique in lab. Without his help and guidance, this work would contain dramatically different experiments and conclusions. Michael Braunfeld and Drs. Rebeca Choy, Sam Li, Xueming Li, Shawn Zhang, and Agustin Avila-Sakar have all provided both good conversations and assistance in running the electron microscope and in understanding data processing, an important component of the research I have done during my time at UCSF. Another important group of people to whom I am indebted is my colleagues working on the bacterial cytoskeleton, including Dr. Jessica Polka formerly of the Mullins lab at UCSF for discussions and protocols, Dr. Marcy Erb and Dr. Joe Pogliano at UCSD for both discussions and materials, as well as for getting me started on the TubZ project to start with, and James Kraemer and Elena Zehr, for ideas, information, and companionship about prokaryotic tubulins. I also

need to thank Joyce Ramponi and Mariano Tabios for keeping me in line, keeping the lab functioning, and for providing essential life advice.

Not to be forgotten is Dr. David Agard, my graduate advisor. David is a true scientist who always strives for the best – whether it is for a more complete story, or the perfect color scheme in a figure, or even for a superior EM camera. It has been inspirational to work with him. Additionally I need to thank Dr. John Gross and Dr. Wallace Marshall, the other members my thesis committee for enthusiasm and ideas. Dr. Yifan Cheng and Dr. Dyche Mullins were also helpful for discussions about EM or the prokaryotic cytoskeleton, respectively.

On a more personal note, I'd like to thank the friends I have made while I've been at UC San Francisco – Hesper Rego, who was my first friend here, for delicious baking nights. Rebeca Choy, Laura Lavery, and Elaine Kirschke, thanks for always being there for with a shoulder to whine on or a buddy to drink with. David Booth, with whom I had some marvelous times teaching middle school students about skulls, bacteria and the forces in an egg drop. I also need to give a shout out to the Folsom Lake Crew for their debauchery and good times.

Of course, I also need to thank my family, old and new. Thanks to my parents for decades of support and patience, and bringing me up in a science friendly environment. Finally, I need to thank my husband, Stephen – thank you for sticking with me through tears and manic work hours, for your encouragement, for tolerating my wild food experiments, dirty dishes, and for countless discussions about science, even when you think I'm not listening. I'm looking forward to many exciting years ahead with the new challenges and joys that the future will bring.

One chapter of this dissertation has been previously published by the National Academy of Sciences and is reprinted here with permission. Chapter 2 originally appeared in the *Proceedings of the National Academy of Science of the United States of America* 105(14), 5378-831 (2008). Thanks also to Mariano Tabios for contributing to this work.

Abstract:

The tubulin superfamily is a unique set of GTPases, which, while they have high sequence diversity, have remarkably similar tertiary structures. These proteins share a very conserved longitudinal interface, but are able to form a surprisingly wide variety of super structures within both eukaryotic and prokaryotic cells – from the familiar 13- protofilament microtubule assembled from $\alpha\beta$ -tubulin heterodimers to the single protofilaments of the ubiquitous prokaryotic FtsZ seen *in vitro*. Additionally in eukaryotes, monomeric tubulin family members have the ability to affect the assembly of filaments, such as nucleation of microtubules with γ -tubulin, or involvement in the assembly of B- and C- microtubules in the centriole microtubule triplets (ϵ - and δ -tubulin respectively). Each tubulin family member, both prokaryotic and eukaryotic is exquisitely tuned to perform its cellular function, with a unique superstructure and dynamics.

The main focus of this manuscript is a structural and biochemical investigation of a recently discovered bacterial tubulin TubZ-Bt. TubZ-Bt is located on the pBtoxis virulence plasmid in *Bacillus thuringiensis*, and is necessary to maintain stability of the pBtoxis plasmid in conjunction with an upstream DNA-adaptor protein (TubR) and DNA-binding site (*tubC*). We have determined that TubZ-Bt forms four-stranded filaments in the presence of GTP *in vitro*, whereas TubZ filaments formed with catalytically compromised protein or non-hydrolysable GTP analogs are predominantly two-stranded. These morphological changes were investigated by high-resolution cryo-electron microscopy of both two- and four-stranded TubZ-Bt filaments, as well as various biochemical approaches, and we propose that TubZ-Bt two-stranded filaments that we observed are an intermediate on pathway to four-stranded filament formation. In addition, we have begun preliminary

investigations on the interaction of TubR bind to *tubC* DNA and the interaction of the TubRC complex with TubZ-Bt filaments.

A minor focus of this manuscript is work on the eukaryotic tubulins, γ -, δ - and ϵ -tubulin. This work details preliminary attempts at purification of these tubulin family members in order to begin more detailed investigative work on their molecular function. Also included is a published manuscript of work done with Dr. Luke Rice investigating the conformational state of both $\alpha\beta$ - and γ -tubulins using solution-state and crystallographic structural studies.

TABLE OF CONTENTS

<i>Title Page</i>	<i>i</i>
<i>Acknowledgements</i>	<i>iii</i>
<i>Abstract</i>	<i>vi</i>
<i>Table of Contents</i>	<i>viii</i>
<i>List of Tables</i>	<i>xi</i>
<i>List of Figures</i>	<i>xi</i>
CHAPTER 1: INTRODUCTION	1
REFERENCES	11
CHAPTER 2: THE LATTICE AS ALLOSTERIC EFFECTOR: STRUCTURAL STUDIES OF $\alpha\beta$- AND γ-TUBULIN CLARIFY THE ROLE OF GTP IN MICROTUBULE ASSEMBLY	17
ABSTRACT	18
AUTHOR CONTRIBUTIONS	19
INTRODUCTION	20
RESULTS	23
DISCUSSION	27
ACKNOWLEDGEMENTS	30
FIGURES	32
METHODS	38
REFERENCES	41
SUPPLEMENTARY INFORMATION	46

CHAPTER 3: INITIAL STUDIES ON THE EXPRESSION AND PURIFICATION OF RECOMBINANT	
MONOMERIC TUBULIN FAMILY MEMBERS γ-TUBULIN, δ-TUBULIN AND	
ϵ-TUBULIN	60
INTRODUCTION	61
RESULTS & DISCUSSION	63
METHODS	67
FIGURES	71
REFERENCES	84
CHAPTER 4: BACTERIAL TUBULIN TUBZ-BT TRANSITIONS BETWEEN A TWO-STRANDED	
INTERMEDIATE AND A FOUR-STRANDED FILAMENT UPON	
GTP HYDROLYSIS	86
ABSTRACT	87
INTRODUCTION	87
RESULTS	90
DISCUSSION	99
MATERIALS & METHODS	104
ACKNOWLEDGEMENTS	105
FIGURES	106
REFERENCES	111
SUPPLEMENTARY INFORMATION	114

CHAPTER 5: COMPLEMENTARY EXPERIMENTS TOWARDS UNDERSTANDING TUBZ-BT

FILAMENT FORMATION	134
INTRODUCTION	135
RESULTS & DISCUSSION	136
METHODS	143
FIGURES	150
REFERENCES	164

CHAPTER 6: INITIAL STUDIES INTO THE INTERACTION OF TUBZ-BT FILAMENTS WITH

TUBRC CENTROMERIC ADAPTOR COMPLEX	166
INTRODUCTION	167
RESULTS & DISCUSSION	168
METHODS	175
FIGURES	180
REFERENCES	192

CHAPTER 7: FUTURE DIRECTIONS

INTRODUCTION	194
MONOMERIC EUKARYOTIC TUBULINS	194
TOWARDS AN UNDERSTANDING OF THE PLASMID SEGREGATION SYSTEM TUBZRC	196
REFERENCES	203

LIST OF TABLES:

CHAPTER 2:

CRYSTALLOGRAPHIC DATA AND REFINEMENT	58
RMSD STATISTICS FOR STRUCTURAL SUPERPOSITIONS OF PREVIOUS TUBULIN STRUCTURES ONTO THE TWO γ -TUBULIN:GDP STRUCTURES	59

CHAPTER 3

PERCENT SIMILARITY BETWEEN DIFFERENT MEMBERS OF THE HUMAN TUBULIN FAMILY	71
---	----

CHAPTER 5

COMPARISON OF RESULTS OF MODELING TUBZ-BT NUCLEATION USING DIFFERENT METHODS	151
RESULTS OF MUTAGENESIS OF INTERFACIAL AND TAIL RESIDUES OF TUBZ-BT	155

LIST OF FIGURES:

CHAPTER 2:

TWO CONFORMATIONS OF $\alpha\beta$ -TUBULIN, AND CONFLICTING MODELS FOR THE ROLE OF GTP	32
STRUCTURAL FEATURES OF γ -TUBULIN:GDP	33
THE AFFINITY OF $\alpha\beta$ -TUBULIN FOR ALLOCOLCHICINE DOES NOT DEPEND ON NUCLEOTIDE STATE	34

SMALL ANGLE X-RAY SCATTERING SHOWS THAT $\alpha\beta$ -TUBULIN:GTP AND $\alpha\beta$ -	
TUBULIN:GDP ADOPT ESSENTIALLY IDENTICAL CURVED CONFORMATIONS	35
IMPLICATIONS FOR THE KINETICS OF MT INITIATION	36
CORRECTED CHAIN TRACE FOR THE C-TERMINAL A-HELIX	50
LATERAL INTERACTIONS IN THE γ -TUBULIN:GDP CRYSTAL REVEAL STRIKING	
ADAPTABILITY	51
ALLOCOLCHICINE FLUORESCES WHEN BOUND TO $\alpha\beta$ -TUBULIN	52
THE STRAIGHT AND CURVED CONFORMATIONS OF β -TUBULIN PRESENT THE GTP	
REQUIRED FOR ASSEMBLY IN DIFFERENT STRUCTURAL CONTEXTS	53
$\alpha\beta$ -TUBULIN STRAIGHTENING PROBABLY OCCURS INCREMENTALLY WITH SUCCESSIVE	
LATERAL EXTENSIONS	55
NUCLEATORS THAT MIMIC THE MICROTUBULE POLYMER SHOULD ALSO OVERCOME THE	
ANTAGONISTIC EFFECT OF THE CONFORMATIONAL STRAIN THAT OPPOSES LATERAL	
ASSEMBLY	57

CHAPTER 3:

MODELING OF THE INSERTIONS IN δ - AND ϵ -TUBULIN ONTO THE STRUCTURE OF γ -	
TUBULIN	71
NUCLEOTIDE BINDING IN γ -TUBULIN	72
INITIAL OVER-EXPRESSION AND PURIFICATION TESTS OF <i>S. CEREVISIAE</i> γ -TUBULIN	
HOMOLOG TUB4P IN <i>E. COLI</i>	73
INITIAL TEST PREP OF TUB4P-PET29B	74
ANALYSIS OF TUB4P-PET29B TEST PREP	75

4L BATCH PURIFICATION OF TUB4P-PET29B	76
TEST PREP OF TUB4P-PET29B WITH USE OF MONOQ	77
DENATURING TUB4P-PET29B PREP	78
PREP OF HIS-TAGGED TUB4P FROM BACULOVIRUS	79
OVER-EXPRESSION OF HIS-TAGGED δ - AND ϵ -TUBULIN IN PBAD EXPRESSION	
VECTOR	80
TEST PURIFICATION OF HIS-TAGGED δ - AND ϵ -TUBULIN IN PBAD EXPRESSION	
VECTOR	81
	82
δ -TUBULIN PURIFICATION TRIALS	83
PURIFICATION FROM BACULOVIRUS CONSTRUCTS	

CHAPTER 4:

CHANGES IN TUBZ-BT FILAMENT MORPHOLOGY AND BEHAVIOR IN THE PRESENCE OF	106
TERMINAL TAGS	
MORPHOLOGY OF TUBZ-GTP FOUR-STRANDED FILAMENTS AND TWO-STRANDED	107
FILAMENTS	108
COMPARISON OF LONGITUDINAL FITS OF ATOMIC MODELS OF TUBZ	
THE C-TERMINAL TAIL OF TUBZ IS IMPORTANT FOR ASSEMBLY OF BOTH TUBZ	109
FILAMENT MORPHOLOGIES	110
MODEL OF THE POLYMERIZATION MECHANISM OF TUBZ	120
MORPHOLOGY OF TAGGED AND UNTAGGED TUBZ-BT	121
ANALYSIS OF THE FOUR-STRANDED FILAMENT RECONSTRUCTION	

ANALYSIS OF THE TWO-STRANDED FILAMENT RECONSTRUCTION	123
COMPARISON OF THE INTERACTIONS OF THE TWO AND FOUR-STRANDED INTERFACES	125
COMPARISON OF THE LATERAL INTERACTIONS OF THE TWO- AND FOUR-STRANDED PROTOFILAMENTS	127
MUTANTS TO LATERAL FOUR-STRANDED INTERFACE MAINLY AFFECT FOUR-STRANDED FILAMENT FORMATION	128
DIFFERENCE MAPS OF FOUR- AND TWO-STRANDED FILAMENT RECONSTRUCTIONS	129
HIGHLIGHTING LOCATION OF C-TERMINAL TAIL DENSITY	130
TRUNCATIONS OF THE C-TERMINAL TAIL DO NOT AFFECT FILAMENT MORPHOLOGY	131
ANALYSIS OF CRYO-EM DATA COLLECTION	132

CHAPTER 5:

TUBZ-BT:GTPrS NEGATIVE STAIN EM REVEALS 2, 3 AND 4 STRANDED FILAMENTS	150
AFFECTS OF NON-HYDROLYZABLE GTP ANALOGS ON TUBZ-BT	151
MODELING OF TUBZ-BT NUCLEATION VIA THE FLYVBJERG MODEL	152
DESIGN OF MUTANTS TO TEST FILAMENT INTERFACES	153
NS ELECTRON MICROGRAPHS OF SELECT INTERFACIAL MUTANTS	154
TUBZ-BT FILAMENT FORMATION IN DIFFERENT PH CONDITIONS	156
COUPLED REGENERATIVE GTPASE ASSAY TO DETERMINE GDP RELEASE RATE	157
TUBZ-BT WITH CFP TAG ON THE C-TERMINUS IN THE PRESENCE OF GTP	158

TUBZ-BT WITH CFP TAG ON THE C-TERMINUS IN THE PRESENCE OF GTP γ S	159
PRELIMINARY RESULTS FROM MINI- <i>BACILLUS SUBTILIS</i> EXPRESSING TUBZ-BT	160
PRELIMINARY LIGHT MICROSCOPY OF TUBZ-BT FLUORESCENTLY LABELED FILAMENTS	161
PURIFICATION OF TUBZ-BM WITH CLEAVABLE GST-TAG	162
NEGATIVE STAIN EM OF TUBZ-BM + GTP γ S	163

CHAPTER 6:

PURIFICATION OF N-TERMINALLY HIS-TAGGED TUBR	180
MALS OF TUBR INDICATING IT IS A DIMER IN SOLUTION	181
GEL SHIFT ASSAY OF SHORT OLIGONUCLEOTIDES OF THE ITERON SEQUENCES	181
BINDING OF VARIOUS LENGTHS OF OLIGONUCLEOTIDES OF THE ITERON SEQUENCES	182
MALS DETERMINING NUMBER OF TUBR DIMERS BOUND TO DIFFERENT <i>TUBC</i> OLIGONUCLEOTIDES	183
GEL SHIFT ASSAY OF TUBR BINDING TO LONGER <i>TUBC</i> OLIGONUCLEOTIDES	183
NEGATIVE STAIN EM OF TUBR DIMERS BINDING TO 48 OR 60 BASE PAIR <i>TUBC</i>	184
NEGATIVE STAIN EM OF TUBR DIMERS BINDING TO 48 BP <i>TUBC</i>	185
NEGATIVE STAIN EM OF TUBR DIMERS BINDING TO LONGER <i>TUBC</i> DNA	186
DIAGRAM OF THE SEQUENCE SURROUNDING <i>TUBC</i>	187
CO-PELLETING TUBZ-BT WITH THE TUBRC COMPLEX	188
CO-PELLETING OF UNTAGGED TUBZ-BT WITH TUBRC COMPLEX	189

STIMULATION OF UNTAGGED TUBZ-BT POLYMERIZATION WITH TUBRC-60MER	
COMPLEX	190
INITIAL ATTEMPTS AT CHARACTERIZING THE TUBRC-TUBZ FILAMENT	
INTERACTION	191

Chapter 1
Introduction

The interiors of cells, both eukaryotic and prokaryotic can be thought of as a well-choreographed dance, where the dancers (DNA, RNA and protein) are dynamic entities that move in time with specific purpose and motion upon the stage. In real life, the directions of the choreographer are often marked off on stage with tape in order to help dancers reliably locate the positions that they need to be when they need to be there. In order for the cell to orchestrate its dancers it also needs to be able to leave markers to help locate these dancers within its confines.

This happens in the cell mainly with the assistance of protein scaffolds, with the most prominent type of scaffold being the cell cytoskeleton. Cell cytoskeleton components are fibrous in nature, consisting of several subclasses of molecules - the most familiar and proliferous being actin, tubulin and intermediate filaments. These molecules form large structures in the cell that are observable with just a light microscope, and their fibers have been observed for several centuries (1). These molecules provided structure to the cell - organizing organelles, allowing for transport of cellular cargoes, positioning DNA during mitosis, and facilitating cell motility.

Breaking the analogy of choreography however, is the important fact that the proteins of the cell cytoskeleton are not only markers for location of other proteins during the cell cycle, but are also highly dynamic proteins themselves. These proteins are able to arrange and rearrange depending on need, and also to generate necessary force in both mitosis and cell movement.

The tubulin family is one of the major classes of cytoskeletal proteins, and has been found to exist in both in both eukaryotes and prokaryotes. Tubulin family members have varying conservation levels among and within organisms. However, they all share a three-

dimensional fold, consisting of a globular N-terminal GTP binding domain connected to a globular C-terminal activation domain by an extended helix (known in the literature as H7) (2). The GTP binding pocket on the N-terminal domain is the most conserved element including the tubulin signature sequence [GGGTG(S/T)G]. Additionally, the catalytic loop (T7) on the C-terminal domain has a conserved GxxNx₂DxxD/E, including a conserved aspartate/glutamate, which is necessary for GTP hydrolysis. In addition to these core elements and structure being conserved, the longitudinal interface at which tubulin monomers interact is highly conserved (2). Other regions on tubulins can be highly variable, including large loop insertions (including helices H11-H12 in $\alpha\beta$ -tubulin which forms a necessary binding interface, but is missing in prokaryotic tubulins), extended n-termini and extended c-termini. The variability of the c-terminus is quite high, probably due to this region being used as a binding site for various protein cofactors (3-5).

Among eukaryotes, tubulin family members are quite conserved, among both paralogs and orthologs, with sequence identity among α - and β -tubulins being >75% across species (6). γ -Tubulin is also well conserved and is found in all eukaryotes and is necessary for microtubule nucleation(7). Additionally there are newly discovered monomeric tubulin family members including δ - and ϵ -tubulin, which are found in most species that have microtubule triplets in their centrioles, with a notable exception of members of the *Drosophila* genus(8). α -, β -, γ -, δ -, and ϵ -tubulin all fall within a range of 35-70% similar in sequence to each other(9).

In contrast to the conserved nature of eukaryotic tubulins with each other, the sequence similarity between eukaryotic and prokaryotic tubulins is quite low (discussed in (10)). In preliminary research on the most common prokaryotic tubulin, the ubiquitous

FtsZ, it was unknown based on sequence alone whether it was indeed a tubulin homolog (11), as the similarity between sequences was quite low (10-20%). It was not until the structures of both $\alpha\beta$ -tubulin and FtsZ were solved that there was a definitive answer. Among prokaryotes, FtsZ itself is fairly well conserved, (40-50%) (10). Relatively recently, other members of the tubulin family have been identified in prokaryotes, including a dimer pair BtubA and BtubB found in *P. dejongeii* (12, 13), the TubZ family of proteins which are involved in low-copy number plasmids segregation (14-17), and the newly discovered phage tubulin family (PhuZ) (18, 19) which seems to be responsible for centering phage particles (19). These new representatives of the tubulin super family are as divergent from each other as they are from FtsZ and eukaryotic tubulins.

The other divergent aspect of members of the tubulin family is the diverse range of superstructures that they are able to form. $\alpha\beta$ -Tubulin forms the important and abundant microtubule, which are typically 13 protofilaments *in vivo* but can range from 11-18 protofilaments *in vitro* (20). The structure of FtsZ *in vivo* is unknown, but it can form sheets, and single protofilaments that can be both curved and straight. BtubA/B forms five-stranded filaments (21), while TubZ is able to form two-, three-, and four-stranded filaments (15, 22, 23). PhuZ has recently been found to form three stranded filaments with the c-terminus in the lumen of the filament, where as all other have the c-terminus on the outside of the filament (Zehr EA, et al, in review). Understanding how these divergent tubulin structures are formed has been the concept that has formed the basis of most of the work in this thesis.

The role of nucleotide state in the conformational changes of eukaryotic tubulins

I began my time in the Agard lab working on a structural project with a then postdoctoral scholar in the lab, Dr. Luke Rice. Dr. Rice had been working on understanding a key structural transition of $\alpha\beta$ -tubulin that had been observed in earlier work (24, 25): Microtubule growth and dynamics are critically dependent on the binding and hydrolysis of GTP by β -tubulin, but the prevailing mechanism at the time posited that the state of nucleotide bound to the exchangeable site of free $\alpha\beta$ -tubulin dimer controlled an allosteric switch between 'straight'(GTP) and 'curved'(GDP) conformations (26). Dr. Rice and then graduate student Hector Aldaz were able to purify and crystallize human γ -tubulin, solving the structure bound to GTP and GTP γ S (27). They observed that unlike the structure of GTP-bound $\alpha\beta$ -tubulin solved by 2D electron crystallography (24), the GTP and GTP γ S structures were in a 'curved' conformation (27). This led them to hypothesis that instead of acting as an allosteric effector, the GTP γ -phosphate directly enhances longitudinal interactions in the lattice, providing sufficient binding energy needed to overcome the curved to straight transition. In order to show this, Dr. Rice monitored the solution state of GTP and GDP $\alpha\beta$ -tubulin by small angle x-ray scattering. We observed that the two scattering curves appeared to indicate they were in the same conformation, and that there were more similar to a modeling of the curved crystal structure. In addition, Dr. Rice monitored binding of allocolchicine to $\alpha\beta$ -tubulin bound to GTP or GDP. If GTP-binding led to a 'straight' conformation, binding to allocolchicine would be sterically hindered. However, we observed that allocolchicine binding was identical in the presence of either GTP or GDP. To complement these studies, I was able to crystallize human γ -tubulin in the presence of GDP, and solve the structure to a resolution of 2.3 Å, as well as playing a role in refining of the crystal structure. The crystal structure revealed that γ -tubulin:GDP has a

virtually identical conformation to that of γ -tubulin:GTP. The results of these studies have been published in the journal PNAS (28) and are presented in chapter 2.

Expression and purification of eukaryotic monomeric tubulins

As a follow up to these studies and others done earlier in the lab by Dr. Michelle Moritz (29, 30), we wished to further investigate the role of nucleotide binding pocket in γ -tubulin function. Since our studies indicated that the conformation change of γ -tubulin was not affected by GTP binding or hydrolysis (27, 28), it was unclear whether these functions were necessary for the nucleating role that γ -tubulin plays for microtubules. Because both $\alpha\beta$ - and γ -tubulin bind and hydrolyze GTP it has not been possible to separately analyze the functional importance of the γ -tubulin nucleotide state, in order to decouple the two nucleotide binding and hydrolysis events, we wished to create mutants of γ -tubulin that would have altered nucleotide specificity via chemical genetics (precedent for altering nucleotide specificity had been established through work on kinases (31) and other GTPases, such as Eftu (32)). As a preliminary step towards this, we wished to establish a protocol for purifying yeast γ -tubulin from an *E. coli* expression system. Using various techniques we attempted to accomplish this, to an unsuccessful end. These efforts are outlined in chapter 3.

While attempting to purify soluble γ -tubulin from *E. coli*, I became interested in two other monomeric tubulins δ - and ϵ -. Deletions of δ -tubulin in *C. reinhardtii* cause a centriolar defect in which the centrioles lose the C-tubule of the microtubule triplets to become doublets (33), while ϵ -Tubulin mutations in *C. reinhardtii* cause a phenotype in which only shortened singlet microtubules form (34). I was interested in understanding

what role these two tubulins could have in controlling the polymeric superstructure of centrioles. I wished to pursue investigation of these biochemically, structurally, and also to do immunoprecipitation studies to locate binding partners. The first step in these studies was to establish protocols to purify soluble recombinant versions of human δ - and ϵ -tubulin. We received cDNA as a gift from Dr. Tim Stearns at Stanford University. We first tried to do this via an *E. coli* system, which did not provide promising results. Attempts at purifying them from a baculovirus/insect cell expression system seemed to hold promise, but were halted before all tests could be done. The results of these efforts are also outlined in chapter 3.

TubZ-Bt forms transitional two-stranded filaments on pathway to stable four-stranded filament

In addition to the study of eukaryotic tubulins, our lab took an interested in investigating interesting new prokaryotic tubulins through a nascent collaboration with the lab of Dr. Joe Pogliano at the University of California, San Diego. His lab had recently investigated the *in vivo* function of a newly discovered tubulin family member TubZ (14). TubZ proteins, of which several have recently been identified are involved in the segregation of low copy number plasmids (17, 35) or pseudo-lysogens (15). I wished to follow up on the research that the Pogliano lab had accomplished, and began work on a TubZ from the pBtoxis virulence plasmid found in *B. thuringiensis*. TubZ-Bt is a 54 kDa protein with low sequence identity (<20%) to both eukaryotic tubulins and FtsZ, or even other members of the TubZ family. Initially we attempted both crystallography and electron microscopy in order to probe the structural nature of this filament forming protein. During these attempts,

several papers on the *in vitro* structure and biochemistry of TubZ were published (22, 23, 36). Through negative stain EM we were able to observe that *in vitro* TubZ-Bt filaments grown in the presence of GTP form almost exclusively four-stranded filaments, whereas TubZ filaments formed with catalytically compromised protein or non-hydrolysable GTP analogs are predominantly two-stranded. These results showed that the filament conformation is linked to nucleotide state. To understand this nucleotide driven transition, I used cryo-EM to reconstruct both two- and four-stranded filaments, using the technique of iterative helical real space refinement (IHRSR) pioneered by Dr. Ed Egelman (37). I was able to reconstruct the four-stranded filament to ~ 7 Å resolution and the two-stranded filament to a ~ 11 Å resolution. This allowed us to make a pseudo-atomic model using previously solved crystal structures. In addition to the pseudo-atomic model, we were able to probe the importance of N- and C-terminal residues by tagging and truncation. Even relatively small tags on the N-terminus have detrimental effects on the ability of TubZ-Bt to polymerize, while tags on the C-terminus have only a slight dampening affect. Of even greater interest is that even slight truncation of only 14 residues of the C-terminal region, which is predicted to be mostly unstructured, has a dramatic affect on polymerization ability. Removal of 42 residues lowers the polymerization to a negligible amount. These residues were all missing from the current set of crystal structures, so their role is not understood. Analysis of the cryo-EM reconstructions suggests that this region may be binding along the two-stranded filament, but seems to be absent in the four-stranded filament. This, along with other data, has led us to hypothesis that the two-stranded filament form is on pathway to the formation of a more stable four-stranded filament, which is an unprecedented mechanism of polymerization. A full summary of these results is

presented in chapter 4.

Further results regarding TubZ-Bt filament formation and kinetics

In addition to the work presented in chapter 4, many different experiments were conducted to explore TubZ-Bt filament formation and understand its kinetics. These results were not presented in conjunction with chapter 4, either because they were tangential to results, or because they need to be followed up in more detail. These results include, but are not limited to, modeling of TubZ-Bt filament nucleation, GDP release assays of both two- and four-stranded filament forms, attempts to locate the C-terminal region of TubZ-Bt by GFP tagging, and initial purifications of a second member of the TubZ protein family, TubZ from *B. megaterium*. These various uncategorized results are contained within chapter 5.

Role of TubRC DNA binding complex in TubZ-Bt filament formation

TubZ-Bt and other known cytoskeletal elements (Other TubZs, ParM, ParA) that segregate plasmids, are members of 3-component systems. The other components are a DNA binding protein, and a centromeric region of DNA, which often contains palindromic or repeating elements (38). TubZ-Bt is found with a DNA adaptor protein known as TubR, a winged helix-turn helix protein, which binds to a centromeric region, *tubC*, which consists of 7 pseudo-repeats binding sequences (36, 39). In order to understand the mechanism by which TubZ-Bt filaments are able to segregate plasmids, we wished to explore and structural and biochemical understanding of both TubR binding to *tubC* DNA as well as the interaction of the TubRC complex to TubZ filaments. We were able to visualize binding of

TubR dimers to *tubC* DNA by negative stain EM, revealing that TubR binds cooperatively along extended pieces of DNA. The TubRC complex does not appear to have any discrete conformation. In addition, we were able to see that the TubRC complex is able to stimulate TubZ filament growth in presence of both GTP and GTP γ S, a result that has since been published by another group (39). Although we were able to see binding by both gel shift assay as well as pelleting, our attempts so far have not led to a clear visualization of TubRC complex binding to TubZ filaments. The results of these efforts are summarized in chapter 6.

Future directions for the study of tubulin family members

The tubulin family of proteins has been identified for quite sometime (2, 11, 40, 41), and much progress has been made to understand their kinetics and function *in vivo* and *in vitro*. Two major challenges exist to a full and detailed understanding of these proteins. One challenge that exists is applicable mainly to the field of eukaryotic tubulin family members, which is that of stability and manipulability of these proteins in an *in vitro* environment. New developments in this field (42, 43) are already starting to give us new insight into the function of $\alpha\beta$ -tubulin. Progress in the future may be made on purifying δ - and ϵ -tubulin (as well as other even more specialized monomeric tubulins) by using cell-free systems, baculovirus, or human cell lines. Another challenge is the mesoscale nature of polymer formation. Understanding small intermediates in filament formation, as well as understanding the nature of interactions to form complicated structures such as the FtsZ contractile ring or assembly of the centriole, is hampered by the limitations of techniques that make these either too small or too large to visualize. As techniques such as AFM,

electron microscopy, and super-resolution light microscopy improve, they hopefully will be able to shed light on these processes (44-46). The future is bright for a detailed understanding of how the tubulin family of cytoskeletal functions.

References

1. Frixione E (2000) Recurring views on the structure and function of the cytoskeleton: a 300-year epic. *Cell Motil Cytoskeleton* 46(2):73-94 .
2. Nogales E, Downing KH, Amos LA, & Lowe J (1998) Tubulin and FtsZ form a distinct family of GTPases. *Nat Struct Biol* 5(6):451-458 .
3. Buske PJ & Levin PA (2012) Extreme C terminus of bacterial cytoskeletal protein FtsZ plays fundamental role in assembly independent of modulatory proteins. *J Biol Chem* 287(14):10945-10957 .
4. Little M & Seehaus T (1988) Comparative analysis of tubulin sequences. *Comp Biochem Physiol B* 90(4):655-670 .
5. Serrano L, de la Torre J, Maccioni RB, & Avila J (1984) Involvement of the carboxyl-terminal domain of tubulin in the regulation of its assembly. *Proc Natl Acad Sci U S A* 81(19):5989-5993 .
6. Fyngson DK, Needleman DJ, & Sneppen K (2004) Variability-based sequence alignment identifies residues responsible for functional differences in alpha and beta tubulin. *Protein Sci* 13(1):25-31 .
7. Wiese C & Zheng Y (1999) Gamma-tubulin complexes and their interaction with

- microtubule-organizing centers. *Curr Opin Struct Biol* 9(2):250-259 .
8. McKean PG, Vaughan S, & Gull K (2001) The extended tubulin superfamily. *J Cell Sci* 114(Pt 15):2723-2733 .
 9. Inclan YF & Nogales E (2001) Structural models for the self-assembly and microtubule interactions of gamma-, delta- and epsilon-tubulin. *J Cell Sci* 114(Pt 2):413-422 .
 10. Erickson HP (2007) Evolution of the cytoskeleton. *Bioessays* 29(7):668-677 .
 11. Mukherjee A, Dai K, & Lutkenhaus J (1993) Escherichia coli cell division protein FtsZ is a guanine nucleotide binding protein. *Proc Natl Acad Sci U S A* 90(3):1053-1057 .
 12. Jenkins C, *et al.* (2002) Genes for the cytoskeletal protein tubulin in the bacterial genus *Prostheco bacter*. *Proc Natl Acad Sci U S A* 99(26):17049-17054 .
 13. Schlieper D, Oliva MA, Andreu JM, & Lowe J (2005) Structure of bacterial tubulin BtubA/B: evidence for horizontal gene transfer. *Proc Natl Acad Sci U S A* 102(26):9170-9175 .
 14. Larsen RA, *et al.* (2007) Treadmilling of a prokaryotic tubulin-like protein, TubZ, required for plasmid stability in *Bacillus thuringiensis*. *Genes Dev* 21(11):1340-1352 .
 15. Oliva MA, Martin-Galiano AJ, Sakaguchi Y, & Andreu JM (2012) Tubulin homolog TubZ in a phage-encoded partition system. *Proc Natl Acad Sci U S A* 109(20):7711-7716 .
 16. Tang M, Bideshi DK, Park HW, & Federici BA (2007) Iteron-binding ORF157 and FtsZ-like ORF156 proteins encoded by pBtoxis play a role in its replication in *Bacillus thuringiensis* subsp. *israelensis*. *J Bacteriol* 189(22):8053-8058 .

17. Tinsley E & Khan SA (2006) A novel FtsZ-like protein is involved in replication of the anthrax toxin-encoding pXO1 plasmid in *Bacillus anthracis*. *J Bacteriol* 188(8):2829-2835 .
18. Aylett CH, Izore T, Amos LA, & Lowe J (2013) Structure of the tubulin/FtsZ-like protein TubZ from *Pseudomonas* bacteriophage PhiKZ. *J Mol Biol* 425(12):2164-2173 .
19. Kraemer JA, *et al.* (2012) A phage tubulin assembles dynamic filaments by an atypical mechanism to center viral DNA within the host cell. *Cell* 149(7):1488-1499 .
20. Sui H & Downing KH (2010) Structural basis of interprotofilament interaction and lateral deformation of microtubules. *Structure* 18(8):1022-1031 .
21. Pilhofer M & Jensen GJ (2013) The bacterial cytoskeleton: more than twisted filaments. *Curr Opin Cell Biol* 25(1):125-133 .
22. Aylett CH, Wang Q, Michie KA, Amos LA, & Lowe J (2010) Filament structure of bacterial tubulin homologue TubZ. *Proc Natl Acad Sci U S A* 107(46):19766-19771 .
23. Chen Y & Erickson HP (2008) In vitro assembly studies of FtsZ/tubulin-like proteins (TubZ) from *Bacillus* plasmids: evidence for a capping mechanism. *J Biol Chem* 283(13):8102-8109 .
24. Lowe J, Li H, Downing KH, & Nogales E (2001) Refined structure of alpha beta-tubulin at 3.5 Å resolution. *J Mol Biol* 313(5):1045-1057 .
25. Ravelli RB, *et al.* (2004) Insight into tubulin regulation from a complex with colchicine and a stathmin-like domain. *Nature* 428(6979):198-202 .
26. Nogales E & Wang HW (2006) Structural mechanisms underlying nucleotide-dependent self-assembly of tubulin and its relatives. *Curr Opin Struct Biol*

- 16(2):221-229 .
27. Aldaz H, Rice LM, Stearns T, & Agard DA (2005) Insights into microtubule nucleation from the crystal structure of human gamma-tubulin. *Nature* 435(7041):523-527 .
 28. Rice LM, Montabana EA, & Agard DA (2008) The lattice as allosteric effector: structural studies of alphabeta- and gamma-tubulin clarify the role of GTP in microtubule assembly. *Proc Natl Acad Sci U S A* 105(14):5378-5383 .
 29. Moritz M, Braunfeld MB, Guenebaut V, Heuser J, & Agard DA (2000) Structure of the gamma-tubulin ring complex: a template for microtubule nucleation. *Nat Cell Biol* 2(6):365-370 .
 30. Moritz M, Braunfeld MB, Sedat JW, Alberts B, & Agard DA (1995) Microtubule nucleation by gamma-tubulin-containing rings in the centrosome. *Nature* 378(6557):638-640 .
 31. Hindley AD, *et al.* (2004) Engineering the serine/threonine protein kinase Raf-1 to utilise an orthogonal analogue of ATP substituted at the N6 position. *FEBS Lett* 556(1-3):26-34 .
 32. Hwang YW & Miller DL (1987) A mutation that alters the nucleotide specificity of elongation factor Tu, a GTP regulatory protein. *J Biol Chem* 262(27):13081-13085 .
 33. Dutcher SK & Trabuco EC (1998) The UNI3 gene is required for assembly of basal bodies of *Chlamydomonas* and encodes delta-tubulin, a new member of the tubulin superfamily. *Mol Biol Cell* 9(6):1293-1308 .
 34. Goodenough UW & StClair HS (1975) BALD-2: a mutation affecting the formation of doublet and triplet sets of microtubules in *Chlamydomonas reinhardtii*. *J Cell Biol* 66(3):480-491 .

35. Tang M, Bideshi DK, Park HW, & Federici BA (2006) Minireplicon from pBtoxis of *Bacillus thuringiensis* subsp. *israelensis*. *Appl Environ Microbiol* 72(11):6948-6954 .
36. Ni L, Xu W, Kumaraswami M, & Schumacher MA (2010) Plasmid protein TubR uses a distinct mode of HTH-DNA binding and recruits the prokaryotic tubulin homolog TubZ to effect DNA partition. *Proc Natl Acad Sci U S A* 107(26):11763-11768 .
37. Egelman EH (2007) The iterative helical real space reconstruction method: surmounting the problems posed by real polymers. *J Struct Biol* 157(1):83-94 .
38. Salje J (2010) Plasmid segregation: how to survive as an extra piece of DNA. *Crit Rev Biochem Mol Biol* 45(4):296-317 .
39. Aylett CH & Lowe J (2012) Superstructure of the centromeric complex of TubZRC plasmid partitioning systems. *Proc Natl Acad Sci U S A* 109(41):16522-16527 .
40. Feit H, Slusarek L, & Shelanski ML (1971) Heterogeneity of tubulin subunits. *Proc Natl Acad Sci U S A* 68(9):2028-2031 .
41. Yi QM & Lutkenhaus J (1985) The nucleotide sequence of the essential cell-division gene *ftsZ* of *Escherichia coli*. *Gene* 36(3):241-247 .
42. Johnson V, Ayaz P, Huddleston P, & Rice LM (2011) Design, overexpression, and purification of polymerization-blocked yeast alpha-tubulin mutants. *Biochemistry* 50(40):8636-8644 .
43. Widlund PO, *et al.* (2012) One-step purification of assembly-competent tubulin from diverse eukaryotic sources. *Mol Biol Cell* 23(22):4393-4401 .
44. Chacko JV, Zanicchi FC, & Diaspro A (2013) Probing cytoskeletal structures by coupling optical superresolution and AFM techniques for a correlative approach. *Cytoskeleton (Hoboken)* .

45. Li X, *et al.* (2013) Electron counting and beam-induced motion correction enable near-atomic-resolution single-particle cryo-EM. *Nat Methods* 10(6):584-590 .
46. Mennella V, *et al.* (2012) Subdiffraction-resolution fluorescence microscopy reveals a domain of the centrosome critical for pericentriolar material organization. *Nat Cell Biol* 14(11):1159-1168 .

Chapter 2

The lattice as allosteric effector: Structural studies of $\alpha\beta$ - and γ -tubulin clarify the role of GTP in microtubule assembly

Luke M. Rice, Elizabeth A. Montabana, David A. Agard

The Department of Biochemistry and Biophysics and the Howard Hughes Medical Institute,

University of California, San Francisco, San Francisco, CA 94158-2517

*This work was previously published in *Proceedings of the National Academy of Science of the United States of America* 105(14), 5378-831 (2008) and is reprinted here with permission.

Abstract

GTP-dependent microtubule polymerization dynamics are required for cell division and are accompanied by domain rearrangements in the polymerizing subunit, $\alpha\beta$ -tubulin. Two opposing models describe the role of GTP and its relationship to conformational change in $\alpha\beta$ -tubulin. The allosteric model posits that unpolymerized $\alpha\beta$ -tubulin adopts a more polymerization competent conformation upon GTP binding. The lattice model posits that conformational changes occur only upon recruitment into the growing lattice. Published data supports a lattice model, but is largely indirect and so the allosteric model has prevailed. We present two independent solution probes of the conformation of $\alpha\beta$ -tubulin, the 2.3 Å crystal structure of γ -tubulin bound to GDP, and kinetic simulations to interpret the functional consequences of the structural data. These results (with our previous γ -tubulin:GTP γ S structure) support the lattice model by demonstrating that major domain rearrangements do not occur in *eukaryotic* tubulins in response to GTP binding, and that the unpolymerized conformation of $\alpha\beta$ -tubulin differs significantly from the polymerized one. Thus, geometric constraints of lateral self-assembly must drive $\alpha\beta$ -tubulin conformational changes, while GTP plays a secondary role to tune the strength of longitudinal contacts within the microtubule lattice. $\alpha\beta$ -Tubulin behaves like a bent spring, resisting straightening until forced to do so by GTP-mediated interactions with the growing microtubule. Kinetic simulations demonstrate that resistance to straightening opposes microtubule initiation by specifically destabilizing early assembly intermediates that are especially sensitive to the strength of lateral interactions. These data provide new insights into the molecular origins of dynamic microtubule behavior.

Author contributions: L.M.R. designed research; L.M.R. and E.A.M. performed research; E.A.M. contributed new reagents/analytic tools; L.M.R. and D.A.A. analyzed data; and L.M.R. and D.A.A. wrote the paper.

Introduction

Microtubules are hollow cylindrical polymers of $\alpha\beta$ -tubulin that are critical for intracellular trafficking and formation of the mitotic spindle required for chromosome segregation during cell division. Although vitally important, the molecular mechanisms underlying dynamic microtubule (MT) behavior are poorly understood. Microtubule assembly requires GTP-bound $\alpha\beta$ -tubulin, and GTP hydrolysis by β -tubulin is required to generate dynamic MTs (reviewed in (1)). Structural studies have demonstrated two extreme conformations of $\alpha\beta$ -tubulin: a “straight” conformation observed in the MT lattice(2), and a “curved” conformation observed in a structure of $\alpha\beta$ -tubulin complexed with colchicine and a stathmin-like domain(3) (Fig. 1). There are two opposing models for the relationship between GTP and conformational change in $\alpha\beta$ -tubulin. The allosteric model (recently reviewed in (4)) postulates that GTP binding to $\alpha\beta$ -tubulin triggers long-range conformational changes yielding a substantially straighter conformation that is pre-structured in solution for lateral interactions (5). The lattice model (6) postulates that in solution, $\alpha\beta$ -tubulin adopts the MT-incompatible, curved conformation independent of nucleotide state. Thus, the conformational changes accompanying straightening are the consequence, not the cause, of lattice assembly. The role of GTP is to tune the strength of the MT lattice contacts (Fig. 1) either directly (the γ -phosphate interacting with conserved residues in the α -tubulin T7 loop), or indirectly (the γ -phosphate directing local restructuring of proximal β -tubulin residues to interact more optimally with α -tubulin). The controversy remains unresolved in large part because most of the evidence for either model is indirect. Here we present new results that argue strongly in favor of the lattice

model. We then use kinetic simulations to show that the lattice model predicts a selective destabilization of critical nucleation intermediates, exaggerating the difficulty of *do novo* polymer initiation.

Because it has not been possible to determine the atomic structure of $\alpha\beta$ -tubulin:GTP, the allosteric model is largely based on electron microscopic observations (e.g. (7)) that showed 'straight' (or, more recently, straighter: (5, 8)) protofilaments in MTs grown from GTP-bound $\alpha\beta$ -tubulin but showed 'curved' assemblies in samples of GDP-bound $\alpha\beta$ -tubulin. Importantly, these data generally derive from large, multi-protofilament assemblies of $\alpha\beta$ -tubulin (5, 9).

Crystallographic studies of $\alpha\beta$ -tubulin and related proteins (3, 10-13) have begun to challenge the allosteric model. The crystal structure of $\alpha\beta$ -tubulin bound to colchicine and a stathmin-like domain provided the first atomic model for the curved conformation (3), revealing that curvature at the heterodimer level was generated by similar domain rearrangements in both α - and β -tubulin subunits, despite GTP being bound to the α -subunit. Our recently reported crystal structure of γ -tubulin:GTP (10) unexpectedly adopted this 'curved' domain arrangement. Multiple crystal structures of more distantly related monomeric bacterial tubulin homologs also showed a 'curved' domain arrangement independent of the nucleotide bound (12, 14, 15) (reviewed in (16)).

Solution experiments have also provided data arguing against nucleotide-dependent conformational changes in unassembled $\alpha\beta$ -tubulin. Colchicine-type ligands destabilize

MTs by binding to a pocket in $\alpha\beta$ -tubulin that is only accessible in the curved, unpolymerized conformation (3). Thus, if straight and curved conformations result from GTP- and GDP-binding, then differences in the affinity of $\alpha\beta$ -tubulin for colchicines should be observed. No such differences have been detected (17). More directly, small-angle X-ray scattering (SAXS), which should be sensitive to differences in domain arrangement failed to detect nucleotide-dependent conformational changes (18).

Unfortunately, the existing evidence is not yet sufficient to unambiguously define which model is correct. The solution data for unpolymerized $\alpha\beta$ -tubulin (SAXS and allocolchicine binding) were for technical reasons performed in the absence of Mg^{2+} known to be critical for proper high-affinity GTP binding. They may therefore have failed to populate the fully active $\alpha\beta$ -tubulin:GTP: Mg^{2+} complex. The bacterial tubulin homologs do not form MTs (19), and in fact do not make MT-like lateral associations at all (13, 20). Therefore, they may not provide a reliable model for any potential linkage between nucleotide state and conformational change required by *eukaryotic* tubulins to form the lateral associations necessary for MT assembly. Finally, without an accompanying GDP-bound structure, it is impossible to assert with confidence that domain rearrangements do not accompany GTP-binding by γ -tubulin.

In this work, we sought to better resolve the nature of potential nucleotide-dependent conformational changes in eukaryotic tubulins by directly studying eukaryotic tubulins. We determined the atomic structure of human γ -tubulin:GDP, and thereby provide the only GTP/GDP pair of eukaryotic tubulin structures. We also used two independent methods,

allocolchicine binding and SAXS -- this time in the presence of Mg^{2+} -- to directly probe the solution conformation of unpolymerized $\alpha\beta$ -tubulin as a function of bound nucleotide. Our results contribute to the rising tide of evidence that, in both γ - and $\alpha\beta$ -tubulin, domain rearrangements do not occur in response to GTP binding. They argue strongly for the lattice model, in which the GTP acts *indirectly* to tune to strength of polymerization contacts. Exploring the potential consequences of this change in perspective with kinetic models reveals that the lattice model predicts unanticipated barriers affecting MT initiation intermediates.

Results

γ -Tubulin:GDP adopts a curved conformation identical to that of γ -tubulin:GTP γ S

γ -Tubulin crystallizes more readily than $\alpha\beta$ -tubulin, allowing us to obtain a new crystal form of γ -tubulin bound to GDP (Table 1; Fig. 2a). These better diffracting crystals (2.3 Å) contain two γ -tubulins in the asymmetric unit (Fig. 2b). The improved resolution allowed us to identify a chain tracing error in our recent GTP γ S structure (10), extending the loop between helices H11 and H12 and shifting the register of the C-terminal helix by three residues (Supplemental Fig. 1). The local structure of the nucleotide binding site and the overall conformation of γ -tubulin:GDP and γ -tubulin:GTP γ S are strikingly similar (overall C_a rmsd 0.78 Å and 0.63 Å for chain A and chain B, respectively) (Fig. 2c). The domain arrangement in the γ -tubulin:GDP structures closely resemble those seen in the γ -tubulin:GTP γ S structure (10) and in the 'curved' $\alpha\beta$ -tubulin crystal structures (Fig. 2c) (3, 11).

Lateral interactions between γ -tubulins are adaptable and are not regulated by nucleotide

A key difference between the bacterial and eukaryotic tubulins is the ability to form MT-like lateral interactions. Lateral interactions similar to those that we observed in the γ -tubulin:GTP γ S crystal (10) are again present in the γ -tubulin:GDP crystals despite different crystal packing (Sup. Fig. 2). This indicates that MT-like lateral interactions between γ -tubulin monomers can occur independent of nucleotide state (Sup. Fig. 2).

Our γ -tubulin structures clearly indicate that γ -tubulin does not undergo curved-straight domain rearrangements in response to its nucleotide state. This lack of nucleotide-linked domain rearrangements in monomeric tubulins is consistent with the behavior of prokaryotic tubulin homologs (12-15), and distinguishes this family of proteins from signaling GTPases that are known to switch conformation in response to nucleotide state. This distinction likely arises because the tubulin fold is quite different from that of the switching GTPases, lacking cognates of the P-loop and switch regions that respond to nucleotide state (21, 22). To rule out the possibility that these monomeric tubulins behave differently from heterodimeric $\alpha\beta$ -tubulin, we sought methods capable of reporting on the solution conformation of $\alpha\beta$ -tubulin in the absence of any higher-order self-assembly.

Allocholchicine binding is conformation-dependent, but allocholchicine affinity is independent of nucleotide state.

Colchicine-type drugs are MT depolymerizers that bind in an open cleft between α - and β -tubulin that becomes substantially occluded in the straight conformation (3) (Figure 3a,b). If GTP binding to β -tubulin were to alter the balance between straight and curved $\alpha\beta$ -tubulin conformations, measurable nucleotide-dependent differences in the colchicine binding affinity should result. We used allocolchicine, a well-characterized colchicine analog (23, 24) to address this question. A study performed before the $\alpha\beta$ -tubulin:colchicine structure was determined had attempted to identify the colchicine binding site by examining the effect of allocolchicine binding on the dissociation of $\alpha\beta$ -tubulin into subunits(17). This work indicated that allocolchicine binds $\alpha\beta$ -tubulin with identical affinity when either GTP or GDP is bound, but unfortunately Mg^{2+} was omitted because it affected the dissociation of $\alpha\beta$ -tubulin into subunits and therefore represented a confounding factor (25). To eliminate the possibility that omitting Mg^{2+} resulted in an artificial failure to observe a nucleotide-dependent change in affinity, we performed similar experiments with Mg^{2+} present. The slow GTPase rate of colchicine-bound $\alpha\beta$ -tubulin(26) and the ease of GDP exchange (27, 28) combine to make measurements with GTP possible. Equilibrium binding curves for $\alpha\beta$ -tubulin:allocolchicine binding in the presence of 1mM GTP or 1mM GDP and 1 mM Mg^{2+} are shown in Fig. 3c. The measured affinity of $\alpha\beta$ -tubulin for allocolchicine (GTP: 0.79 ± 0.15 mM, GDP: 0.74 ± 0.15 mM) is independent of the nucleotide bound to $\alpha\beta$ -tubulin. Thus, any nucleotide-dependent conformational changes that might occur in $\alpha\beta$ -tubulin cannot involve domain rearrangements that would significantly alter the curvature of the heterodimer. To better specify the actual solution conformation of unpolymerized $\alpha\beta$ -tubulin, we turned to solution X-ray scattering.

SAXS profiles for $\alpha\beta$ -tubulin:GTP and $\alpha\beta$ -tubulin:GDP are essentially identical and indicative of the curved conformation

SAXS provides a sensitive probe of the solution conformation, and has recently been used to answer questions about conformation and conformational change in other molecular systems (29-31). We predicted SAXS intensity profiles using structures representative of curved(3) and straight(2) conformations of $\alpha\beta$ -tubulin (Fig. 4a). There is a significant fraction (~6%) of missing atoms in the $\alpha\beta$ -tubulin models used to generate the calculated data (see Methods), so we also calculated a SAXS profile from a more complete model for the curved conformation that has the γ -tubulin structure in place of a- and b-tubulin (see Methods). These predictions show small but significant differences over a large part of the experimentally accessible scattering range (Fig. 4a). By working at relatively low $\alpha\beta$ -tubulin concentrations and by using buffer and temperature conditions that do not promote assembly, we were able to measure SAXS profiles for GTP- or GDP-bound $\alpha\beta$ -tubulin in the presence of 1 mM MgCl_2 (Fig. 4a). Our results confirm and extend the earlier studies performed in the absence of Mg^{2+} (18). The intensity profiles and their associated pair distance probability functions ($P(r)$) (Fig. 4b) reveal that $\alpha\beta$ -tubulin does not undergo detectable curved-straight domain rearrangements in response to nucleotide. Direct fitting of the SAXS intensity curves indicates that our data are best modeled by the most complete heterodimer in a curved conformation (purple curve, Fig. 4c), closely followed by the curved $\alpha\beta$ -tubulin conformation. Our SAXS analysis, the allocolchicine affinity, and the predominance of the curved conformation in all structures of monomeric tubulins or bacterial homologs (10, 12-15) together strongly argue for the lattice model, in which a

curved conformation of the $\alpha\beta$ -tubulin heterodimer dominates independent of the nucleotide bound to β -tubulin.

Discussion

$\alpha\beta$ -Tubulin has a unique structural property compared to monomeric tubulins: curvature at the monomer level is amplified within the heterodimer. The coupling of quaternary organization to otherwise unfavorable structural transitions within each monomer implies that the $\alpha\beta$ -tubulin heterodimer essentially behaves like a bent spring, resisting the straightening required to align lateral interaction surfaces (Fig. 1). The lattice model argues that GTP acts *in trans*, strengthening longitudinal interactions and thereby providing sufficient binding energy to recruit and straighten (via lateral interactions) the unpolymerized, curved $\alpha\beta$ -tubulin heterodimer (Fig. 1, Fig. 5, Sup. Fig. 4). GDP-mediated longitudinal contacts are presumably too weak to overcome the energetic barrier required to straighten the curved, unpolymerized heterodimer. The default, curved conformation of $\alpha\beta$ -tubulin also means that the GTP so critical for assembly is presented in different structural contexts for addition at opposite ends of the microtubule (Sup. Fig. 4). The intrinsic asymmetry of the curved conformation thus provides a structural rationale that begins to answer a longstanding question: why do microtubule plus and minus ends show different dynamic behavior and growth kinetics despite having identical affinities for unpolymerized subunits (32).

By specifying that the unpolymerized conformation of $\alpha\beta$ -tubulin differs significantly from the polymerized one, the lattice model implies that the MT lattice itself, and not the

nucleotide, is the allosteric effector. The lattice model predicts that, because a pre-straightened MT lattice does not exist during initiation, lateral interactions will be selectively disadvantaged. Indeed, during an elongation step only **one** $\alpha\beta$ -tubulin must straighten, but to establish a new MT lattice one or more associations in which **two** $\alpha\beta$ -tubulin heterodimers must simultaneously straighten to permit lateral association (Fig. 5a).

We performed kinetic simulations to explore the functional consequences of these conformational changes for MT initiation. MT assembly displays hallmarks (prolonged lag phase preceding rapid assembly) typical of so-called nucleation-elongation kinetic mechanisms (33), wherein the rate of polymer formation depends on the concentration of *nuclei*: rare, energetically unfavorable oligomers of the polymerizing subunits. Although a biochemically correct kinetic description of MT initiation does not yet exist, we explored the consequences of our observations using a simple nucleation-elongation kinetic model (see Methods) that captures essential features of polymer initiation kinetics. To account for the destabilization of early intermediates that we predict result from the lattice model, we lowered the efficiency of the early ‘nucleation’ steps (see Fig. 5c and Methods). The model predicts that dramatic changes in assembly behavior result from quite modest changes in apparent affinity. For example, a nucleus of size 4 and a straightening penalty DG_{straight} of as little 1.6kT (~ 1 kcal/mol) results in a ~ 10 -fold increase in the time required to reach 10% polymerized (Fig. 5d, red and black curves). The extreme sensitivity to nucleation means that even a modest straightening cost should significantly decrease the rate of assembly (Fig. 5d). Furthermore, the open lattice structure of the MT suggests that *multiple*

nucleation intermediates will require this 'double straightening' and therefore that the associated energetic cost will be incurred multiple times (e.g. Figs. 5b,c, reactions with red arrows), producing a dramatic multiplicative effect as the number of steps increase (Fig. 5e).

By assuming that $\alpha\beta$ -tubulin adopts *only* the fully curved or the fully straight conformation, we chose the simplest possible model to explore the kinetic implications of assembly-dependent conformational change. Our demonstration that the conformation of unpolymerized $\alpha\beta$ -tubulin:GTP:Mg²⁺ is curved, along with EM or AFM results showing assembly/disassembly intermediates with partial curvature (5, 8, 9, 34), support the idea that straightening occurs incrementally in response to multiple lateral associations (Sup. Fig 5). In general terms, progressive straightening means that the wider the assembly, the more the curved heterodimer initiating a new lateral layer must straighten. The energetic cost of straightening could therefore manifest itself differently for intermediates of different width. Some partial straightening could potentially occur in response to longitudinal self-association, but the fact that partially curved $\alpha\beta$ -tubulin assemblies nearly always have at least two protofilaments has made this difficult to determine unambiguously. We have focused on the role of lateral assembly because full straightening is typically only observed after tubulin assemblies are multiple protofilaments wide. A full understanding of the allosteric mechanisms at work in $\alpha\beta$ -tubulin assembly that can integrate these concepts into a quantitative understanding of MT assembly dynamics represents a major challenge for the future.

The general requirement that subunits change conformation for self-assembly selectively exaggerates the difficulty of polymer initiation and represents an unanticipated force that should reduce the likelihood of spontaneous nucleation by opposing lateral association. This additional barrier to polymer formation may help explain why MT initiation *in vivo* is especially dependent on a specific nucleator like γ -TuRC (35) that provides MT-like longitudinal stabilization necessary to drive the otherwise unfavorable straightening of $\alpha\beta$ -tubulin (Sup. Fig. 6). It also helps rationalize the remarkably low nucleation efficiency of smaller γ -tubulin assemblies like the γ -tubulin small complex (36), because these smaller assemblies can only overcome a small number of the necessary lateral additions required for MT formation. Additionally, this new view of MT assembly predicts that while the γ -phosphate of GTP provides the driving force for assembly via lattice contacts, it is the spring-like conformational strain within $\alpha\beta$ -tubulin that determines the energy stored in the metastable MT lattice that is released upon catastrophe. Assembly-dependent conformational change effectively means that polymer formation and polymer disassembly are subject to different energetic constraints. This uncoupling of assembly and disassembly is likely important for MT dynamics *in vivo*.

Acknowledgements:

We thank Margot Paulick (UCB) for synthesizing allocolchicine and Dan Southworth, Michelle Moritz and Brian Kelch for helpful comments. We thank the beamline SAXS support staff: Greg Hura (ALS 12.3.1), David Gore, Liang Guo, and Mark Vukonich (APS BIO-CAT), and Hiro Tsuruta (SSRL 4-2). This work was supported by the NIH (GM31627) and

HHMI. LMR was a Paul Sigler/Agouron Institute fellow of the Helen Hay Whitney Foundation.

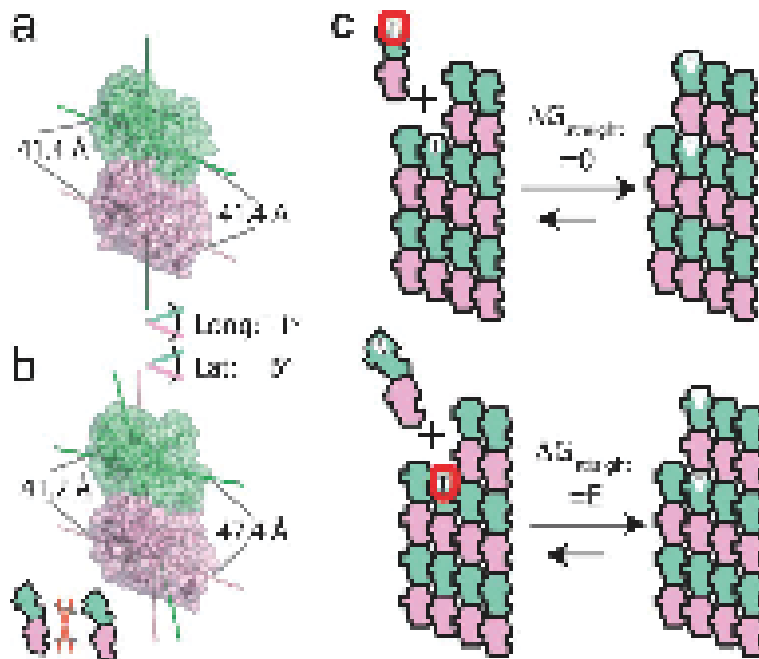


Figure 1. Two conformations of $\alpha\beta$ -tubulin, and conflicting models for the role of GTP. (a) Longitudinal and lateral interaction surfaces are aligned in the straight (1JFF, top), but not in the curved (1SA0, bottom) conformation. In the curved conformation, the a- and b-tubulin protofilament and lateral interaction axes are skewed by 11° and 6° respectively; these rearrangements separate equivalent laterally interacting atoms by up to 6 \AA . Inset: This misalignment of interfaces destabilizes lateral interactions between curved $\alpha\beta$ -tubulins. (b) In the allosteric model, GTP (circled in red) stimulates MT assembly by inducing the straight, MT-compatible conformation in unpolymerized $\alpha\beta$ -tubulin. Incorporation into the lattice is not associated with unfavorable domain rearrangements ($\Delta G_{\text{straight}}=0$). (c) In the lattice model, unpolymerized $\alpha\beta$ -tubulin remains curved even when bound to GTP. Incorporation into the lattice requires unfavorable domain rearrangements ($\Delta G_{\text{straight}}=E$). The lattice-acting GTP (circled in red) provides stronger lattice contacts to stabilize the MT-bound straight conformation.

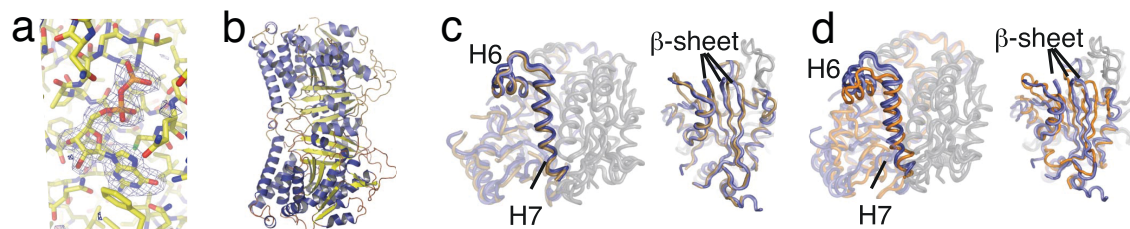


Figure 2. Structural features of γ -tubulin:GDP. (a) F_0-F_c electron density computed from the final model with GDP omitted. The nucleotide binding site of chain A is shown. (b) The two-fold non-crystallographic symmetry interaction between γ -tubulins (Chain A: dark blue and yellow; Chain B: light blue and pale yellow). The nucleotide binding sites ('plus' ends) are top and bottom. (c) γ -tubulin:GDP (chain A: dark blue, chain B: light blue) and γ -tubulin:GTP γ S (tan) adopt the same curved domain organization. See also Sup. Table 2. The left panel highlights helices H6 and H7. The right panel shows the intermediate domain β -sheet (helix H10, which would obscure the view of the β -sheet, has been omitted for clarity). (d) γ -tubulin:GDP (colors as in c) shows characteristic differences when compared to the straight conformation of b-tubulin (PDB code: 1JFF, orange). Left and right panels are as in c.

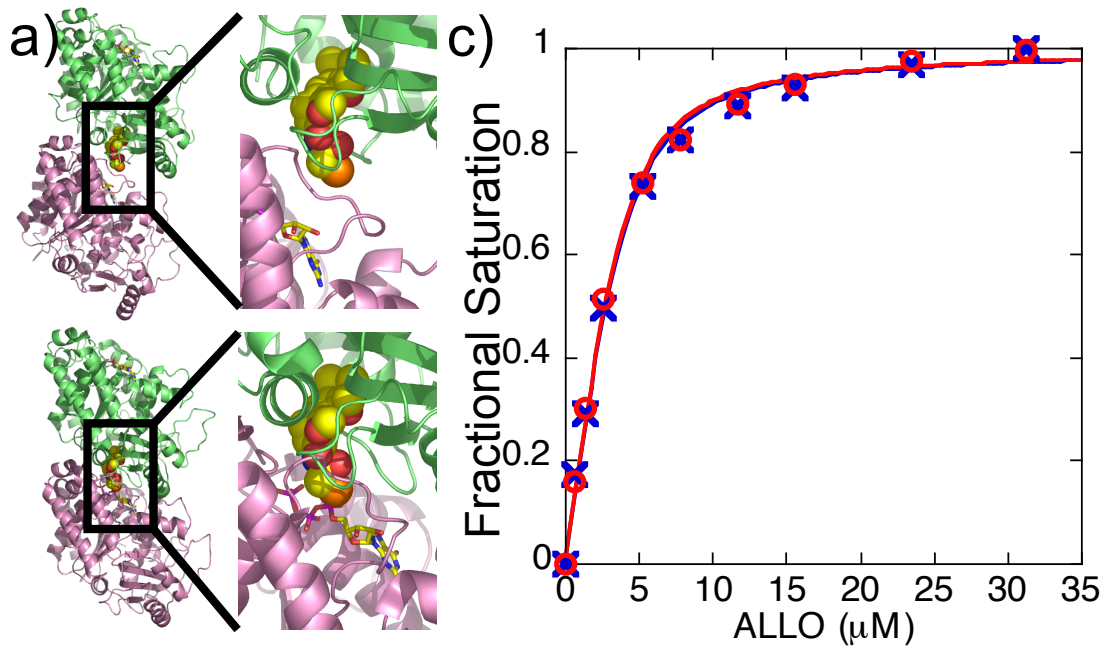


Figure 3. The affinity of $\alpha\beta$ -tubulin for allocolchicine does not depend on nucleotide state.

(a) The colchicine binding pocket as observed in the crystal structure of the curved conformation (1SA0, (3)). Colchicine (spheres) binds between α - (pink) and β -tubulin (green), near the non-exchangeable GTP (sticks). (b) Colchicine binding is not compatible with the straight conformation of $\alpha\beta$ -tubulin. Modeling colchicine into the straight conformation of $\alpha\beta$ -tubulin reveals steric clashes with atoms α - and β -tubulin and the non-exchangeable GTP. (c) Saturation binding curves of allocolchicine binding to $\alpha\beta$ -tubulin in the presence of 1 mM GTP (blue, crosses) or 1 mM GDP (red, squares). Dissociation constants obtained by fitting the curves (solid lines) are 0.79 ± 0.15 mM and 0.74 ± 0.15 mM for $\alpha\beta$ -tubulin:GTP and $\alpha\beta$ -tubulin:GDP respectively.

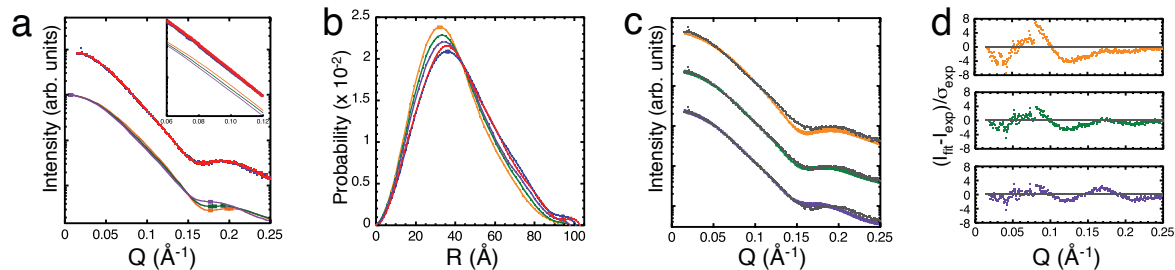


Figure 4. Small angle X-ray scattering shows that $\alpha\beta$ -tubulin:GTP and $\alpha\beta$ -tubulin:GDP adopt essentially identical curved conformations. (a) Predicted scattering curves for straight (PDB 1JFF, brown), curved (PDB 1SA0, green), and more complete curved (γ -tubulin based model, purple) conformations of $\alpha\beta$ -tubulin show differences over most of the scattering range. Measured scattering curves in the presence of 1 mM GTP (blue) or 1 mM GDP (red) are substantially identical. Predicted and measured curves are offset to facilitate comparison. Inset: same comparison (with less offset between measured and calculated curves) over a narrower Q ($=4\pi\sin\theta/\lambda$) range where differences between the calculated curves are most apparent. (b) Pair-distance probability distributions (colors as in a.) obtained from the calculated and measured curves in a. (c) Structural models fit to the $\alpha\beta$ -tubulin:GTP SAXS data (grey dots). Straight conformation (1JFF; brown: $c^2 = 2.34$), curved conformation (1SA0; green: $c^2 = 1.30$), and a more complete model for the curved conformation (purple: $c^2 = 1.11$). Fits are offset to facilitate comparison. (d) Error-normalized residuals $(I_{\text{calc}} - I_{\text{exp}})/s_{\text{exp}}$ from the fits (same color scheme).

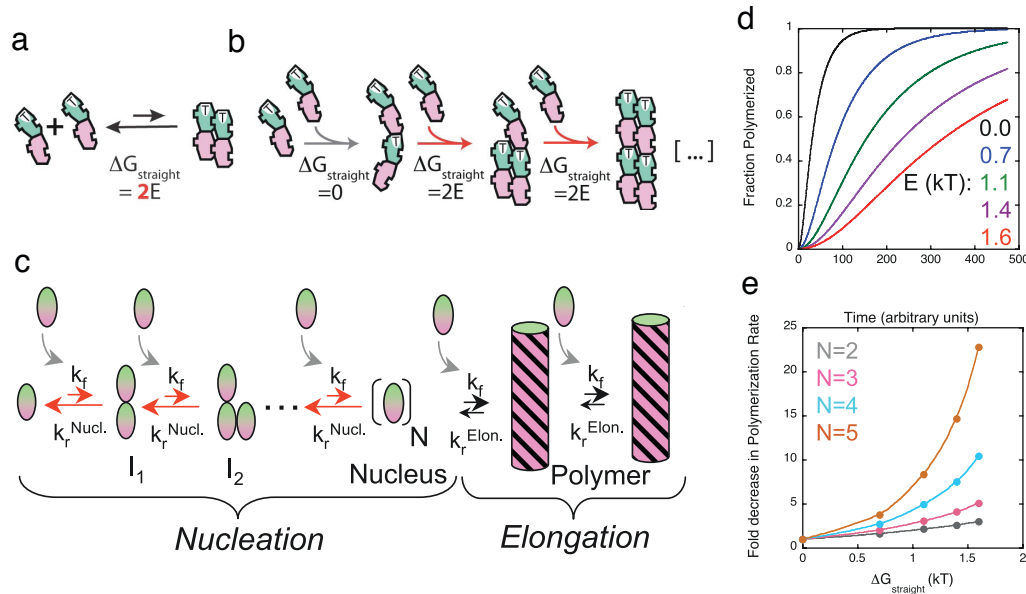


Figure 5. Implications for the kinetics of MT initiation. (a) Assembly-dependent conformational change during MT initiation opposes lateral assembly. In the absence of a straight MT lattice, *both* $\alpha\beta$ -tubulins must change conformation for lateral association. For full straightening, the energetic penalty arising from conformational change during initiation ($\Delta G_{\text{straight}}=2E$) will be double that during elongation. (b) Representation of a possible sequence of early MT initiation intermediates, starting from curved $\alpha\beta$ -tubulin. Pure longitudinal associations (grey arrows) do not require conformational change. To form lateral associations, however, will frequently require that two $\alpha\beta$ -tubulins change conformation (red arrows). These initiation-specific events incur additional energetic costs compared to elongation, and will be selectively disadvantaged (see Fig. 5c). (c) Representation summarizing the kinetic models (see Methods) used to investigate potential consequences of the lattice model. Nucleation is modeled as an arbitrary number of consecutive bimolecular reactions governed by identical association (k_f) and dissociation ($k_r^{\text{Nucl.}}$) rate constants. Red arrows indicate steps that incur the energetic cost of

straightening. Once a critical oligomer is formed (the nucleus, N subunits), elongation by monomer addition becomes energetically favorable and is governed by the same association rate constant (k_f) and a different dissociation rate constant ($k_r^{\text{Elong.}}$). The model treats plus and minus ends of the MT as kinetically indistinguishable (Sup. Fig. 4 presents a possible structural explanation of these known kinetic differences). (d) Energetically unfavorable assembly-dependent conformational changes decrease the stability of nucleation intermediates. The black curve corresponds to self-association of rigid subunits (no conformational change). The energetic cost of assembly-dependent conformational change (DG_{straight}) was estimated at 0.7 (blue), 1.1 (green), 1.4 (purple), and 1.6 (red) kT. This corresponds to 2-, 3-, 4-, or 5-fold reductions in the apparent affinity of subunit associations and significantly decreases the apparent rate of MT assembly. (e) There is a multiplicative slowing effect when multiple nucleation intermediates require energetically unfavorable assembly-dependent conformational change. The cost of assembly-dependent conformational change as described in c. was compared by examining the initial polymerization rate among generic nucleation-elongation models identical except for the size of the nucleus (2: grey, 3: pink, 4: cyan, 5: orange; see Methods).

Methods

Expression, purification, and crystallization of γ -tubulin. Protein expression, purification and crystallization was performed as previously reported (10) with minor changes.

Structure determination. Diffraction data were collected at beamline 8.2.1 (HHMI) at the Advanced Light Source (Berkeley, CA). Data processing and reduction were carried out with HKL2000(37). Molecular replacement searches and refinement were carried out with phaser (38) and model building was performed with O (39). Initial phases were determined by molecular replacement using a γ -tubulin search model (PDB 1Z5V, (10)) with all sidechains truncated to alanine and all cofactors (GTP γ S, Mg²⁺, colchicine, and waters) removed. A conservative approach, along with the improved resolution compared to previous tubulin structures, allowed us to identify a register shift error in H12, the c-terminal helix of the protein (Sup. Fig. 1). Figures made with PyMOL (40).

Allocholchicine binding

Allocholchicine was prepared by Margot Paulick (U.C. Berkeley) following established methods (23). Solutions of 4 mM $\alpha\beta$ -tubulin containing 0, 0.65, 1.3, 2.6, 5.2, 7.8, 11.7, 15.6, 23.4, or 31.2 mM allocholchicine were prepared and equilibrated at 20 °C for two hours before measurement. For each sample, emission spectra were collected between 380 and 420 nm using excitation at 315 nm. The affinity of $\alpha\beta$ -tubulin:GTP and $\alpha\beta$ -tubulin:GDP for allocholchicine was determined by fitting the normalized fluorescence at 400 nm to the

following equation:

$$saturation = \left\{ (Kd + [ALLO] + [\alpha\beta]) - \sqrt{(Kd + [ALLO] + [\alpha\beta])^2 - 4 * [ALLO] * [\alpha\beta]} \right\} / (2 * [\alpha\beta])$$

where Kd represents the dissociation constant for allocolchicine binding, and $(ALLO)$ and $(\alpha\beta)$ denote the total allocolchicine and $\alpha\beta$ -tubulin concentrations respectively. See supplemental Methods for more details.

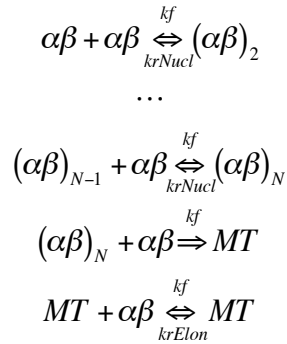
Small-angle X-ray Scattering

Sample preparation, data collection, and the models used for calculations are described in Supplemental Methods. Pair distribution functions were computed using GNOM (41) from data such that $0 < Q < 0.25$, choosing D_{max} so that the curves tail smoothly to zero probability (95 Å for 1JFF, 1SA0, and the γ -tubulin based curved model; 101 and 103 Å for GTP and GDP data, respectively). Radii of gyration determined from these calculated distributions are 29.6 Å, 30.5 Å, and 31.4 Å for straight (1JFF), curved (1SA0), and model curved conformations, respectively, and 33.0 ± 1.1 Å and 32.7 ± 1.5 Å for experimental GTP- and GDP-bound $\alpha\beta$ -tubulin, respectively. The trimmed straight (1JFF), curved (1SA0), and more complete γ -tubulin based curved $\alpha\beta$ -tubulin models were fit to the experimental GTP $\alpha\beta$ -tubulin SAXS data using CRY SOL (42).

Kinetic simulations

Nucleation-elongation kinetic models were constructed to explore the potential consequences of assembly-dependent conformational exchange. We used a generic model that ignores the structural details of oligomer organization because the sequence of intermediates leading to microtubule assembly is not known. Having assumed a

bimolecular on rate constant of $1 \times 10^6 \text{ M}^{-1}\text{s}^{-1}$ and subunit concentrations in the 10 mM range, we chose dissociation rate constants such that subunit addition was relatively high affinity during elongation (k_r^{Elong} such that $K_d^{\text{Elong}} = 1 \text{ mM}$) but significantly lower affinity during nucleation (k_r^{Nucl} such that $K_d^{\text{Nucl}} = 1 \text{ mM}$). These parameters capture the essence of nucleation-elongation behavior, and the conclusions we draw are valid over a broad range of parameters. The species at which subunit addition becomes energetically favorable is



called the nucleus. Kinetic equations corresponding to a model with a nucleus consisting of N subunits are:

where the $(ab)_i$ represent subcritical intermediates, MT represents the microtubule polymer, k_f is the bi-molecular on-rate constant (assumed to be $1 \times 10^6 \text{ M}^{-1}\text{s}^{-1}$), and k_r^{Nucl} and k_r^{Elong} are the reverse rate constants for nucleation and elongation, respectively, calculated so as to give the dissociation constants assumed above. As in other polymerization models, to avoid wholesale destruction of polymers the reverse rate constant for initial polymer formation was set to 0. Assembly kinetics were simulated in Berkeley Madonna (www.berkeleymadonna.com) assuming a monomer concentration of 10 mM, and the assembly-dependent conformational change was modelled as a decrease in the affinity of nucleation steps (increase in k_r^{nuc} by a factor of $\exp(DG_{\text{straight}}/kT)$, where DG_{straight} denotes the estimated energetic cost for conformational change. Fractional assembly was calculated

from $\frac{([\alpha\beta]_i - [\alpha\beta]_t)}{([\alpha\beta]_i - K_D^{Elong.})}$, where $(ab)_i$ and $(ab)_t$ respectively denote the initial and time-dependent concentrations of unassembled $\alpha\beta$ -tubulin, and $K_D^{Elong.}$ denotes the dissociation constant for elongation. To compare models with different number of intermediates, the timescale of the unpenalized run from each model was rescaled such that 10% assembly occurred at $t=10$. Initial rates of assembly were calculated from $1/T_{10\%}$, where $T_{10\%}$ denotes the time taken to reach 10% assembly.

References

1. Desai, A. and T.J. Mitchison, *Microtubule polymerization dynamics*. Annual Review of Cell and Developmental Biology, 1997. **13**: p. 83-117.
2. Lowe, J., et al., *Refined structure of alpha beta-tubulin at 3.5 A resolution*. J Mol Biol, 2001. **313**(5): p. 1045-57.
3. Ravelli, R.B., et al., *Insight into tubulin regulation from a complex with colchicine and a stathmin-like domain*. Nature, 2004. **428**(6979): p. 198-202.
4. Nogales, E. and H.W. Wang, *Structural mechanisms underlying nucleotide-dependent self-assembly of tubulin and its relatives*. Current Opinion in Structural Biology, 2006. **16**(2): p. 221-229.
5. Wang, H.W. and E. Nogales, *Nucleotide-dependent bending flexibility of tubulin regulates microtubule assembly*. Nature, 2005. **435**(7044): p. 911-5.
6. Buey, R.M., J.F. Diaz, and J.M. Andreu, *The nucleotide switch of tubulin and microtubule assembly: A polymerization-driven structural change*. Biochemistry, 2006. **45**(19): p. 5933-5938.

7. Mandelkow, E.M., E. Mandelkow, and R.A. Milligan, *Microtubule dynamics and microtubule caps: a time-resolved cryo-electron microscopy study*. J Cell Biol, 1991. **114**(5): p. 977-91.
8. Muller-Reichert, T., et al., *Structural changes at microtubule ends accompanying GTP hydrolysis: information from a slowly hydrolyzable analogue of GTP, guanylyl (alpha,beta)methylenediphosphonate*. Proc Natl Acad Sci U S A, 1998. **95**(7): p. 3661-6.
9. Chretien, D., S.D. Fuller, and E. Karsenti, *Structure of growing microtubule ends: two-dimensional sheets close into tubes at variable rates*. J Cell Biol, 1995. **129**(5): p. 1311-28.
10. Aldaz, H., et al., *Insights into microtubule nucleation from the crystal structure of human gamma-tubulin*. Nature, 2005. **435**(7041): p. 523-7.
11. Gigant, B., et al., *Structural basis for the regulation of tubulin by vinblastine*. Nature, 2005. **435**(7041): p. 519-22.
12. Schlieper, D., et al., *Structure of bacterial tubulin BtubA/B: evidence for horizontal gene transfer*. Proc Natl Acad Sci U S A, 2005. **102**(26): p. 9170-5.
13. Oliva, M.A., D. Trambaiolo, and J. Lowe, *Structural Insights into the Conformational Variability of FtsZ*. J Mol Biol, 2007. **373**(5): p. 1229-42.
14. Lowe, J. and L.A. Amos, *Crystal structure of the bacterial cell-division protein FtsZ*. Nature, 1998. **391**(6663): p. 203-6.
15. Oliva, M.A., S.C. Cordell, and J. Lowe, *Structural insights into FtsZ protofilament formation*. Nat Struct Mol Biol, 2004. **11**(12): p. 1243-50.

16. Nogales, E. and H.W. Wang, *Structural mechanisms underlying nucleotide-dependent self-assembly of tubulin and its relatives*. *Curr Opin Struct Biol*, 2006. **16**(2): p. 221-9.
17. Shearwin, K.E. and S.N. Timasheff, *Effect of colchicine analogues on the dissociation of alpha beta tubulin into subunits: the locus of colchicine binding*. *Biochemistry*, 1994. **33**(4): p. 894-901.
18. Manuel Andreu, J., et al., *A synchrotron X-ray scattering characterization of purified tubulin and of its expansion induced by mild detergent binding*. *Biochemistry*, 1989. **28**(9): p. 4036-40.
19. Sontag, C.A., J.T. Staley, and H.P. Erickson, *In vitro assembly and GTP hydrolysis by bacterial tubulins BtubA and BtubB*. *J Cell Biol*, 2005. **169**(2): p. 233-8.
20. Oliva, M.A., et al., *Assembly of archaeal cell division protein FtsZ and a GTPase-inactive mutant into double-stranded filaments*. *J Biol Chem*, 2003. **278**(35): p. 33562-70.
21. Kull, F.J. and R.J. Fletterick, *Is the tubulin/FtsZ fold related to the G-protein fold?* *Trends Cell Biol*, 1998. **8**(8): p. 306-7.
22. Nogales, E., et al., *Tubulin and FtsZ form a distinct family of GTPases*. *Nat Struct Biol*, 1998. **5**(6): p. 451-8.
23. Hastie, S.B., *Spectroscopic and kinetic features of allocolchicine binding to tubulin*. *Biochemistry*, 1989. **28**(19): p. 7753-60.
24. Medrano, F.J., et al., *Roles of colchicine rings B and C in the binding process to tubulin*. *Biochemistry*, 1989. **28**(13): p. 5589-99.
25. Shearwin, K.E., B. Perezramirez, and S.N. Timasheff, *Linkages between the Dissociation of Alpha-Beta Tubulin into Subunits and Ligand-Binding - the Ground-State of Tubulin Is the Gdp Conformation*. *Biochemistry*, 1994. **33**(4): p. 885-893.

26. Perez-Ramirez, B., K.E. Shearwin, and S.N. Timasheff, *The colchicine-induced GTPase activity of tubulin: state of the product. Activation by microtubule-promoting cosolvents*. *Biochemistry*, 1994. **33**(20): p. 6253-61.
27. Amayed, P., M.F. Carlier, and D. Pantaloni, *Stathmin slows down guanosine diphosphate dissociation from tubulin in a phosphorylation-controlled fashion*. *Biochemistry*, 2000. **39**(40): p. 12295-302.
28. Melki, R., M.F. Carlier, and D. Pantaloni, *Oscillations in microtubule polymerization: the rate of GTP regeneration on tubulin controls the period*. *EMBO J*, 1988. **7**(9): p. 2653-9.
29. Davies, J.M., et al., *Conformational changes of p97 during nucleotide hydrolysis determined by small-angle X-Ray scattering*. *Structure*, 2005. **13**(2): p. 183-95.
30. Koch, M.H., P. Vachette, and D.I. Svergun, *Small-angle scattering: a view on the properties, structures and structural changes of biological macromolecules in solution*. *Q Rev Biophys*, 2003. **36**(2): p. 147-227.
31. Nagar, B., et al., *Organization of the SH3-SH2 unit in active and inactive forms of the c-Abl tyrosine kinase*. *Mol Cell*, 2006. **21**(6): p. 787-98.
32. Walker, R.A., et al., *Dynamic instability of individual microtubules analyzed by video light microscopy: rate constants and transition frequencies*. *J Cell Biol*, 1988. **107**(4): p. 1437-48.
33. Ferrone, F., *Analysis of protein aggregation kinetics*. *Methods Enzymol*, 1999. **309**: p. 256-74.
34. Elie-Caille, C., et al., *Straight GDP-Tubulin Protofilaments Form in the Presence of Taxol*. *Curr Biol*, 2007. **17**(20): p. 1765-1770.

35. Moritz, M., et al., *Structure of the gamma-tubulin ring complex: a template for microtubule nucleation*. Nat Cell Biol, 2000. **2**(6): p. 365-70.
36. Oegema, K., et al., *Characterization of two related Drosophila gamma-tubulin complexes that differ in their ability to nucleate microtubules*. J Cell Biol, 1999. **144**(4): p. 721-33.
37. Minor, W., M. Cymborowski, and Z. Otwinowski, *Automatic system for crystallographic data collection and analysis*. Acta Physica Polonica A, 2002. **101**(5): p. 613-619.
38. Storoni, L.C., A.J. McCoy, and R.J. Read, *Likelihood-enhanced fast rotation functions*. Acta Crystallogr D Biol Crystallogr, 2004. **60**(Pt 3): p. 432-8.
39. Jones, T.A., et al., *Improved methods for building protein models in electron density maps and the location of errors in these models*. Acta Crystallogr A, 1991. **47 (Pt 2)**: p. 110-9.
40. DeLano, W.L., *The PyMol Molecular Graphics System* <http://www.pymol.org>. 2002, Delano Scientific, San Carlos, CA, USA.
41. Svergun, D.I., *Determination of the Regularization Parameter in Indirect-Transform Methods Using Perceptual Criteria*. Journal of Applied Crystallography, 1992. **25**: p. 495-503.
42. Svergun, D., C. Barberato, and M.H.J. Koch, *CRY SOL - A program to evaluate x-ray solution scattering of biological macromolecules from atomic coordinates*. Journal of Applied Crystallography, 1995. **28**: p. 768-773.

Supporting Information

Rice *et al.* 10.1073/pnas.0801155105

SI Text

Expression and Purification of γ -Tubulin. Protein was produced in Sf9 cells using a baculovirus construct encoding human γ -tubulin with a C-terminal myc-His6 tag. Infections were carried out by the Tissue Culture Core Facility at the University of Colorado Cancer Center. All protein purification work was performed at 4°C. A cell pellet derived from 2.0 liters of cells was resuspended in 6 volumes of lysis buffer (50 mM KPO₄ pH 8.0, 500 mM KCl, 1 μ M MgCl₂, 1 μ M GDP, 10 mM 1-thioglycerol, Complete EDTA-free Protease Inhibitor Mixture Tablet (1 tablet/50 ml) (Roche)), lysed using a microfluidizer, and centrifuged for 15 min at 18,000 X *g* in an JA 25.5 rotor. Imidazole was added directly to the supernatant to a final concentration of 10 mM. The adjusted lysate was clarified by centrifugation for 60 min at 35,000 RPM in a Type 45 rotor and subsequently mixed with 12 ml Ni-NTA Superflow resin (Qiagen) for 1 h. Beads were harvested and washed with 10 volumes of wash buffer A (50 mM KPO₄ pH 8.0, 500 mM KCl, 1 mM MgCl₂, 10% glycerol, 25 mM imidazole, 1 μ M GDP, 10 mM 1-thioglycerol), and 10 volumes of wash buffer B (50 mM K-Mes pH 6.6, 500 mM KCl, 5 mM MgCl₂, 10% glycerol, 25 mM imidazole, 1 μ M GDP, 10 mM 1-thioglycerol). Protein was eluted in wash buffer B + 250 mM imidazole. Fractions containing γ -tubulin were pooled and further purified by gel filtration using a HiLoad 16/60 Superdex 200 column (Amersham Biosciences) pre-equilibrated with gel filtration buffer (50 mM K-Mes pH 6.6, 500 mM KCl, 5 mM MgCl₂, 1 mM K-EGTA, 10 μ M GDP, 1 mM DTT). Peak fractions were identified by A₂₈₀. Protein concentration was determined by

Bradford assay. Pooled fractions were concentrated using Ultrafree Biomax microconcentrators (Millipore). For crystallization, GDP (final concentration: 1 mM) was added to the pooled gel filtration fractions, and the protein was concentrated to 5–7 mg/ml. γ -Tubulin was crystallized by mixing protein (1:1 or 1:2) with top solution (83.3 mM Hepes pH 7.2, 1200 mM KCl, 20% PEG6000, 1 mM GDP; the initial Mg^{2+} concentration during crystallization was therefore either 2.5 or 1.6 mM) and equilibrating against 500 μ l of well solution (83.3 mM Hepes pH 7.2, 600 mM KCl, 20% PEG6000, 1 mM GDP). After 4 days at room temperature, blocky plates were harvested into cryoprotectant (83.3 mM Hepes pH 7.2, 600 mM KCl, 23% PEG6000, 1 mM GDP, 1 mM $MgCl_2$, and 17% glycerol) and frozen in liquid N_2 .

Allocholchicine Binding. Solutions of allocholchicine were prepared by dissolving allocholchicine crystals in DMSO; concentration was determined by UV absorbance using an extinction coefficient of $10250\text{ M}^{-1}\text{cm}^{-1}$ at 276 nm (1). $\alpha\beta$ -tubulin was exchanged into nucleotide free binding buffer (50 mM Hepes 7.1, 50 mM KCl, 1 mM EGTA, 1 mM $MgCl_2$) using NICK (Amersham) desalting columns. The concentration of pooled eluates was determined by UV absorption, using an extinction coefficient of $115,000\text{ M}^{-1}\text{cm}^{-1}$. Pooled $\alpha\beta$ -tubulin was divided into two equal fractions, and GTP or GDP was added to a final concentration of 1 mM.

Small-Angle X-Ray Scattering. For sample preparation, $\alpha\beta$ -tubulin was polymerized in glycerol and pelleted through a 60% glycerol cushion. Pelleted microtubules were rinsed two times with warm SAXS buffer (50 mM Hepes pH 7.5, 1 mM EGTA, 1 mM $MgCl_2$) to

remove excess nucleotides, re-suspended in a small volume of SAXS buffer and depolymerized on ice for 30 min before a final spin to remove microtubule fragments. The resulting protein was applied to NICK desalting columns to remove remaining nucleotide. The concentration of pooled eluates was determined by UV absorption, using an extinction coefficient of $115,000\text{M}^{-1}\text{cm}^{-1}$. Pooled $\alpha\beta$ -tubulin was divided into two equal fractions, and GTP or GDP was added to a final concentration of 1 mM. These samples were then frozen in small aliquots on liquid nitrogen and stored at -80.

SAXS. SAXS data were collected over a range of $\alpha\beta$ -tubulin concentrations (3–10 mg/ml) at $\sim 4^\circ\text{C}$ using an aluminium cuvette mounted in the liquid cooled sample holder at ALS beamline 12.3.1. Short (7-s) and long (100-s) exposures were taken for each sample or buffer scan. Normalization for incident beam intensity and radial integration were performed using programs written by Greg Hura. To minimize differences at high scattering angles that resulted from small normalization errors, raw buffer or protein scans (at identical concentrations) were scaled together (using the tail of the scattering curves in the range $0.25 < Q < 0.3$; Q is defined as $4\pi\sin\theta/\lambda$, where λ is the wavelength and 2θ is the scattering angle) before buffer subtraction. Low and high concentration curves were spliced together to assemble a composite, low noise scattering curve. For comparison to calculated scattering curves, we made small adjustments in the relative scale between raw protein and buffer scans. Scattering profiles for tubulin conformations (straight: 1JFF.pdb; curved: 1SA0.pdb and the γ -tubulin based curved model; see below) of $\alpha\beta$ -tubulin were calculated using the program CRY SOL(2) with default values. To avoid artificial differences that could result from the differing degrees of incompleteness in the two published $\alpha\beta$ -

tubulin models, we based our calculation only on the set of atoms common to both structures (these trimmed structures comprise ~94% of the total expected mass of $\alpha\beta$ -tubulin). In an attempt to compensate for the effect of these missing atoms, we constructed a more complete model for the curved conformation of $\alpha\beta$ -tubulin by replacing the (incomplete) α - and β -tubulin chains with the γ -tubulin:GDP structure.

Supporting References

1. Medrano FJ, *et al.* (1989) Roles of colchicine rings B and C in the binding process to tubulin. *Biochemistry* 28:5589 –99.
2. Svergun D, Barberato C, Koch MJH (1995) CRY SOL - A program to evaluate x-ray solution scattering of biological macromolecules from atomic coordinates. *J Appl Crystallogr* 28:768 –773.
3. Wang HW, Nogales E (2005) Nucleotide-dependent bending flexibility of tubulin regulates microtubule assembly. *Nature* 435:911–915.

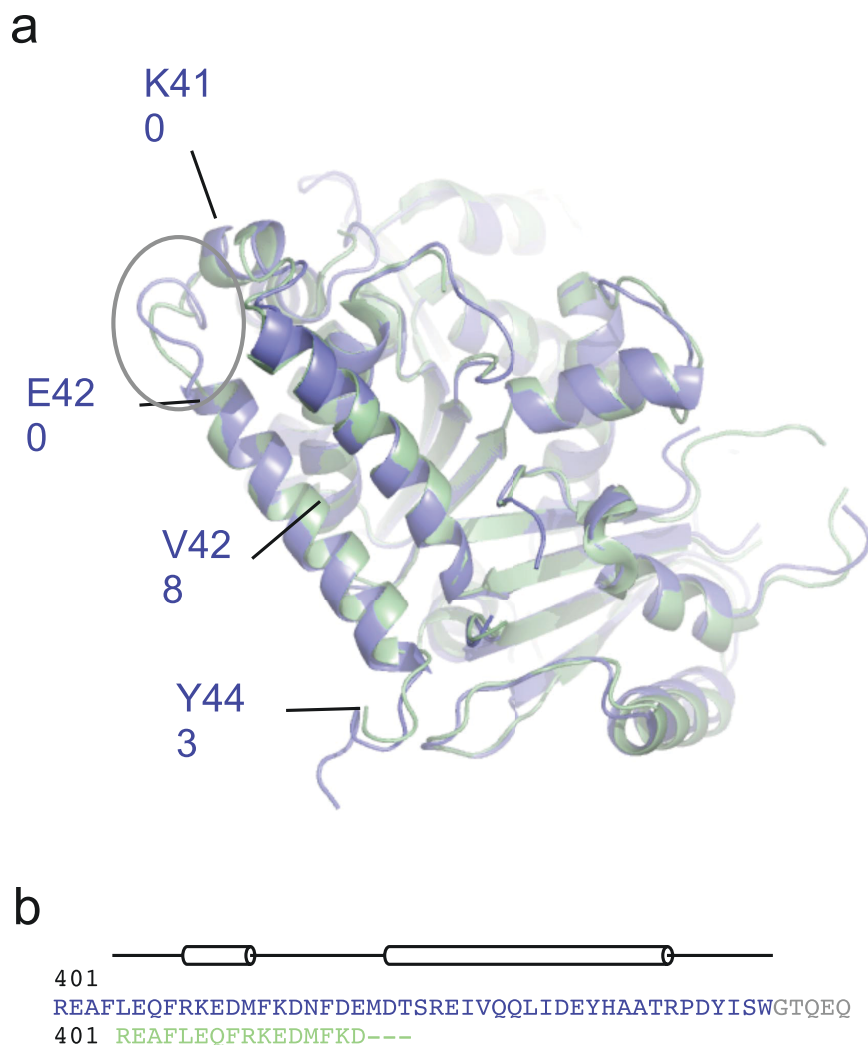


Fig. S1. Corrected chain trace for the C-terminal α -helix. (a) Structural superposition of the previous γ -tubulin structure (1Z5V; pale green) and the current one (Chain A; lavender), highlighting the new sequence register of helix 12 resulting from the new tracing of the preceding loop (circled in gray). The alternate trace begins after residue K410, the identity of a few residues is indicated. (b) Cartoon of the C-terminal secondary structure beginning at residue R401 with the new (lavender) and old (pale green) sequences below. In the new tracing, the loop after residue 411 is extended by three residues.

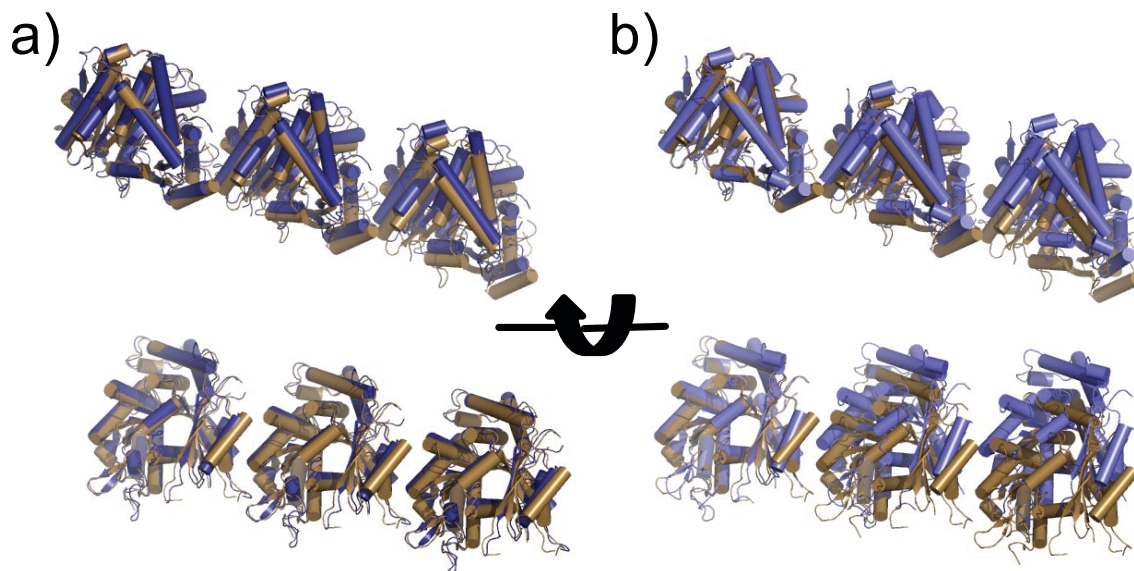


Fig. S2. Lateral interactions in the γ -tubulin:GDP crystal reveal striking adaptability. (a) Lateral interactions between A chains in the crystal resemble those previously observed for γ -tubulin:GTP. Two perpendicular views (top: “outside”, bottom: “minus-end”) indicate γ -tubulin:GDP (chain A, purple) only shows a small reduction in pitch (2 \AA toward the plus end) compared with γ -tubulin:GTP (PDB code: 1Z5V). (b) Lateral interactions between B chains in the crystal resemble those previously observed for γ -tubulin:GTP but show more significant differences. Two perpendicular views (top: outside; bottom: minus-end) indicate that γ -tubulin:GDP (chain B, lavender) shows a greater reduction in pitch (7 \AA toward the plus end and 7° rotation; top) and a change of direction (bottom) compared with γ -tubulin:GTP (PDB code: 1Z5V).

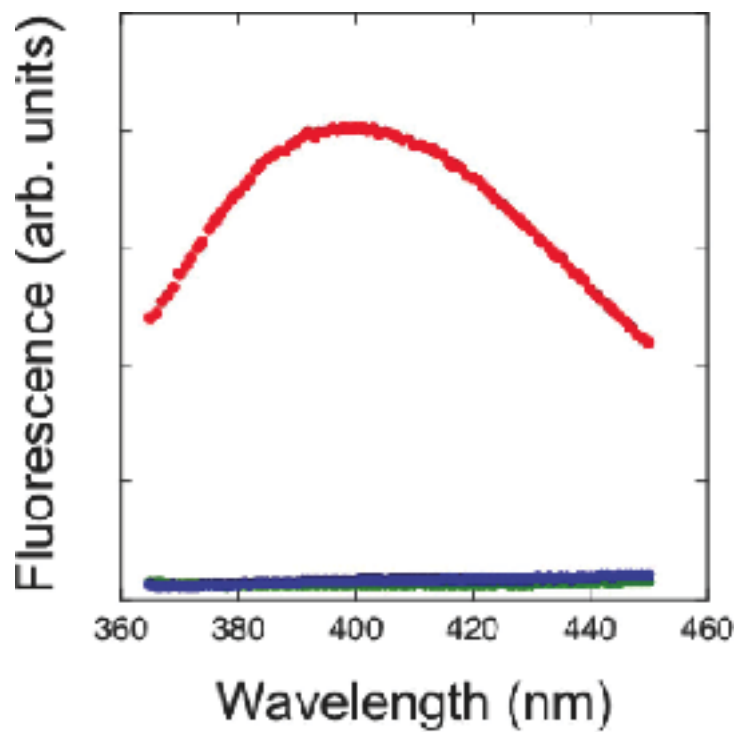


Fig. S3. Allocolchicine fluoresces when bound to $\alpha\beta$ -tubulin. Fluorescence emission spectra for 30 mM allocolchicine (blue circles), 2 μ M $\alpha\beta$ -tubulin (green circles), and 2 μ M $\alpha\beta$ -tubulin equilibrated with 30 mM allocolchicine (red circles).

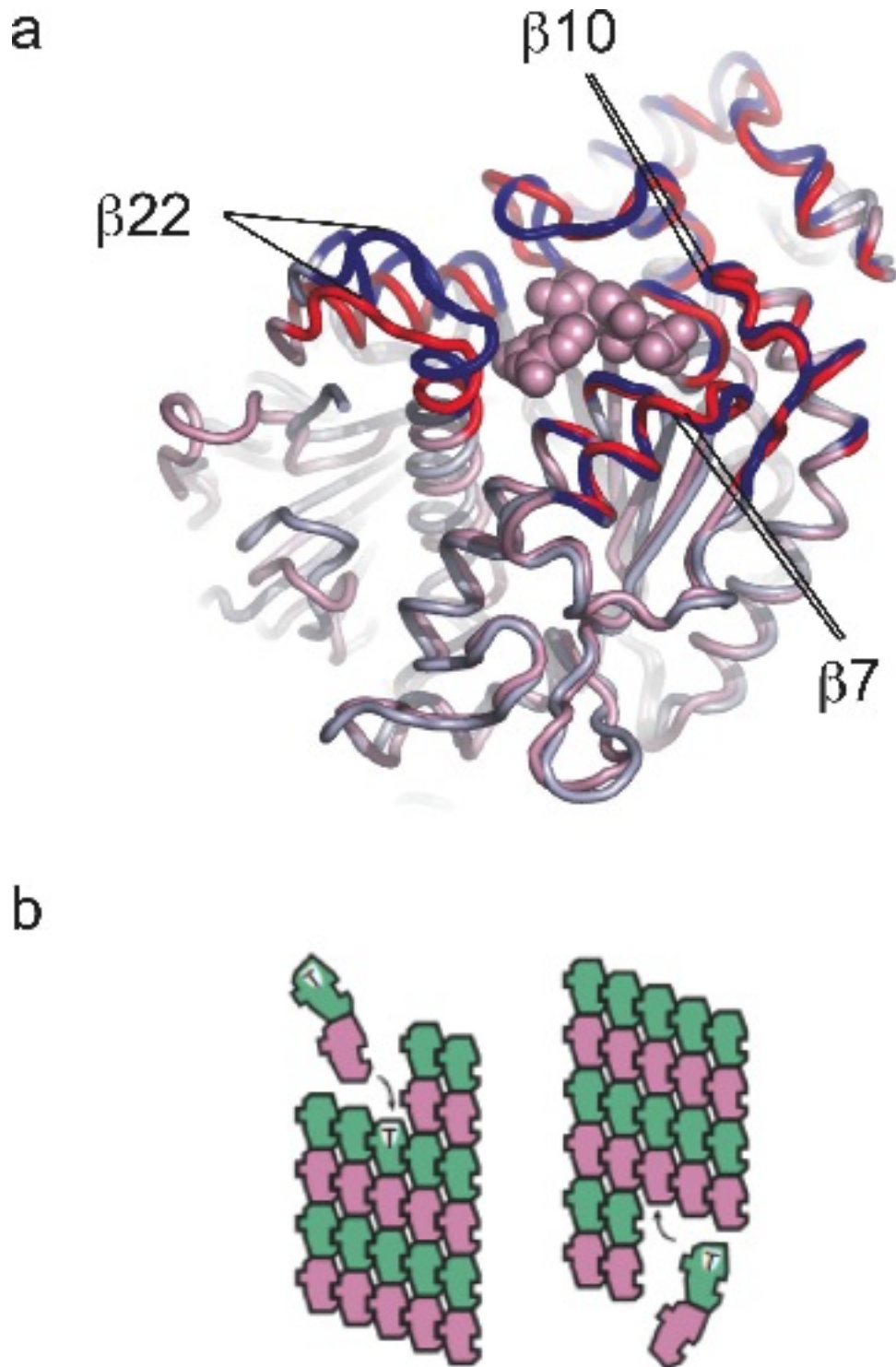


Fig. S4. The straight (blue shades) and curved (red shades) conformations of β -tubulin present the GTP required for assembly in different structural contexts. (a) The straight and curved conformations of β -tubulin were aligned on the N-terminal domain. Residues

that participate in longitudinal polymerization contacts are colored in dark shades. Large differences ($>5.5\text{-\AA}$ shift for Y221) between the two conformations occur in the helical elements shown at left. (b) The changed environment of the nucleotide in straight and curved conformations, coupled with the intrinsic polarity of the microtubule, alters the structural determinants for subunit addition at the plus (*Left*) or minus (*Right*) ends of the microtubule. These structural differences may help explain the different dynamic behavior of microtubule plus and minus ends. At the plus end, the nucleotide (circled in red) that interacts with the incoming $\alpha\beta$ -tubulin is presented in the straight context. At the minus end, the nucleotide (circled in red) that will interact with the lattice is presented in the curved context on the unpolymerized heterodimer.

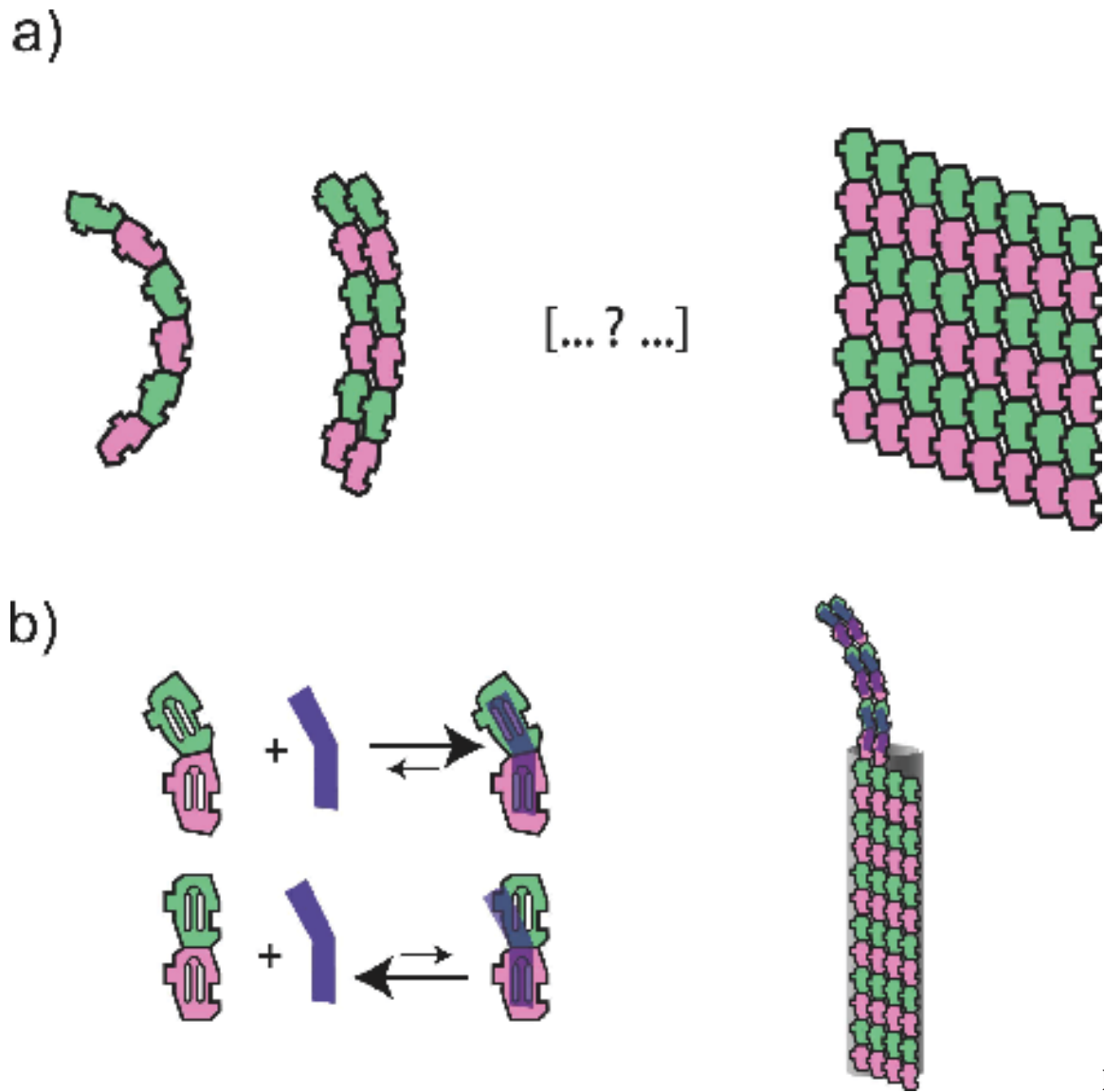
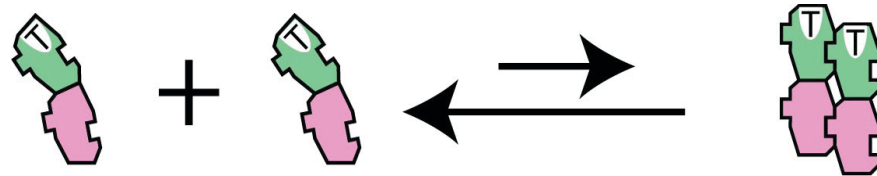


Fig.

S5. $\alpha\beta$ -Tubulin straightening probably occurs incrementally with successive lateral extensions. A spectrum of $\alpha\beta$ -tubulin conformations that depends on the degree of assembly could allow other proteins to differentiate between unpolymerized and polymerized $\alpha\beta$ -tubulin. (a) Longitudinal associations do not require or induce straightening, allowing for curved single protofilaments (*Left*). Partial straightening allows for limited, asymmetric pairwise lateral interactions (as seen in ref. 3; second panel from left). It is likely that full straightening (*Right*) is only achieved after an undetermined

number of additional intermediates with progressively less curvature. Because such intermediates have yet to be observed we indicate them with (...?..). (b) Assembly-dependent curvature provides a mechanism for $\alpha\beta$ -tubulin binding proteins (cartooned in purple) to distinguish between unpolymerized (curved conformation; *Upper Left*) and polymerized tubulins (straight conformation, *Lower Left*). Curvature in the heterodimer changes the relative orientation of potential recognition elements (like the C-terminal helices of α - and β -tubulin, cartooned as scuba-tanks) on the outer surface of the protofilament. In this example, the $\alpha\beta$ -tubulin binding protein prefers to bind the curved conformation of the heterodimer. It is possible that accessory proteins use conformation-selective recognition to associate specifically with functionally unique regions of the microtubule such as the plus end (*Right*).

a)



b)

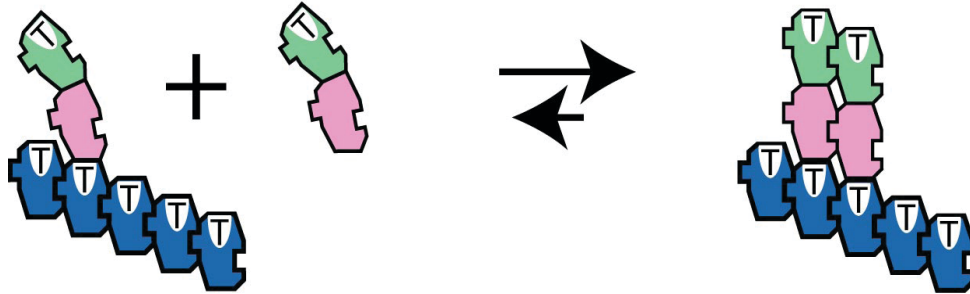


Fig. S6. Nucleators that mimic the microtubule polymer should also overcome the antagonistic effect of the conformational strain that opposes lateral assembly. (a) To permit lateral association in the absence of an existing microtubule lattice, two curved $\alpha\beta$ -tubulins must change conformation; these energetically unfavorable rearrangements incur an energetic cost that opposes the association (indicated by the large backward arrow in the reaction scheme). (b) Nucleators like the γ -TuRC can help overcome the conformational barrier to lateral assembly by providing favorable longitudinal interaction surfaces that stabilize (indicated by a much smaller backward arrow in the reaction scheme) the straight conformation by forming a polymer-like template.

Table S1. Crystallographic data and refinement

Data collection	
Unit cell a, b, c, Å	51.74, 108.76, 83.347
$\alpha, \beta, \gamma, ^\circ$	90, 96.33, 90
Space group	P2 ₁
Temperature, K	100
Minimum Bragg spacing, Å	2.3
Unique observations	40,179
Redundancy	5.7
Completeness, %	98.9 (97.0)
R _{merge}	0.061 (0.112)
1/ σ	20.1 (10.02)
Refinement	
Model (residues)	Chain A: 2–277, 284–310, 313–366, 372–446 Chain B: 3–96, 99–277, 287–307, 313–343, 345–368, 372–446 2 GDP molecules, 378 water molecules
R (R _{free})	0.19 (0.24)
Cross-validated Luzzati coordinate error, Å	0.24
Bond rms deviation, Å	0.008
Angle rms deviation, °	1.15
Average B factor, Å ²	26.7
Residues in most favored ϕ/ψ regions	92.4%
Residues in disallowed ϕ/ψ regions	0.3% (2 residues)

Completeness, R_{merge}, and 1/ σ values in parentheses are for data in the highest-resolution shell.R_{free} was calculated from a test set consisting of 5% of the data.

Table S2. rmsd statistics for structural superpositions of previous tubulin structures onto the two γ -tubulin:GDP structures.

	H6-H7		Intermediate β -sheet		N-terminal domain	
	A	B	A	B	A	B
γ -Tubulin:GTP- γ S (1Z5V)	1.44	0.56	1.04	0.87	0.39	0.35
Curved β -tubulin (1SA0)	1.09	1.19	0.86	0.95	0.87	0.93
Straight β -tubulin (1JFF)	3.87	2.66	2.79	2.63	1.13	1.24

γ -Tubulin:GTP γ S (PDB code 1Z5V) and curved and straight β -tubulin (PDB codes 1SA0 and 1JFF, respectively) were aligned to the two γ -tubulin:GDP chains using the N-terminal domain (residues 1–175). Pairwise rms coordinate deviations for secondary structural elements indicative of curved and straight conformations (helices H6-H7 comprises residues 208–244 and the intermediate domain β -sheet comprises residues 267–274, 313–321, 351–356, and 373–382) were calculated from these aligned models. Statistics for the N-terminal domain are provided as a control to show that this region aligns well for all sequences and conformations. The γ -tubulin:GDP structures are clearly in a curved conformation (see also Fig. 1 *c* and *d*).

Chapter Three

Initial studies on the expression and purification of recombinant monomeric tubulin family members γ -tubulin, δ -tubulin and ϵ -tubulin

Introduction

Microtubules play an essential role in eukaryotic cell function, with key roles in cellular trafficking and chromosome separation. Much of the spatial and temporal patterning of the dynamic microtubule cytoskeleton is regulated via nucleation by γ -tubulin containing protein complexes. Unlike the $\alpha\beta$ -tubulin heterodimer that makes up the microtubule, γ -tubulin is monomeric, does not form protofilaments under normal *in vivo* conditions, and can template microtubules when organized as a component of the 2.2MDa γ -tubulin ring complex (γ -TuRC). Efforts in our lab (1-3) and other labs (4-6) have shown that within the microtubule organizing center (MTOC), the γ -TuRC is the protein assembly responsible for nucleation of 13 protofilament microtubules formed of α/β -tubulin heterodimers. Within the γ -TuRC, the γ -tubulin small complex (γ -TuSC), a heterotetramer of two γ -tubulins interacting with two accessory proteins (GCP2 and GCP3), forms a ring, likely containing 7 γ -TuSCs, which leaves 13 γ -tubulins accessible to template microtubule growth (reviewed in (7)).

While the general mechanism for cytoplasmic MT formation by γ -TuRC is well appreciated, little is known about the formation of doublet and triplet MTs within another structure of the MTOC of higher eukaryotes, the centriole. Centrioles consist of triplet microtubules (although some organisms have only doublet and singlet microtubules) arranged in a 9-fold cartwheel structure, connected by an internal spoke system with a hub (a review of structural progress in (8)). The microtubule triplets consist of an A-tubule consisting of 13 protofilaments, and B- and C-tubules consisting of 10 protofilaments each (9). One edge of the B-tubule is attached to one of the protofilaments involved in the A tubule seam (a discontinuity in the α - α , β - β interactions) (10).

In addition to nucleation of cytoplasmic microtubules, the γ -TuRC is also necessary for centriole duplication (11), presumably to nucleate the initial singlet MTs upon which doublet, and then triplet MTs grow. By analogy with gTuRC, there probably exists machinery that specifically nucleates the branch structure that leads to each secondary ring. Within the last decade, two new tubulin family members, δ - and ϵ -tubulin, were discovered to be centriolar proteins that affect triplet formation (12, 13). These are thus superb candidates for carrying out B-, and C-tubule nucleation much as γ -tubulin aids in formation of the A-tubule. δ - And ϵ -tubulin genes are found in a number of vertebrates (*H. sapiens*, *M. musculus*, etc.) and some unicellular organisms such as *Chlamydomonas reinhardtii* and *Paramecium tetraurelia*, but are missing from many classic model organisms such as *C. elegans*, *S. cerevisiae*, and *D. melanogaster*, however, δ - and ϵ -tubulin appear to exist in most organisms that have triplet microtubules (14). Although the oligomeric state of these tubulins is unknown, it does not appear that either of them forms obligate heterodimers as with $\alpha\beta$ -tubulin, and thus, like γ -tubulin, are likely to play a role in MT nucleation (Figure 1, table 2).

Following up on the research done with postdoctoral scholar Luke Rice in the previous chapter of this work (Chapter 2), we wished to do further detailed studies investigating the role of nucleotide in the function of γ -tubulin. We wished to pursue this as a means to both understand its specific role in nucleation, and also as a way of continuing our studies into the important role GTP plays in microtubule formation. In order to pursue these studies, we wished to be able to express and purify recombinant γ -tubulin. Our initial goal was to use this recombinant protein system to make mutations in to create a γ -tubulin with altered nucleotide specificity, allowing us to tease apart the role of nucleotide for γ -

tubulin from its role in the growth of microtubules, as both $\alpha\beta$ - and γ -tubulin bind and hydrolyze GTP. Our preliminary design altered the specificity to isoGTP (Figure 3).

Additionally, we wished to investigate other monomeric eukaryotic tubulins to understand their role in microtubule nucleation and formation, and identified two new tubulin family members, δ - and ϵ -tubulin, discussed above, in the literature as possible candidates for study. We wished to accomplish soluble recombinant protein for biochemical and structural studies. An additional goal was to perform pull-downs out of cells with greater than normal number of centrioles to find δ - and ϵ -tubulin binding partners.

Both the γ -tubulin and δ - and ϵ -tubulin proteins could be overexpressed in both *E. coli*. Unfortunately, protein overexpressed in *E. coli* of these monomeric tubulins in all the conditions explored was bound to chaperones, which I was unable to remove. All three were cloned into baculovirus. These studies never progressed past the initial stages, so it is yet unknown whether they would have succeeded in their purpose. I am hopeful that with a bit of tenacity, another scientist in the lab will be able to accomplish a soluble purification of these proteins for further study.

In the results section following, I have not included all the variations that I tried in order to accomplish my goals with this project. I have picked a few examples of experiments done to outline what was and what was not accomplished during the duration of these projects.

Results and Discussion

Expression in E. coli and preliminary purification of γ -tubulin

Because there were ongoing studies of the budding yeast γ -TuSC complex, we chose the yeast homolog of γ -tubulin as the initial candidate to attempt expression in *E. coli* and purification, despite the fact that the lab had a previously established protocol for the purification of human γ -tubulin from baculovirus infected sf9 cells. Yeast protein Tub4p was cloned into both an n-terminally his-tagged construct (into pET15b from Novagen), and a C-terminally his-tagged construct (into pET29b from Novagen). Various cell types and growth conditions were attempted including modified salt growth conditions, temperature, cells with rare tRNAs encoded (Rosetta™ 2, EMD4Biosciences), cells designed for lower growth temperature (ArticExpress™, Agilent), and low and high temperature growth conditions. In general most purification attempts were made with the c-terminally tagged construct (Tub4p-pET29b) in Rosetta™ 2 cells.

The c-terminally and n-terminally tagged constructs were made to test if one would be more soluble than the other, using a NiNTA column, following the current lab protocol for human γ -tubulin from sf9 pellets. Ultimately, it appeared that neither construct was particularly more soluble than the other (see Figure 3). Tub4p-pET15b is 54.7908 kDa, and Tub4p-pET29b is 53.6926 kDa. It is not clear from the initial gels whether any Tub4p was eluted from the NiNTA elution with imidazole, although it is obvious that the majority of the protein is insoluble and remains in the pellet after lysis. A purification of just Tub4p-pET29b with both a NiNTA column followed by a size exclusion column (Superdex 200, GE Healthcare) reveals that under these conditions, little protein remains after NiNTA elution, and the remaining fraction is still quite contaminated with other proteins after the size exclusion run. This is demonstrated with both SDS-PAGE and westerns using anti-his-tag antibodies (Figures 4,5). Additionally, a larger batch preparation was performed using 4L

of cell growth rather than the 1L initially used (Figure 6). Unfortunately this did not improve the yield of soluble protein, and it was equally contaminated as the smaller preparation.

Another basic strategy was to try and NiNTA column followed by anion exchange (MonoQ, GE Healthcare). This contained several peaks that westerns indicated contained Tub4 using anti-his-tag antibodies – possibly there is more than one species, and it is unclear from gels if there are other proteins contained in each of those species. The second peak did not show up well on SDS-PAGE staining (Figure 7). If further studies were done to pursue purification of Tub4 from *E. coli*, anion exchange seems more promising than size exclusion as a separation method.

Given the amount of γ -tubulin that was in the insoluble fraction of lysed cells, I attempted a denaturing preparation, in order to both obtain a maximal amount of soluble protein, as well as the possibility of removing chaperone contamination. This preparation did yield some fairly pure protein, although the majority of protein crashed out during the refolding phase of the experiment (Figure 8). It was not possible to easily to determine the folded state of the γ -tubulin that remained after filtered out the precipitated protein.

Preliminary purification of Tub4p from baculovirus infected Sf9 cells

We were able to obtain some cell pellets of Sf9 cells that had been infected with Tub4p expressing baculovirus, which had been created by Dr. Alex Zelter in the lab of Dr. Trisha Davis at the University of Washington. I used the established protocol for human γ -tubulin in the lab. This preparation seemed to yield a higher fraction of soluble protein, but

it also seemed to be very contaminated after the normal γ -tubulin purification steps (Figure 9).

Expression and preliminary purification of δ - and ϵ -tubulin

We obtained cDNA for human δ - and ϵ -tubulin as a kind gift from Dr. Tim Stearns at Stanford University. They were cloned into two vectors, 24ba2 from the lab of Dr. Robert Stroud, and pBAD arabinose inducible vector. Both constructs contained his-tags. The 24ba2 clones were overexpressed successfully in BL21(DE3) and Rosetta™ 2 cells. These constructs did not appear to be particularly soluble, so an attempt was made to limit the induction level using the more tunable pBAD vector. The pBAD constructs were overexpressed using different levels of arabinose induction, ranging from 20% to 0.002%. In Figure 10, we see that even at the highest amount of arabinose, there is no apparent change in induction from the pre-induced sample by SDS-PAGE. However, with anti-his-tag western, we see expression from 0.2-20% Arabinose. Purifications using these samples were attempted, mainly focused on δ -tubulin, as it seemed slightly more soluble than ϵ -tubulin. Most attempts were to find a way to remove what appeared to be the chaperone GroEL, with no apparent success, including ATP washes and the addition of detergent (Figure 11).

We additionally tried to create baculovirus constructs to infect insect cells. At the time, we were in the initial stages of setting up this kind of expression in lab, so these attempts may not have been done in the most optimal manner. Purification with these constructs offered potential soluble protein, but these efforts were abandoned before many attempts were made (Figure 12).

Although the attempts that were made so far did not yield any soluble final product, I think the most viable approach was using the baculovirus/insect cell expression products. I think with more careful production of the proteins, followed by a more in-depth analysis of the purification will potentially yield soluble protein with which to perform biochemical and structural analysis of these under-studied proteins. Other potential means to investigate these proteins *in vitro* include investigating the solubility of different species.

Methods

Cloning of Tub4p, human δ -tubulin and human ϵ -tubulin

Yeast γ -tubulin, Tub4p, was cloned into several different vectors. First, it was cloned into both pET15b and pET29b (Novagen) with directional cloning using NdeI and XhoI in the MCS. Additionally it was cloned into a pIEx/Bac-3™ (EMD4Biosciences) Plasmid by ligation independent cloning, although experiment shown in figures here are from Baculovirus produced in the Davis Lab at University of Washington by other methods.

Human δ -tubulin and human ϵ -tubulin were cloned in the LIC vector 24ba2, and pBAD/HisA (Invitrogen) using direction with XhoI and HindIII restriction enzymes. These proteins were also cloned into pIEx/Bac-3™ (EMD4Biosciences) plasmids by ligation independent cloning, which is shown here, but addition into the Bac-to-Bac system using pFastBac HTB his-tagged vectors (Invitrogen), using iPCR.

Expression of Tub4p, human δ -tubulin and human ϵ -tubulin

For expression of Tub4p, h δ -tubulin and h ϵ -tubulin in *E. coli*, plasmid constructs were transformed into either BL21(DE3)* or Rosetta™ 2 cells. Cells were grown up

overnight from a colony from solid media in the presence of antibiotic. 1 L of autoclaved media (generally LB, high-salt) was inoculated with ~10 ml of overnight culture. Cells were grown to OD600 of ~0.5. In most cases, cells were induced with 1mM IPTG. Most cells were grown at 37 degrees Celsius for growth and expression. One exception is h δ -tubulin and h ϵ -tubulin in pBAD constructs – for expression tests, 10 mL of LB was inoculated with overnight culture and grown to OD600 of ~0.5 and then 100 ml of arabinose at various concentrations (0.002%, 0.02%, 0.2%, 2%, 20%) was added and cultures were grown for an additional 4 hours. For purification tests, 1L of cells were induced with 1 mL of 20% arabinose.

Two systems of baculovirus/sf9 cell expression were used – InsectDirect™ from EMD4Biosciences, and Bac-to-Bac™ from Invitrogen. The figures here represent tests only from the InsectDirect™ system. In the InsectDirect™ system, clones are transfected into sf9 cells using special Insect GeneJuice®. In the Bac-to-Bac™ system, we transformed cloned vectors (pFastBac™HTB) into DH10Bac™ *E. coli* cells, and we then purified the recombinant bacmid from positive colonies. The purified bacmid was then transfected into sf9 cells. Cells were harvested at various times after infection.

Purification of Tub4p, human δ -tubulin and human ϵ -tubulin

Because of the volume of different test purifications that were done, this portion of the methods cannot be inclusive. Most initial purifications were modeled after the Agard lab's protocol for purification of h-myc-his- γ -tubulin (see previous chapter, and Aldaz and Rice, Nature 2005).

Figure 7 shows a chromatogram of a MonoQ (GE Life Sciences) column run post-NiNTA column. In this example prep, the 3 ml elution of the NiNTA column was diluted to a volume of 50 mL and loaded onto the column and a linear gradient was performed between 0-100% Buffer B. (Buffer A: 50 mM K-MES pH 6.6, 5 mM MgCl₂, 1 mM K-EGTA, 10% glycerol, 10 mM GDP, 10 mM thioglycerol) Buffer B: 1 M K-MES pH 6.6, 5 mM MgCl₂, 1 mM K-EGTA, 10% glycerol, 10 mM GDP, 10 mM thioglycerol)

Figure 8 shows a denaturing preparation. In this preparation, a 1 L cell pellet was lysed (Lysis Buffer: 100 mM K-Phosphate, 10 mM Tris-HCl, 8M Urea, 0.5% Tween-20, 1 mM PMSF, adjusted to pH 8) using the Emulsiflex-C3 (Avestin). Lysate was spun down at 10k x g for 30 minutes. Clarified supernatant was bound to 3 mL bed volume of NiNTA beads (Qiagen) for 1 hr at room temperature. The column was then washed with 2 CV of wash buffer (100 mM K-Phosphate, 10 mM Tris-HCl, 8M Urea. Adjusted to pH 6.3), Then eluted with 2 CV of e1 buffer (100 mM K-Phosphate, 10 mM Tris-HCl, 8M Urea. Adjusted to pH 5.9), followed by an extensive elution using e2 buffer (100 mM K-Phosphate, 10 mM Tris-HCl, 8M Urea. Adjusted to pH 4.5) of 15 ml. Protein was then sequentially dialyzed (D1: 6 M Urea, D2: 4 M Urea, D3: 2 M Urea, D4: 0 M Urea +500 mM KCl, 0.5% Tween-20, 50 mM Arginine, 250 mM AmSO₄, 5 mM DTT, 100 mM K-Phosphate, 10 mM Tris-HCl, 1 μM GDP). Precipitate protein in the dialysis bag was consequently filtered out using a syringe filter.

In Figure 12 A, 1L hδ-tubulin-pBAD/HisA cell pellet was lysed (lysis buffer: 50 mM HEPES pH 8.0, 500 mM KCl, 1 mM MgCl₂, 10% glycerol, 1 μM GDP, 1 mM 1-thioglycerol, 2 EDTA-free protease tabs (SIGMA)) using the Emulsiflex-C3. Lysate was spun down at 30k x g for 40 minutes. Imidazole was added to supernatant to 10 mM. Supernatant was incubated with pre-equilibrated NiNTA resin (3 ml bed volume) for 1 hr at 4 degrees.

Column was then washed with 100 mL wash buffer (50 mM HEPES pH 8.0, 500 mM KCl, 1 mM MgCl₂, 10% glycerol, 1 μM GDP, 1 mM 1-thioglycerol, 25 mM imidazole), and eluted in a volume of 5 mL (elution buffer: 50 mM HEPES pH 8.0, 500 mM KCl, 1 mM MgCl₂, 10% glycerol, 1 μM GDP, 1 mM 1-thioglycerol, 250 mM imidazole). In B of the same figure, the purification steps were the same, but all the buffers were changed to have 5 mM MgCl₂ and 2 mM ATP. In C of the same figure, 0.5% sarkosyl was added to all buffers.

In Figure 13, an example of attempted purification from InsectDirect™ system. Transfected cultures were lysed using 0.5 mL of Insect PopCulture™ solution + Benzonase nuclease, with a 15 minute incubation. Lysate was added to 1 mL bed volume pre-equilibrated NiNTA resin, and incubated for 30 minutes at 4 degrees. Column was washed with 30 mLs wash buffer (50 mM HEPES pH 8.0, 500 mM KCl, 1 mM MgCl₂, 10% glycerol, 1 μM GDP, 1 mM 1-thioglycerol, 25 mM imidazole) and then eluted with 2 mLs elution buffer (50 mM HEPES pH 8.0, 500 mM KCl, 1 mM MgCl₂, 10% glycerol, 1 μM GDP, 1 mM 1-thioglycerol, 250 mM imidazole)

	α	β	γ	δ	ϵ
α	100	58	47	36	45
β		100	52	35	44
γ			100	43	44
δ				100	36
ϵ					100

Table 1. Percent similarity between different members of the human tubulin family.

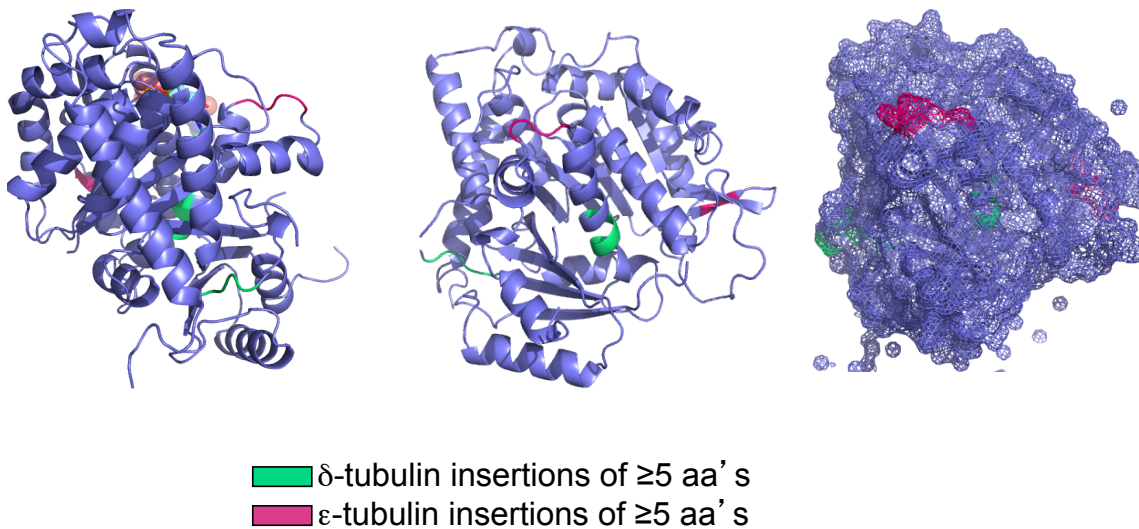


Figure 1. Modeling of the insertions in δ - and ϵ -tubulin onto the structure of γ -tubulin.

Green is for δ -tubulin insertions of larger than 5 amino acids, and pink is for ϵ -tubulin insertions of larger than 5 amino acids.

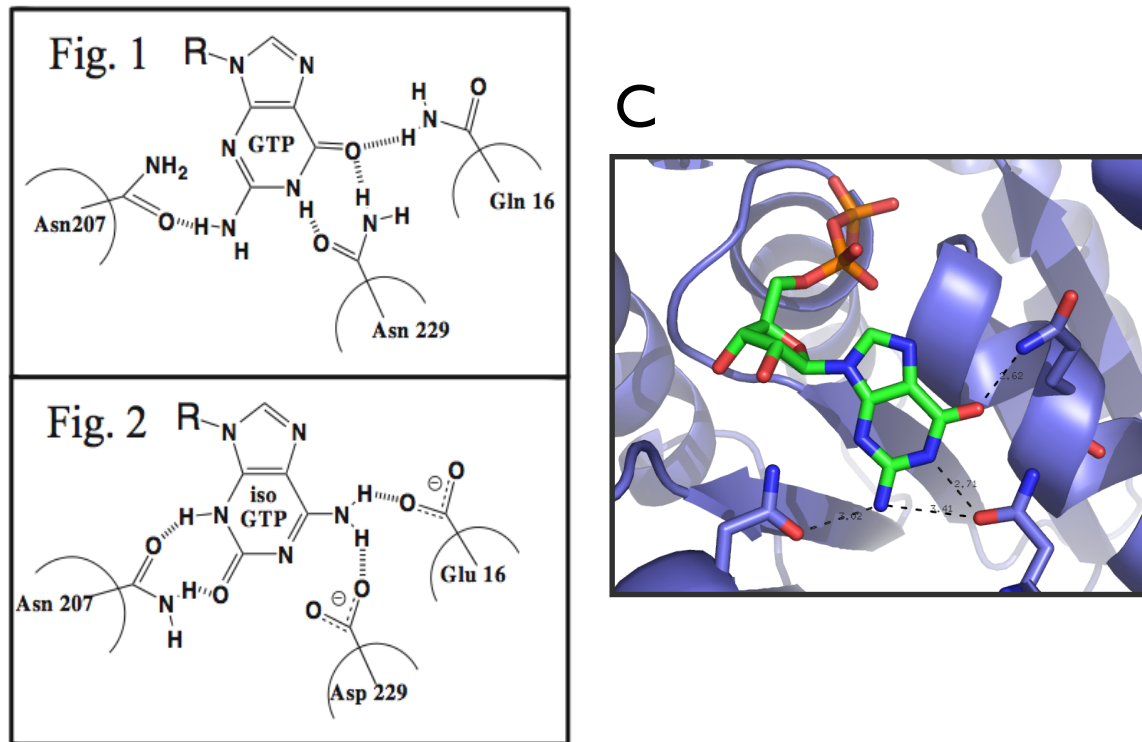


Figure 2. Nucleotide binding in γ -tubulin. A,C, Interactions driving GTP binding to γ -tubulin; specificity is conferred through the side chain H-bonding of three key residues – Asn 207, Gln 16, Asn 229. B, Proposed changes to NTP binding pocket to a preferred binding of the modified isoGTP of N229D and Q16E.

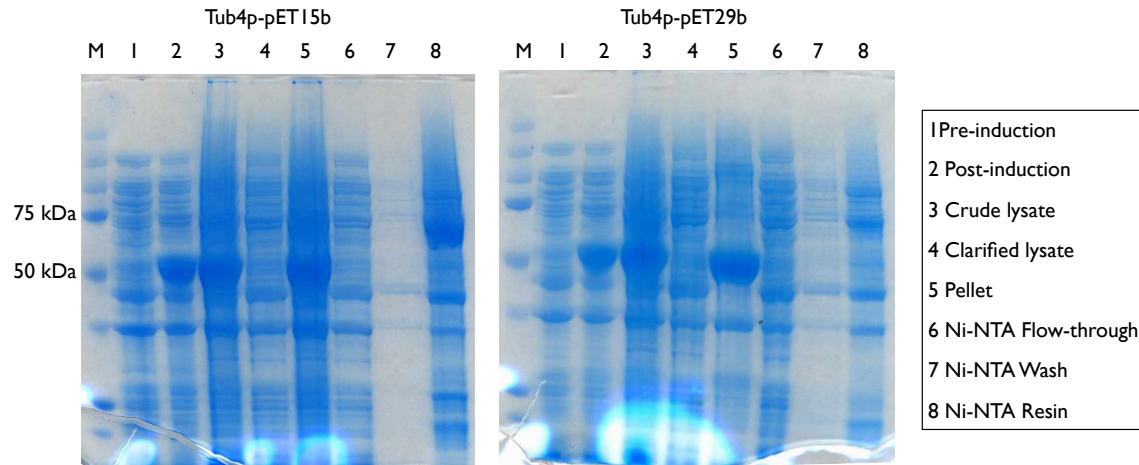


Figure 3. Initial over-expression and purification tests of *S. cerevisiae* γ -tubulin homolog Tub4p in *E. Coli*.

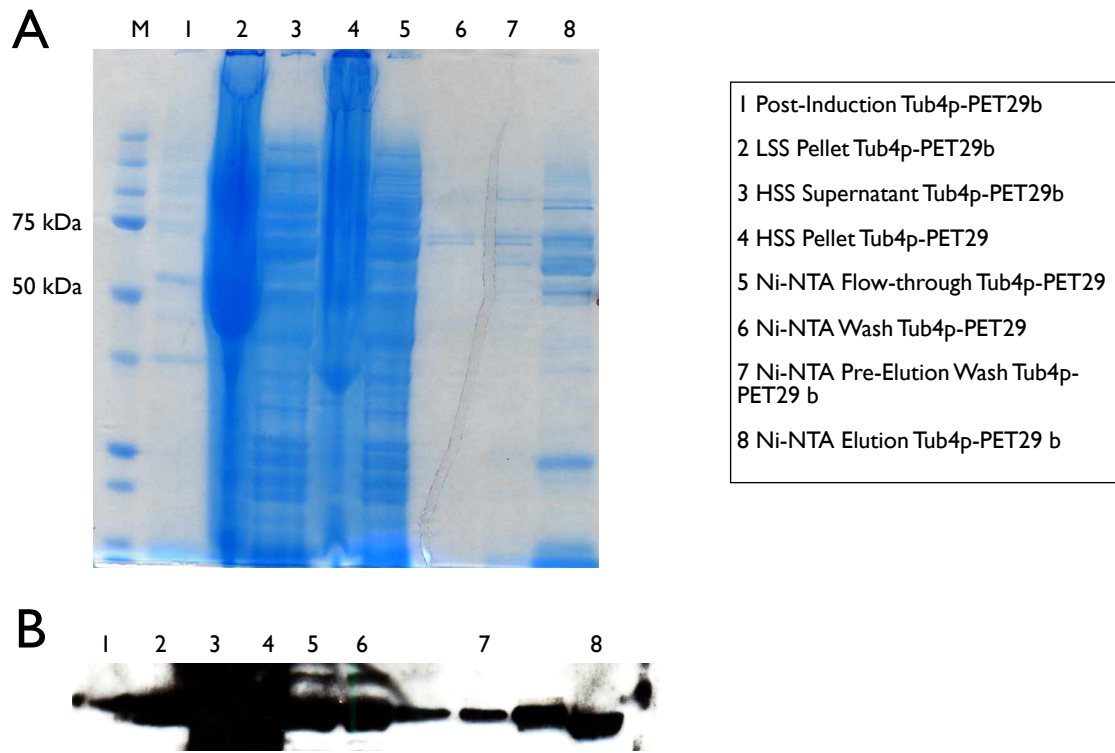


Figure 4. Initial test prep of Tub4p-pET29b (C-terminal his-tag). A. SDS-PAGE gel using Safestain (tm). B. Western blot using anti-his antibody

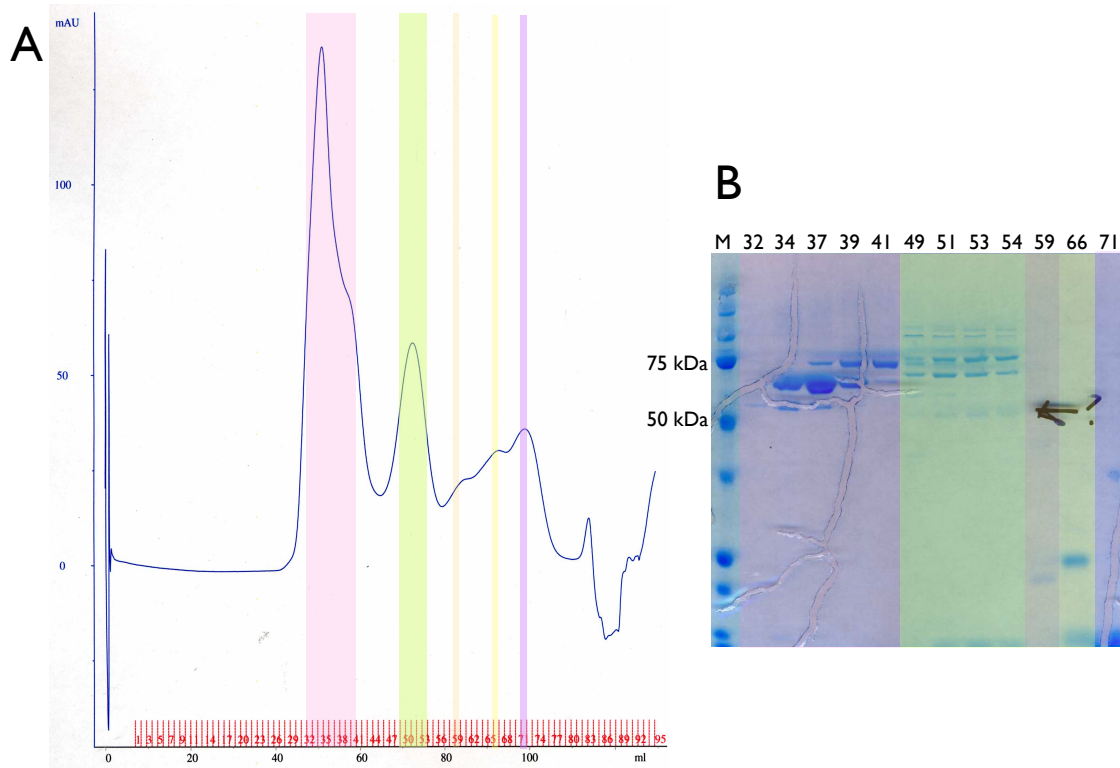


Figure 5. Analysis of Tub4p-pET29b test prep, S200 16/60 sizing column. A. Chromatogram monitoring 280nm B. SDS-PAGE gel using Safestain™ of sizing column fractions.

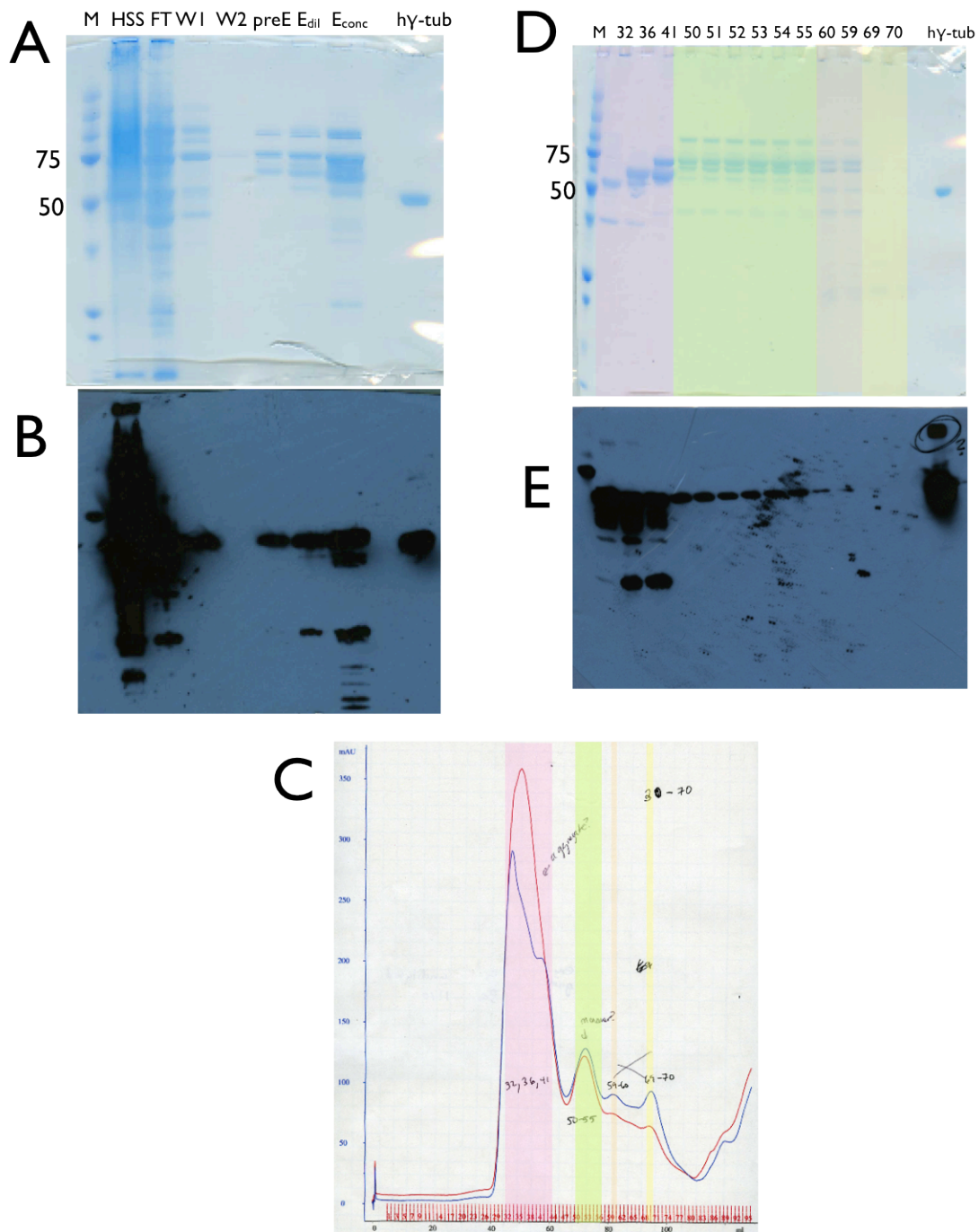


Figure 6. 4L batch purification of Tub4p-pET29b. A and B SDS-PAGE and western of Lysis through NiNTA column elution. C Chromatogram of Sizing Column S200 16/60 monitoring 280nm(Blue) 260nm(Red). D and E SDS-PAGE and western of Westerns are done with anti-his antibody.

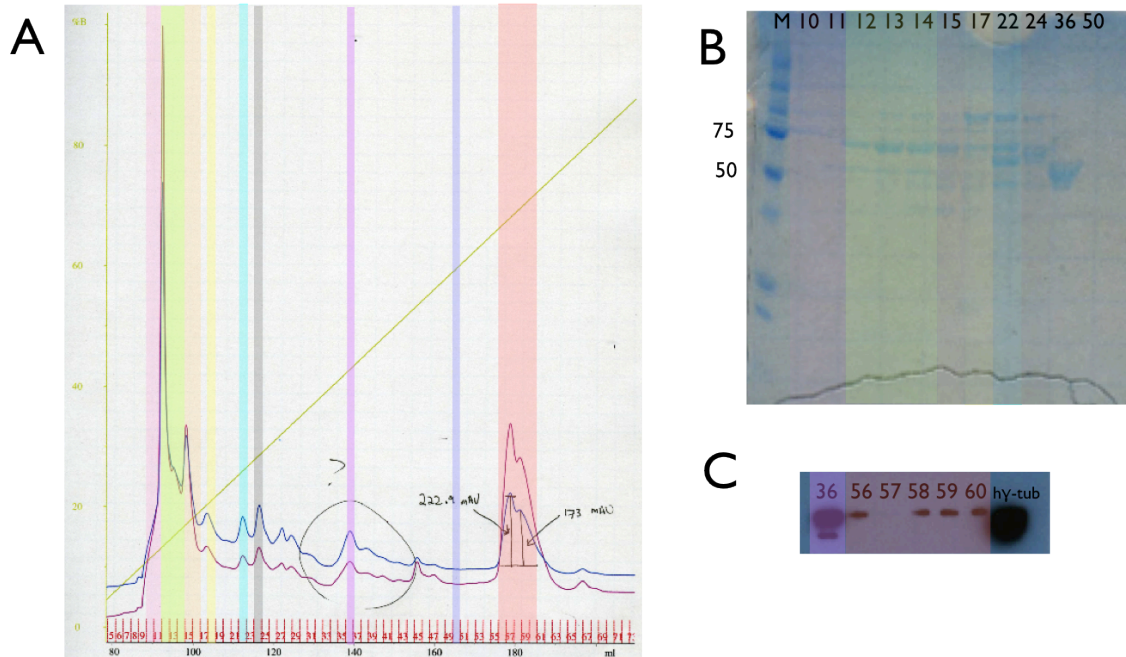


Figure 7. Test prep of Tub4p-pET29b with use of MonoQ anion exchange column. A Chromatogram of MonoQ run, blue 280 nm, purple 260 nm. B SDS-PAGE of relevant fractions of column run C Western of relevant fractions of column run, using anti-his-tag antibody.

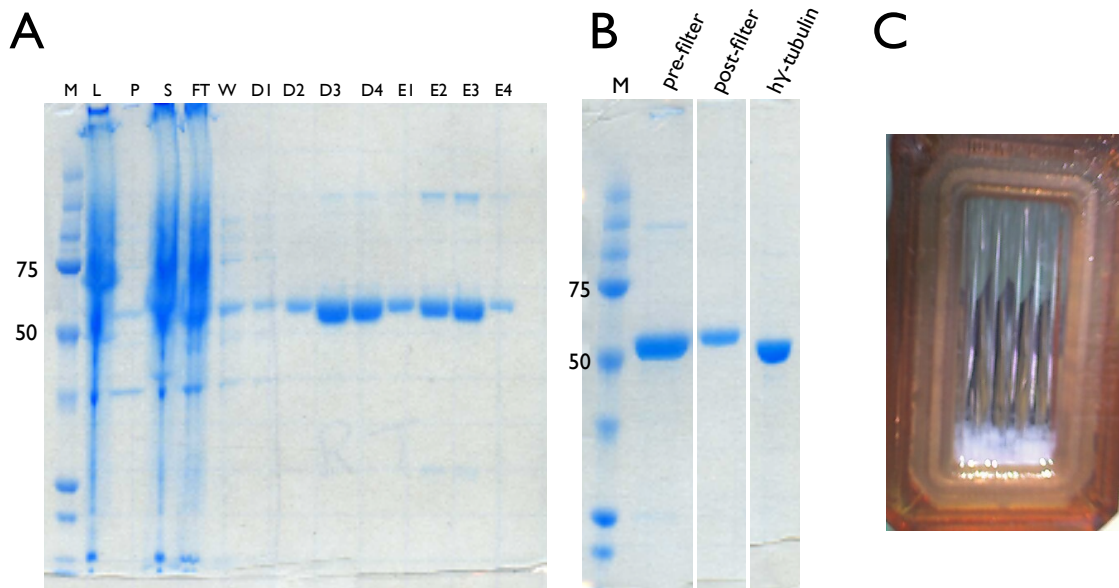


Figure 8. Denaturing Tub4p-pET29b prep. A SDS-PAGE of denaturing prep (M) Marker, (L) Lysate, (P) Pellet, (S) Clarified Supernatant, (FT) Flowthrough NiNTA column, (W) Wash NiNTA column, (D1-D4) refolding dialysis steps, (E1-E4) Elutions from NiNTA column. B SDS-PAGE of pre- and post-filtered protein from final dialysis re-folding step. C photograph of final dialysis step.

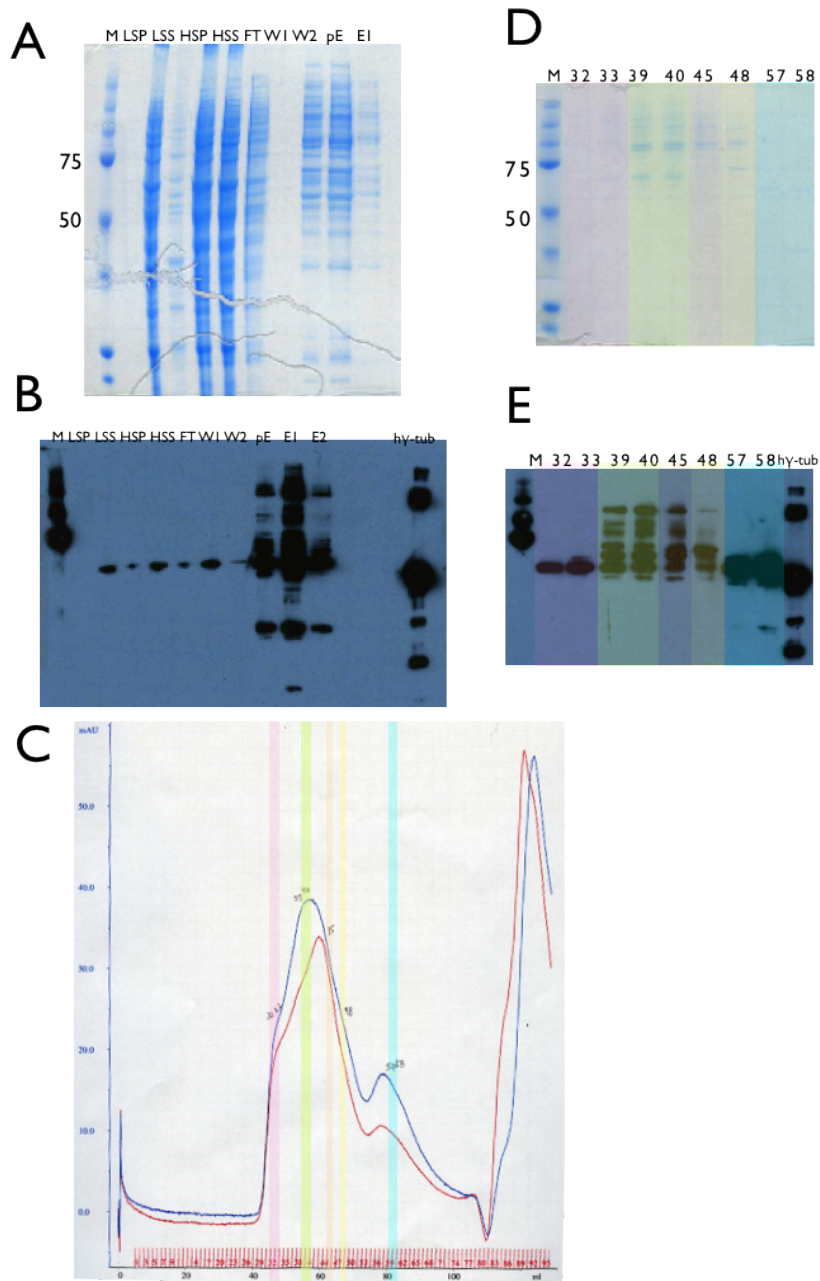


Figure 9. Prep of his-tagged Tub4p from baculovirus infected sf9 pellet. A, B. SDS-PAGE and western of prep until elution from NiNTA column. C Chromatogram of eluate of NiNTA column run on S200 16/60 sizing column, red, 260nm, blue, 280nm. D, E SDS-PAGE and western of selected fractions from sizing column. Westerns use anti-his antibodies.

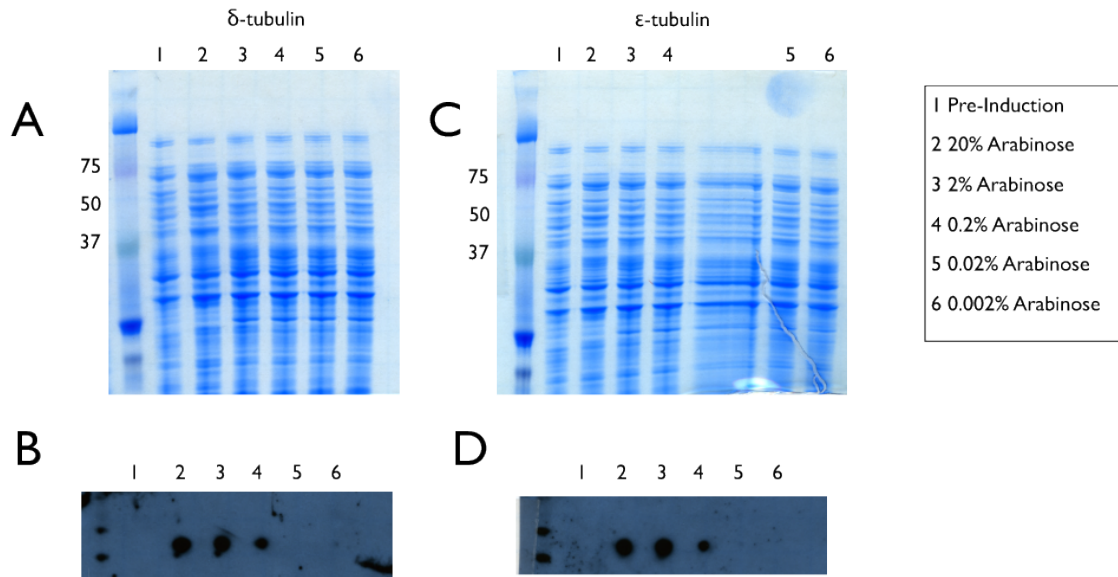


Figure 10. Over-expression of his-tagged δ - and ϵ -tubulin in pBAD expression vector. A and B SDS-PAGE and western (anti-his-tag) of differing amounts of induction with arabinose of δ -tubulin. C and D SDS-PAGE and western (anti-his-tag) of differing amounts of induction with arabinose of ϵ -tubulin.

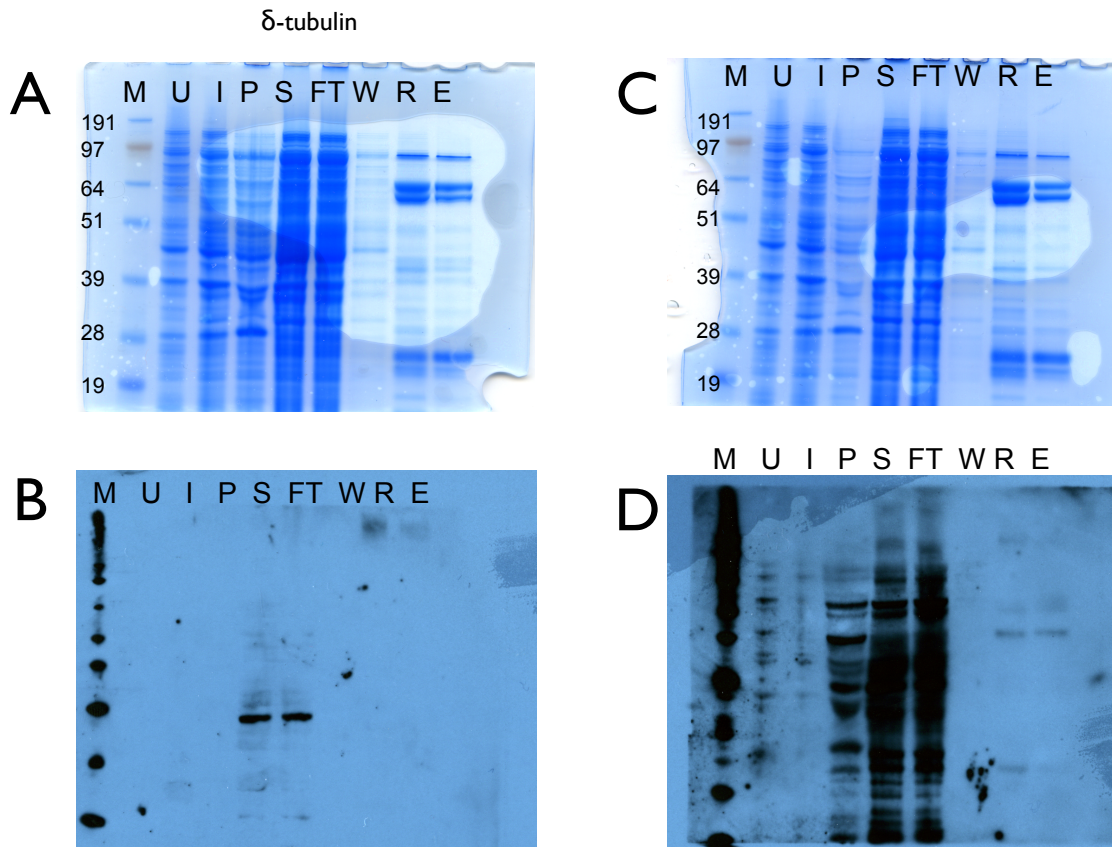


Figure 11. Test purification of his-tagged δ - and ϵ -tubulin in pBAD expression vector. A and B SDS-PAGE and western (anti-his) of differing amounts of induction with arabinose of δ -tubulin. C and D SDS-PAGE and western (anti-his) of differing amounts of induction with arabinose of ϵ -tubulin. In all (M) Marker, (U) Pre-induction, (I) Post-induction, (P) Pellet, (S) Clarified lysate, (FT) NiNTA Flowthrough, (W) NiNTA wash, (R) NiNTA Resin, (E) NiNTA Eluate.

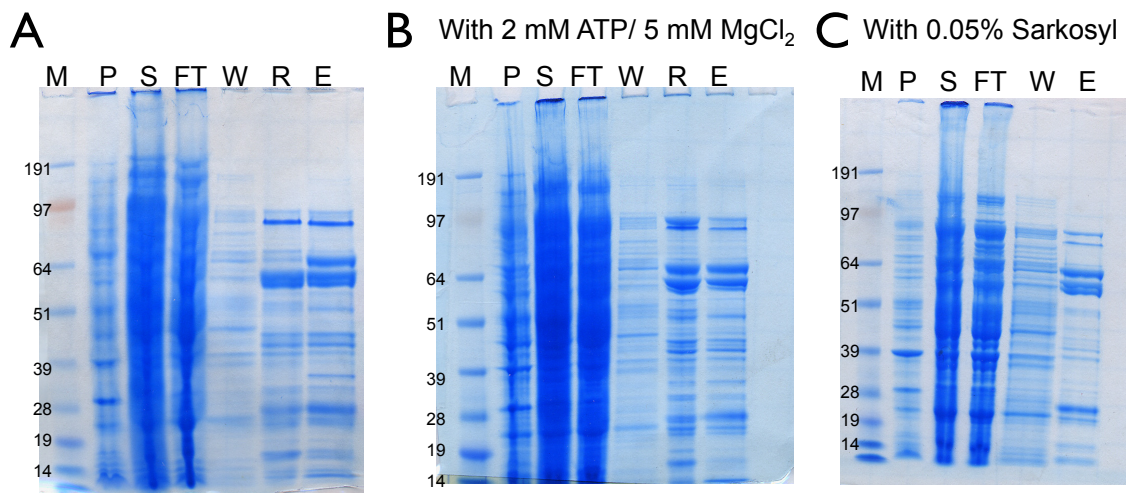


Figure 12. δ -tubulin purification trials. A SDS-PAGE of a 'standard' NiNTA prep. B SDS-PAGE of NiNTA prep with ATP and MgCl₂ added to release chaperones. C SDS-PAGE of NiNTA prep with detergent Sarkosyl. In all, (M) Marker, (P) Pellet, (S) Clarified Lysate, (FT) NiNTA flowthrough, (W) NiNTA wash, (R) NiNTA resin, (E) NiNTA eluate.

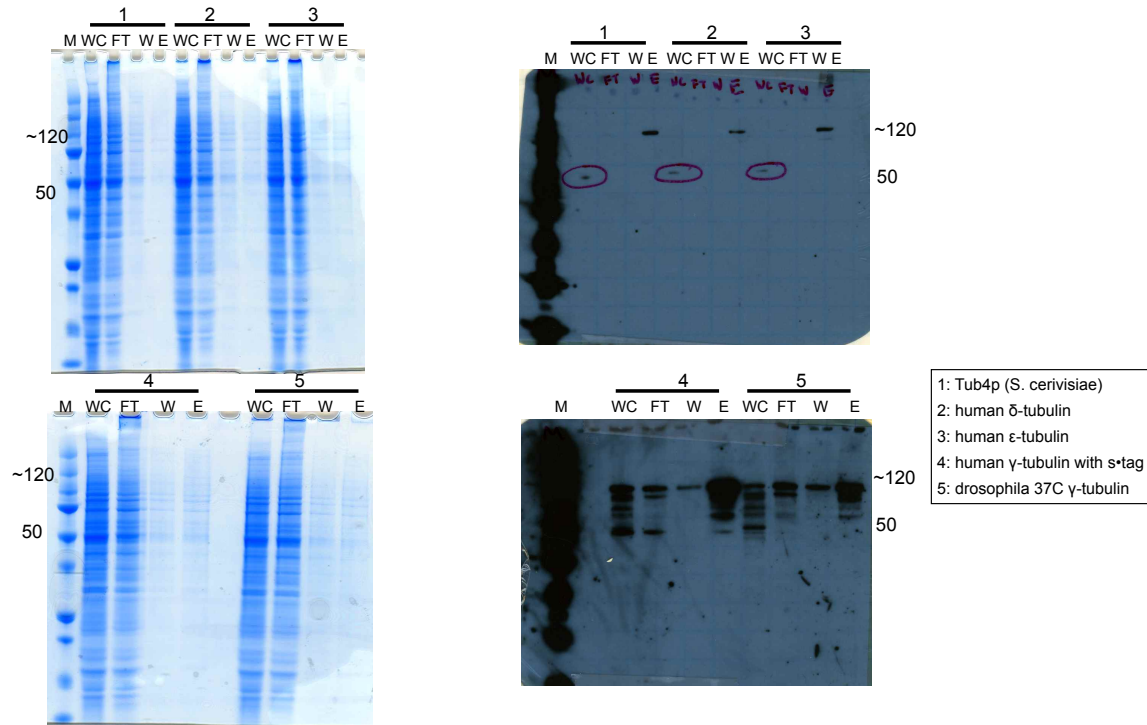


Figure 13. Purification from baculovirus constructs from sf9 cells. A SDS-PAGE and B westerns using anti-His antibodies of 5 different protein constructs. (M) Marker, (WC) Whole cell, (FT) NiNTA flowthrough, (W) NiNTA wash, (E) NiNTA eluate.

References

1. Kollman JM, Polka JK, Zelter A, Davis TN, & Agard DA (2010) Microtubule nucleating gamma-TuSC assembles structures with 13-fold microtubule-like symmetry. *Nature* 466(7308):879-882 .
2. Moritz M, Braunfeld MB, Guenebaut V, Heuser J, & Agard DA (2000) Structure of the gamma-tubulin ring complex: a template for microtubule nucleation. *Nat Cell Biol* 2(6):365-370 .
3. Moritz M, Braunfeld MB, Sedat JW, Alberts B, & Agard DA (1995) Microtubule nucleation by gamma-tubulin-containing rings in the centrosome. *Nature* 378(6557):638-640 .
4. Stearns T, Evans L, & Kirschner M (1991) Gamma-tubulin is a highly conserved component of the centrosome. *Cell* 65(5):825-836 .
5. Stearns T & Kirschner M (1994) In vitro reconstitution of centrosome assembly and function: the central role of gamma-tubulin. *Cell* 76(4):623-637 .
6. Zheng Y, Wong ML, Alberts B, & Mitchison T (1995) Nucleation of microtubule assembly by a gamma-tubulin-containing ring complex. *Nature* 378(6557):578-583 .
7. Kollman JM, Merdes A, Mourey L, & Agard DA (2011) Microtubule nucleation by gamma-tubulin complexes. *Nat Rev Mol Cell Biol* 12(11):709-721 .
8. Gonczy P (2012) Towards a molecular architecture of centriole assembly. *Nat Rev Mol Cell Biol* 13(7):425-435 .
9. Li S, Fernandez JJ, Marshall WF, & Agard DA (2012) Three-dimensional structure of basal body triplet revealed by electron cryo-tomography. *Embo J* 31(3):552-562 .

10. Song YH & Mandelkow E (1995) The anatomy of flagellar microtubules: polarity, seam, junctions, and lattice. *J Cell Biol* 128(1-2):81-94 .
11. Haren L, *et al.* (2006) NEDD1-dependent recruitment of the gamma-tubulin ring complex to the centrosome is necessary for centriole duplication and spindle assembly. *J Cell Biol* 172(4):505-515 .
12. Dutcher SK & Trabuco EC (1998) The UNI3 gene is required for assembly of basal bodies of *Chlamydomonas* and encodes delta-tubulin, a new member of the tubulin superfamily. *Mol Biol Cell* 9(6):1293-1308 .
13. Goodenough UW & StClair HS (1975) BALD-2: a mutation affecting the formation of doublet and triplet sets of microtubules in *Chlamydomonas reinhardtii*. *J Cell Biol* 66(3):480-491 .
14. McKean PG, Vaughan S, & Gull K (2001) The extended tubulin superfamily. *J Cell Sci* 114(Pt 15):2723-2733 .

Chapter 4

Bacterial tubulin TubZ-Bt transitions between a two-stranded intermediate and a four-stranded filament upon GTP hydrolysis

Abstract

Cytoskeletal filaments form diverse superstructures that are highly adapted for specific functions. The recently discovered TubZ sub-family of tubulins is involved in type III plasmid partitioning systems, facilitating faithful segregation of low-copy number plasmids during bacterial cell division. One such protein, TubZ-Bt, is found on the large pBtoxis plasmid in *Bacillus thuringiensis*, and interacts via its extended C-terminus with a DNA adaptor protein TubR. Here, we use cryo-electron microscopy to determine the structure of TubZ-Bt filaments and light scattering to explore their mechanism of polymerization. Surprisingly, we find that the helical filament architecture is remarkably sensitive to nucleotide state, changing from two-stranded to four-stranded depending on the ability of TubZ to hydrolyze GTP. We present pseudo-atomic models of both the two- and four-protofilament forms based on cryo-electron microscopy reconstructions (10.8Å and 6.9Å, respectively) of filaments formed under different nucleotide states. These data lead to a model in which the two-stranded filament is a necessary intermediate along the pathway to formation of the four-stranded filament. Such nucleotide-directed structural polymorphism is to our knowledge an unprecedented mechanism for the formation of polar filaments.

Introduction

The tubulin family of cytoskeletal proteins plays important roles in both eukaryotic and prokaryotic cells. $\alpha\beta$ -Tubulin dimers form microtubules in eukaryotic cells that are necessary for cell division, but also for intracellular transport. The most common prokaryotic tubulin, FtsZ, plays an essential role in cytokinesis and is found ubiquitously in

bacteria, and also in many archaea. Additionally, a diverse set of less conserved tubulin family members have been identified including a variety of monomeric eukaryotic tubulins (γ -, δ -, ϵ -, ζ -, and η -) (1), the $\alpha\beta$ -tubulin-like heterodimer BtubA/B (2), the prokaryotic extrachromosomal TubZs involved in plasmid segregation (3-5), and the recently discovered bacteriophage encoded tubulins, PhuZ (6, 7).

Amongst eukaryotic $\alpha\beta$ -tubulins, sequence identity is quite high (75-85%), as it is also amongst FtsZs (40-50%) (8). However, sequence identity between eukaryotic and prokaryotic family members is quite low (10-20%), and new tubulins are often discovered using only the limited number of highly conserved residues involved in nucleotide binding and hydrolysis. Despite this sequence diversity, the core structures of individual tubulin subunits are extraordinarily well conserved, and this structural conservation extends to the longitudinal interactions between monomers (9). By contrast, such striking structural conservation stops at the protofilament level: $\alpha\beta$ -tubulin forms tubes of varying protofilament number (10), FtsZ forms a variety of straight and curved protofilament structures (11), and BtubA/B forms 5 protofilament structures (12). The lack of conservation of residues involved in lateral interactions has allowed the evolution of diverse higher-order filament structures whose organization and dynamics are precisely tuned to their cellular function.

The TubZ tubulin family, discovered recently on several *Bacillus* virulence plasmids (4, 5) and in a Clostridial bacteriophage (3), is a group of proteins involved in bacterial plasmid partitioning (*par*) systems. At their core, *par* systems contain a polymer-forming NTPase, a DNA-binding protein, and a centromeric binding site on the DNA (13, 14). Together these components ensure that low-copy number plasmids are efficiently

segregated to both daughter cells during cell division. The TubZ found on the pBtoxis plasmid from *B. thurigiensis* (TubZ-Bt) has been shown to treadmill (growing at one end, while shrinking at the other end), and these dynamics are important for proper plasmid segregation (15). Additionally TubZ-Bt assembly has been monitored *in vitro* by light scattering (16) and crystal structures have been solved in the presence of GDP, GTP γ S and in the apo state (17, 18).

TubZ-Bt acts in concert with the TubR helix-turn-helix DNA binding protein, (18, 19), and binds to a centromeric region of the plasmid DNA, *tubC*, which contains 7 12-bp pseudorepeats. The TubRC complex binds in an unknown manner to the C-terminus of TubZ (residues ~407-484). Additionally, a new protein located downstream of *tubZRC*, named TubY, was recently implicated in the function of the *C. botulinum* bacteriophage c-st TubZ. TubY stabilizes the assembly of TubZ filaments alone, but depolymerizes TubZ assembled in the presences of the TubRC complex. Other TubZ systems, including TubZ-Bt, have been found to have a similar protein located upstream of the operon (3), but it is unknown whether this putative TubY plays a role in pBtoxis TubZRC plasmid segregation.

Here we show that the filament morphology of TubZ-Bt is linked to nucleotide state. Untagged TubZ-Bt forms almost exclusively four-stranded helical filaments *in vitro* in the presence of GTP, whereas the previously observed (16-18) two-stranded filaments only accumulate under conditions where GTP hydrolysis is blocked. We present ~11Å and ~7Å resolution cryo-electron microscopy (cryo-EM) reconstructions of the helical structure of TubZ-Bt grown in the presence of GTP or GTP γ S respectively. We can unambiguously fit the TubZ-Bt crystal structure into both of these filament morphologies to form detailed pseudo-atomic models. We observe that removing the extreme C-terminus of the protein

compromises or abrogates filament assembly, although the majority of these residues are unresolved in the reconstructions. These structures, coupled with additional biochemical and mutational studies, lead to a model in which TubZ-Bt forms an unstable two-stranded intermediate on pathway to the formation of highly stable four-stranded filaments that is only reached upon GTP hydrolysis.

Results

TubZ filament morphology is affected by nucleotide state

During early experiments to understand the kinetics of TubZ-Bt, we observed that an N-terminally tagged TubZ-Bt, with six residues before the start methionine, exhibited extremely poor polymerization in the presence of GTP when compared to a C-terminally tagged construct. Previous studies had used an N-terminally tagged construct for polymerization studies (16) and a C-terminally tagged construct for structural studies (17). Because the extreme C-terminus has been shown to be important for binding to TubRC complexes, we cloned, expressed and purified an untagged version of wild-type TubZ. Quantitatively comparing the polymerization ability of these different proteins using 90-degree light scattering in the presence of GTP revealed that C-terminally tagged protein exhibited strong polymerization, whereas the N-terminally tagged protein showed almost no polymerization (Fig 1a). By contrast, untagged TubZ showed an even more robust polymerization than the C-terminally tagged construct, reaching a nearly doubled plateau value (Fig 1a). As this seemed at odds with previously published data, we next compared the polymerization kinetics of all three constructs (N- tagged, C-tagged, untagged) in the

presence of the non-hydrolyzable GTP analog GTP γ S by 90-degree light scattering. We observed that although all constructs show similar rapid polymerization with GTP γ S (Fig 1b), they plateau at a much lower scattering value than the assembly of untagged TubZ with GTP. GDP alone did not appear to polymerize TubZ to any detectable degree (Fig 1b).

To test the possibility that the observed lower plateaus with GTP γ S were due solely to an unfavorable interaction with the non-hydrolysable analog, the catalytic aspartate on the T7 loop of TubZ was mutated (D269A) to abolish GTP hydrolysis allowing us to directly assess the impact of hydrolysis. This mutant contains a C-terminal His-tag as the fully untagged D269A mutant proved refractory to purification. Notably, TubZ-D269A in the presence of GTP showed a polymerization curve comparable to that of GTP γ S, with a similarly low plateau value (Fig 1b).

Two possibilities exist to explain the striking differences in observed light scattering plateau values. One possibility is that without hydrolysis, polymerization is somehow stunted – fewer polymers are formed, leading to a commensurate loss of signal. A second possibility is that the two filaments have different morphologies, with the GTP filament scattering more strongly (they are wider or longer) than the GTP γ S/D269A TubZ filaments. The first possibility was tested by pelleting filaments polymerized using either GTP or GTP γ S. Surprisingly, we observed that a greater percentage of TubZ polymerizes in GTP γ S than in GTP, clearly showing that the lower plateau in light scattering cannot be a consequence of decreased polymer formation (Fig 1c). To test the second possibility, TubZ filaments formed in the presence of either GTP or GTP γ S were examined by negative stain EM. Surprisingly, untagged TubZ polymerized with GTP predominantly formed thick filaments, ~ 120 Å in diameter (Fig. 1e), whereas polymerization with GTP γ S led to the

thinner two-stranded filaments (Figs. 1d,f) observed by previous groups (16, 17), although short thicker regions were occasionally observed. The ratio of filament types observed for TubZ-D269A in the presence of GTP or GTP γ S was comparable to that in the WT-GTP γ S sample, indicating that GTP hydrolysis must play a fundamental role in determining TubZ-Bt filament morphology (Figs 1d-f, Fig. S1), and that the two-stranded species is not an artifact of using a nucleotide analog.

TubZ-Bt filaments are able to interconvert between filament forms

Two-stranded filaments dominate TubZ preparations containing GTP γ S, but thicker segments are also present (17). Whether two-stranded filaments emerge from the thicker filaments or vice versa was unclear. We boxed out these branching sites for analysis, and it appears that the two-stranded filaments emerging from thicker filaments have a similar morphology to unattached two-stranded filaments. Thick filaments predominate when assembling TubZ in the presence of GTP (Fig. 1e). However, if the two-stranded form were an intermediate to the thicker filaments, it might be possible to stabilize two-stranded filaments in the presence of GTP by either adding glycerol or forming filaments directly on carbon-coated grids rather than in solution before visualization, helping trap early intermediates. Using these strategies we were able to visualize two stranded filaments leading in and out of thicker filaments, suggesting that the two-stranded filaments are transient intermediates in the formation of the thick filaments (Fig. S2).

Helical Reconstruction of TubZ four-stranded filaments by Cryo-electron microscopy

To further understand the structure of both filament types we performed cryo-EM reconstructions using iterative helical real space refinement (IHRSR) (20, 21). The WT TubZ-GTP filaments were reconstructed to a resolution of 6.9 Å by the 0.143 FSC criteria using “gold-standard” refinement (22) (Fig. S3a). The TubZ-GTP filaments consist of four parallel protofilaments with four-fold planar symmetry (Fig. 2). The fiber has an outer diameter of ~120 Å, and an inner diameter of ~19 Å, showing no strand-strand contacts across the lumen. The helical symmetry has a rise of ~43.5 Å and an azimuthal angle of ~31.8°. Crystal structures of TubZ fit quite well into the density of the reconstruction (Fig. 2b,c). This indicates that that no large intra-monomer conformational changes occur upon polymerization, suggesting the difference in four- and two-stranded morphologies is dictated largely by inter-monomer conformational changes. Subtle adjustments to the structure of the loop between H6 and H7, and H11 (Fig. 2) were made using the program Flex-EM (23). An alignment between the individual chains of the filamentous crystal structures highlights this range of structural conformations, and we observe that our modified structure falls well within the conformation range (Fig. S3c). Density in the EM map for the T3 loop is quite weak, and we were unable to place the residues accurately in this area. Comparison of our density at a low contour level with the two conformations observed in the crystal structure show that the conformation is likely in an intermediate conformation (Fig. S3e).

The important and generally well-conserved protofilament longitudinal interactions can be clearly observed and are comparable to those observed in the filamentous crystal structures. The rotation between longitudinal pairs in the four-stranded filament is most

consistent with the rotation of those of the GDP crystal structure (31.8° versus 30° respectively)(17). One feature highlighted by Aylett et al was a motion of helix H2 upon coordination of Mg⁺⁺ in the TubZ nucleotide-binding pocket (17). They observed that helix H2 takes on an 'in' conformation with aspartate 64 coordinating with the Mg⁺⁺ in the binding pocket, while H2 is in an 'out' conformation with the Mg⁺⁺ absent. In our EM structure, the density of the helix is clearly in the 'out' position, indicating that Mg⁺⁺ is likely missing from the binding site, despite saturating amounts in the polymerization buffer, supporting the expectation that GTP would be hydrolyzed in the four-stranded filaments corresponding to a GDP state (Fig. S3b). Consequently, we will refer to this four-stranded filament grown from GTP as the GDP-state.

We were able to directly visualize lateral contacts between adjacent protofilaments. The lateral contacts form two charged surfaces (Fig. S5a) in one layer. Helices 6, 9, and 10, in addition to the loop between H6 and H7, forming one side of interface, and residues on loops S9-S10, H1-S2 forming the other (Fig. S5a). The N-terminal helix H0 is also found in this interface, explaining the sensitivity of the four-stranded form to N-terminal purification tags, whereas the C-terminus is on the outside surface of the filament (Fig. 2). In addition, the residues on H9 and H10 of the 0 monomer are potentially interacting with the residues between H2-S3 on the adjacent layer (+1 monomer).

Helical Reconstruction of TubZ two-stranded filaments by Cryo-electron microscopy

In order to understand the relationship between the two filament forms, we also performed a helical reconstruction of the TubZ-GTP γ S filaments. To optimize formation of

the two-stranded filaments, an N-terminally tagged construct was used in addition to GTP γ S. The filaments were reconstructed to a resolution of 10.8 Å by the 0.143 FSC criteria (Fig. S4a). TubZ-GTP γ S filaments refine to a helical rise of 22 Å and an azimuthal angle of 191.8°. Unlike the TubZ-GDP state, the two protofilaments are offset from each other by a half a monomer length (Fig. 2). As in the four-stranded filament, we see that the longitudinal interactions are similar to those previously observed. The distance between longitudinally interacting monomers on the same strand is 44 Å, as dictated by the helical symmetry (For clarity we will refer to the monomers along the same strand as 0, +1, etc.). The long C-terminal helix of TubZ H11, and the N-terminal helix H0 are both exposed to solution on non-luminal, non-external opposite flat sides of the filament, which we designate the H4-H5 and N (for N-terminal) interfaces, respectively (labeled in Fig. S4D). Surprisingly, there is a limited amount of density at the luminal junction of the two protofilaments. As with the four-stranded interface, this two-stranded interface is laced with charged residues (Fig. S5b). The positioning of the cross-strand monomers suggest interactions between H9 and H10 on one monomer and H6 and H11 of the opposite monomer (Fig. S4), although with the current configuration of residues on these helices in the crystal structure, it is hard to pinpoint definitively which residues are interacting.

Comparison of two- and four-stranded filaments

We compared the two filament forms in order to gain insight into the mechanism of filament assembly and the role of GTP binding and hydrolysis in the process. While longitudinal interactions are generally well conserved, our EM structures reveal small but important differences between the longitudinal arrangements in the two- and four-

stranded polymers (Fig. 3). The two-stranded filament has a significantly smaller inter-monomer twist angle ($\sim 23.8^\circ$) versus the four-stranded filament ($\sim 31.8^\circ$). This is similar to, but more exaggerated than the differences observed between the protofilament crystal forms of GTP γ S ($\sim 25.7^\circ$) and GDP (30°) (17), more precisely representing the dictates of the respective filament forms. By contrast the longitudinal rise along the protofilament axes are nearly identical, only differing by $\sim 0.5\text{\AA}$. The difference in twist angle can be explained by looking at an alignment of the bottom monomer of a longitudinal pair fit into our two maps (Fig. 3). This reveals a hinge-like opening motion as you transition between the GTP γ S and GDP filament forms. The 'closed' conformation of the GTP γ S interaction allows for a tighter twist angle. The two interfaces which form the GTPase pocket open approximately $\sim 12^\circ$ between the two- and four-stranded structures. This moves the catalytic aspartate (residue 269) in the T7 loop of the +1 monomer further away from the location of the guanosine phosphate in the GTP binding site of the +0 monomer (Fig 4), suggesting that the two-stranded filaments are in a hydrolysis competent state. By contrast, the distance of D269 to the predicted location of the guanosine phosphate in the GTP binding site of the +0 monomer would be considerably larger ($\sim 10\text{\AA}$ versus 7\AA). This suggests that the interaction with the guanosine phosphate in the GTP binding site of the +0 monomer suggests that the interaction is in a 'closed' conformation, capable of forming the intermediary two-stranded morphology. Post-hydrolysis, this interaction is broken, and the longitudinal pairs 'open', forming the four-stranded filament structure. This observation, together with the position of H2 again supports that the four-stranded filament is in a post-hydrolysis, GDP state, and the two-stranded filament is in pre-hydrolysis state, consistent with results showing that the TubZ filaments grown in GTP contain mostly GDP (16).

Location and importance of extended C-terminal tail

An important feature missing in the crystal structures is the extended C-terminal tail of TubZ-Bt, with the electron density only extending to residue 421 of 484 residues. This tail is necessary for interaction with TubRC complexes (18) and is highly charged. We anticipated the TubZ reconstructions would provide extra information about the structure and possible interactions of the C-terminal tail. However, density in the four-stranded reconstruction ends around residue 414, and little density beyond that expected for the crystal structure is visible anywhere in the map, even at a low contour level (Figs. 2c, 5a, S8a).

By contrast, several prominent density features that cannot be accounted for by the crystal structure are seen in the two-stranded reconstruction. Unlike the four-stranded structure, density for H11 is visible at least up to limit seen in the crystal structure (421). Notably, extra density (especially in the difference map, Fig S8b) seems to extend beyond the end of the H11 emerging from the +0 monomer, but making contact with the +1 monomer. There is also additional density on the +2 monomer along a single protofilament (Fig. 4b, Fig. S8b). Owing to the resolution of the reconstruction and the predicted lack of structure in this region, we were unable to convincingly model this area, but propose that both of these major regions of extra density arise from a continuation of the C-terminal tail of the +0 monomer. This suggests that C-terminal tail interactions along the protofilament could be important in the formation of the two-stranded filament.

To investigate the functional importance of the C-terminal tail for polymerization several tagless truncations of varying lengths (1-442, 1-460, and 1-470) were cloned, expressed and purified. These mutants were first characterized by light scattering to confirm their activity. To our surprise, even a 14-residue truncation (1-470) seriously compromised the polymerization kinetics of TubZ, both in the presence of GTP and GTP γ S (Fig. 4c and d). Removing another 10 residues (1-460) further impairs polymerization, while removal of 42 residues (1-442), completely abolishes observable polymerization of either form at concentrations comparable to full-length protein. By negative stain EM, the filament morphologies of truncated constructs 1-470 and 1-460 are identical to that seen with full-length filament (Fig. S9), however at substantially lower abundance.

The two-stranded TubZ filament is on pathway to the four-stranded filament

We observed that C-terminal truncations comparably affected TubZ polymerization efficiency in the presence of GTP or GTP γ S, while the expectation from the degree of C-terminal contacts made in the four- and two-stranded filaments would suggest a much larger affect on the formation of the two-stranded filament. This, along with the structural differences described above, lead to a model in which a two-stranded, pre-hydrolysis intermediate is a necessary pre-requisite to formation of the mature four-stranded post-hydrolysis filament. The existence of such a transient two-stranded intermediate is also supported by our visualizations of the two-stranded filament branching into and out of four-stranded filaments. Given that a requirement for such a structurally different intermediate in tubulin family assembly is unprecedented, we pursued evidence for this transition through mutations.

Because we had observed that adding residues on the N-terminus disrupted formation of the four-stranded TubZ filament, we designed a set of point mutations based on our structure that should preferentially compromise the four-stranded filament. To have a robust affect, three lysines on a loop adjacent to the N-terminus in the four-stranded filament were mutated to alanines (K224A/K227A/K230A [3K]). As observed by negative stain EM, this mutation prevents polymerization in the presence of GTP. Notably, in the presence of GTP γ S, mutant TubZ polymerizes similarly to wild-type protein, forming two stranded filaments. In addition, single protofilaments can also be seen on grids of TubZ-3K, implying that these residues might be weakly involved in stabilizing the two-stranded filament via luminal interactions (Fig. S7). These observations further support the proposal of the two stranded filaments being on pathway to the four-stranded form.

Discussion

Bacillus thuringiensis TubZ forms distinct two- and four-stranded species

Our results show that TubZ-Bt forms four-stranded filaments *in vitro*, in the presence of the native substrate GTP, while assuming a predominantly two-stranded conformation in the presence of the non-hydrolyzable nucleotide analog GTP γ S. We propose that both conformations are biologically relevant with the two-stranded form being a transient intermediate on the pathway to the four-stranded state. Previous reports have focused on the two-stranded form, either because of their use of GTP γ de(17) or their use of N-terminally tagged protein (16, 18). We show here that both of these factors have

an unexpectedly profound effect on filament morphology, either by disruption of critical lateral interfaces or by affecting nucleotide turnover and filament kinetics.

Beyond these overall observations, we determined cryo-EM reconstructions of both filament forms at resolutions of 6.9Å and 10.8Å (four- and two-stranded forms, respectively) allowing the crystal structure of TubZ-Bt to be unambiguously positioned within our experimental density maps. The resultant pseudo-atomic resolution molecular models are notably different from previously published work using negative stain reconstructions (17); this discrepancy is likely due to the higher resolution data available when using cryo-EM, and the lack of features on TubZ-Bt making accurate fitting at low resolution problematic. Our model for the two-stranded filament is rotated roughly 90 degrees from the previous fitting, with H11, and the N-terminus located on opposite surfaces on the side of the lumen of the filament. In an effort to confirm the prior model, the authors sought to determine the location of the C-terminus using a C-terminal GFP tag. While the location of the GFP in their negative stain map was consistent with H11 being on the outside of the filament, the position of GFP is unfortunately a very weak constraint as there are ~60 intervening residues. Indeed, our two-stranded map suggests that a significant portion of the C-terminus binds along the filament and ends up on the external surface, while H11 is located on the luminal interface of the filament.

Effects of nucleotide state on TubZ-Bt filament morphology

We observed that TubZ-Bt filaments have the ability to interconvert between an unstable two-stranded filament and a four-stranded filament. Four observations suggest that the two-stranded filament is an on-pathway intermediate to the formation of the more

stable four-stranded filament: First, blocking the ability of TubZ-Bt to hydrolyze GTP by either mutagenesis or chemical means stabilizes the two-stranded filament and reduces the population of four-stranded filaments. Second, in the presence of GTP the population of two-stranded filaments can be significantly increased by using conditions that would either be expected to trap initial events or stabilize transient species. Third, mutations that disrupt the four-stranded lateral interface but don't impact GTP hydrolysis lead to a loss of polymer in GTP but not in GTP_{gb}, indicating that the two-stranded filaments are unstable after GTP hydrolysis. Lastly, the four-stranded filament structure appears to be in a post-hydrolysis conformation containing GDP, whereas the two-stranded filament is in a pre-hydrolysis conformation. The lack of filament growth in the presence of GDP leads to the supposition that there is an obligate structural intermediate that is in a hydrolysis competent conformation, and allows for formation of the four-stranded filament. This dramatic reconfiguration of filament morphology is an unprecedented mechanism of filament formation (Fig. 5).

In eukaryotic tubulins there is both an intra- and inter-monomer conformational change that has been observed between unassembled $\alpha\beta$ -dimers and $\alpha\beta$ -dimers in the microtubule lattice. This change happens via a piston-like motion of H6 and H7 (24); no such conformational switch has been observed in the crystal structures of TubZ-Bt, nor do we have evidence of it happening in our EM structures. Instead, it appears that the conformational change underlying the different TubZ-Bt filament morphologies is driven by an opening of nucleotide cleft and consequent changes in protofilament twist, implying that the TubZ-Bt:GTP γ S and TubZ-Bt: GDP structures represent pre- and post-hydrolysis states respectively. This motion appears to be based solely on changes in the inter-

monomer interactions, rather than an intra-monomer rearrangement of TubZ-Bt and represents a novel mechanism to couple nucleotide state to filament morphology.

Dramatic rearrangements would have to occur for long stretches of two-stranded filaments to become four-stranded. Changes in longitudinal twist upon GTP hydrolysis must directly disrupt interactions that stabilize the staggered two-stranded state and provide new opportunities for stabilizing four-stranded planar interactions. Whether the pre-existing two strands initially reform as a planar adjacent pair (Fig. S6b) or first separate completely to become diametrically opposed protofilaments (Fig. S6c) within the four-stranded filament, is unclear. Either way, additional subunits would have to add to stabilize the final form.

Given the infrequent visualization of two-stranded filaments of any length under normal conditions, it seems likely that the two-stranded filaments are short in both length and duration. Thus, only a small number of 'closed' protofilaments interactions would need to decouple upon hydrolysis as the 'opening' of longitudinal interactions occurs. Such a model would suggest the possibility of a short two-stranded cap at the growing end of the filament. Determining how the transformation occurs, and looking for a specialized cap structure would shed light on the underlying polymer dynamics by which TubZ-Bt is able to segregate plasmids.

TubZ-Bt polymerization is dependent on the C-terminal tail

It is well known that the C-terminal tail of tubulin family members plays an important role in the binding of accessory proteins. We have shown that even small

truncations of the C-terminal tail induce a dramatic loss of polymerization of the TubZ-Bt filament. Similarly, removal of the C-terminal tail of TubZ-Bc leads to a loss of polymerization (25). Intriguingly, there is no observed density for ~71 residues of this tail in the four-stranded structure, but there is extra density in the two-stranded intermediate that potentially represents at least a portion of the C-terminal tail. It seems most likely that the residues in this density are the residues immediately following those seen in the crystal structures, although parts of the C-terminus may loop out before returning to bind to the +2 subunit. In the context of our model of TubZ polymerization, this suggests that the C-terminal tail may be involved in filament nucleation via longitudinal interactions in the two-stranded filament. We propose that in the 'closed' two-stranded GTP state, the residues C-terminal to H11 are able to form important stabilizing interactions along the protofilaments, between 0, +1 and +2 subunits. Upon hydrolysis, the loss of the D269/ γ -phosphate interaction causes cleft opening, straining the C-terminal interaction, allowing for formation of the more stable four-stranded filament.

It has been observed that the TubRC complex nucleates TubZ filaments (19). The TubRC complex has been shown to bind to the C-terminal tail, and it appears that residues 408-484 have an important effect, although the most dramatic loss in binding comes from the loss of the same 14 residues that have most dramatic effect on TubZ polymerization (18). An intriguing speculation is that the TubRC complex is involved in modulating the interaction of the C-terminal tail with the plus-end subunit as the filament grows. An important future direction is to obtain structural understanding of the interaction between the TubRC complex and the TubZ filament. Does TubR bind on the side of TubZ filaments and act like a tram for the transport of DNA, or does it form a formin-like ring that either

caps or slides along the TubZ filament to facilitate proper location of the pBtoxis plasmid during cell division? Does it facilitate conversion between two- and four-stranded polymers?

TubZ-Bt filaments in the cell

Previous whole cell tomography data suggest that TubZ-Bt may be two-stranded *in vivo*. These data were collected in *E. coli* cells, with TubZ-Bt overexpressed and in the absence of the TubRC complex (17). Unfortunately we have not yet been able to observe the filament morphology of TubZ-Bt in native cells and in the presence of pBtoxis. We note, however, that we have not been able to identify conditions that eliminate the preferential formation of four-stranded filaments of WT TubZ-Bt in the presence of GTP even when including TubRC.

If TubZ does in fact preferentially form a four-stranded filament in the cell, what would be the purpose of this unique two-stranded intermediate? Whether it helps the fine-tuning of filament dynamics alone or in concert with TubRC and the pBtoxis plasmid or provides a means to better couple TubRC to just the growing end of filaments are two possibilities. A tomographic reconstruction of TubZ-Bt in cells, similar to recent work on BtubA/B filaments (12) would help resolve structural questions that might remain.

Materials and Methods

Detailed methods are provided in SI Materials and Methods. Briefly, TubZ proteins were expressed in *E. coli*. and purified. TubZ polymerization was monitored by 90° light scattering using an in-house designed stopped-flow system monitored at 530 nm. Negative

stain electron microscopy was carried out using 0.75% uranyl formate, and imaged on FEI Tecnai T12. Cryo-electron microscopy was carried out using sample applied to holey carbon grids (C-FLAT, Protochips) frozen in liquid ethane using an FEI Vitrobot. Images of frozen sample were collected on a FEI Tecnai F20 operating at 200 kV with an 8k x 8k TemCam-F816 camera (TVIPS, GmbH). Data were processed using SPIDER, EMAN1.9 and in-house CTF correction software. Reconstructions were performed using Iterative Helical Real Space Refinement (IHRSR).

Acknowledgments

We thank M. Erb and J. Pogliano for the gift of DNA encoding TubZ-Bt, and many discussions, as well as J. Kraemer, S. Li, M. Moritz, R. Choy, D. Southworth, J. Polka and C. Rivera for helpful discussions. We thank Dr. Justin Kollman for EM advice and support throughout this project. M. Braunfeld, C. Waddling and P. Wassam provided assistance with EM and computing facilities. This work was supported by both the NIH (GM031627) and the Howard Hughes Medical Institute.

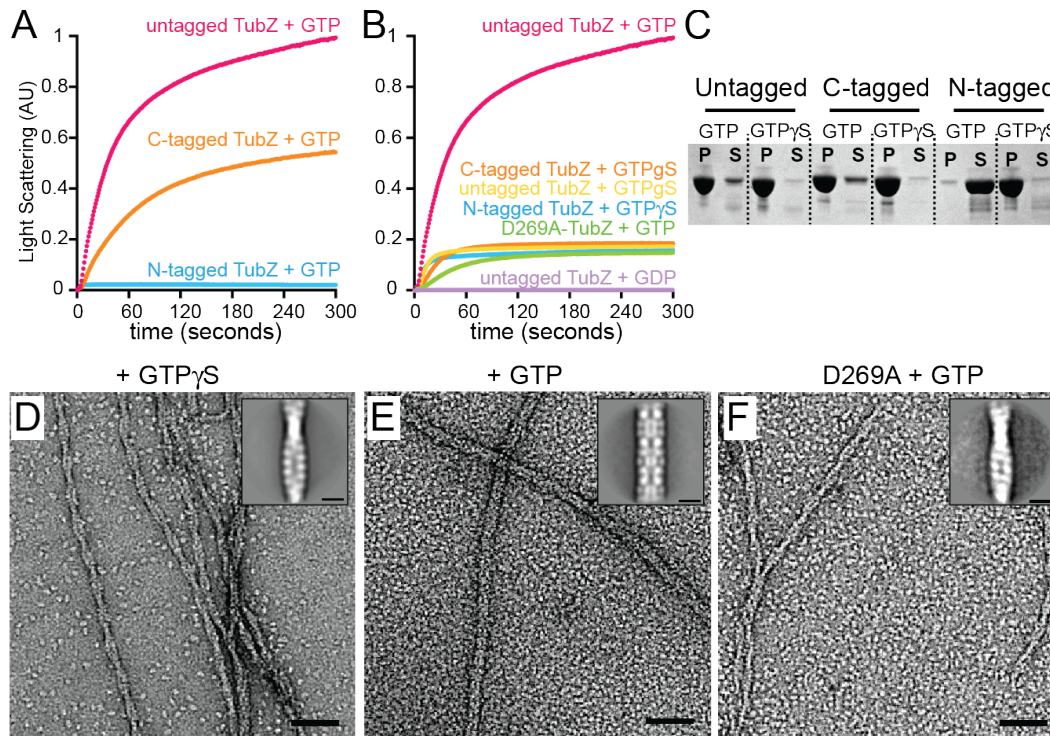


Figure 1. Changes in TubZ-Bt filament morphology and behavior in the presence of terminal tags. (A) and (B) Monitoring polymerization of 3 μ M TubZ by light scattering. (A) N-terminally tagged TubZ in the presence of GTP, C-terminally His₆ TubZ in the presence of GTP, and untagged TubZ in the presence of GTP. (B) N- or C-terminally his-tagged TubZ in the presence of GTP γ S, and untagged TubZ in the presence of GTP γ S, GTP, or GDP. C-terminally His₆ D269A-TubZ (hydrolysis dead) in the presence of GTP. (C) SDS-PAGE of pelleting assays of N- or C-terminally tagged, untagged TubZ in the presence of GTP or GTP γ S. P, pellet; S, supernatant. (D) Micrograph of NS EM of untagged TubZ assembled with GTP γ S, inset is average of boxed two-stranded filaments. (E) NS EM of untagged TubZ assembled with GTP, inset is average of boxed filaments. (F) NS EM of C-terminally his-tagged D269A-TubZ assembled with GTP, inset is average of boxed filaments. Scale bars on micrographs are 50 nm, and 10 nm on inset averages.

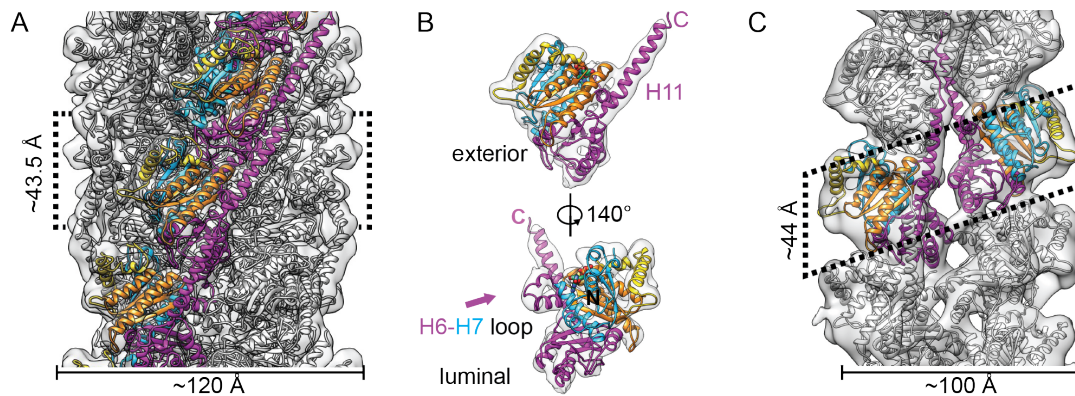


Figure 2. Morphology of TubZ-GTP four-stranded filaments and two-stranded filaments.

(A) cryo-EM TubZ-GTP filament reconstruction. Filament has been low-pass filtered to 7 Å, a B-factor of \sim -309 applied, and high-pass filtered to 30 Å. A pseudo-atomic model is fit, using a structure determined using FlexEM fitting. Residues 0-80 and 236-257 are colored in blue, 81-129 in gold, residues 130-212 in orange, and 213-235 and 258-414 in magenta

(B) Cut-out of one monomer of TubZ from the four-stranded filament. (C) cryo-EM TubZ-GTP_S filament reconstruction. Filament has been low-pass filtered to 11 Å, a B-factor of \sim -452 applied, and high-pass filtered to 35 Å. A pseudo-atomic model is fit using PDB 2XKA chain F. In all, unconnected density has been hidden for improved visualization.

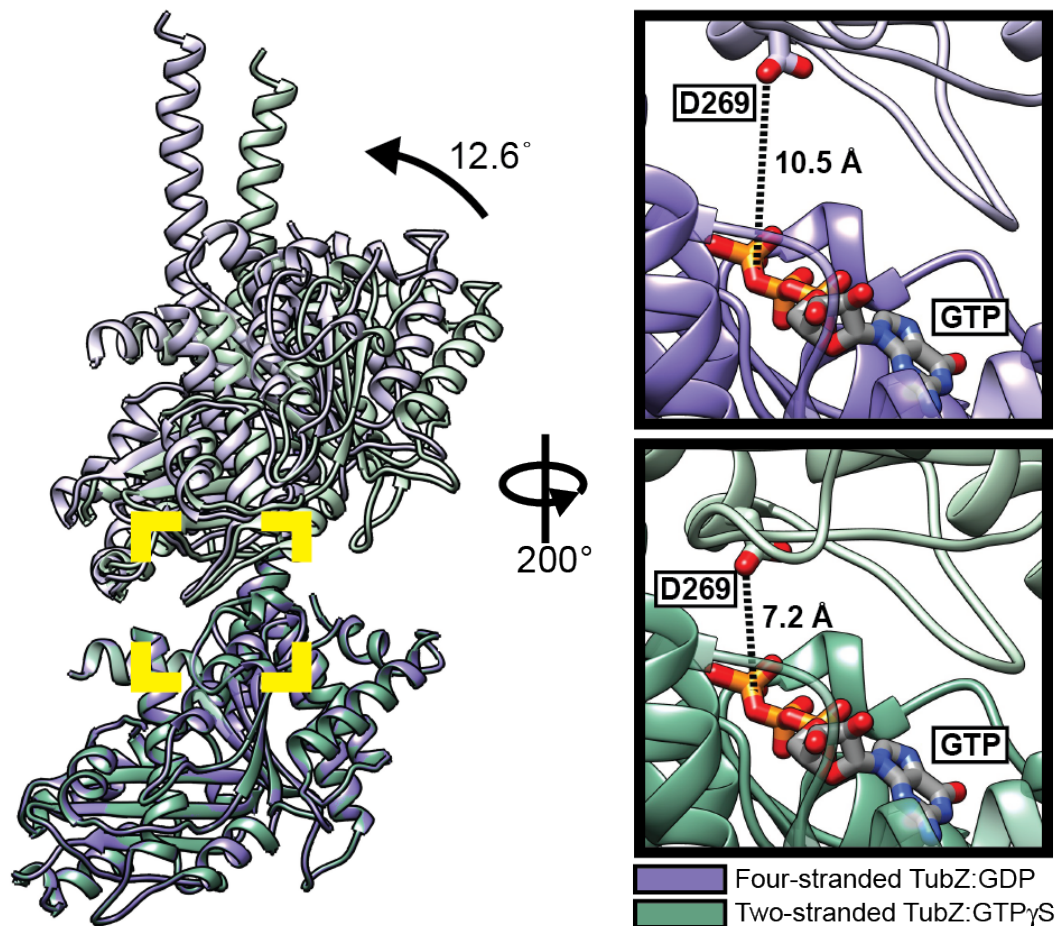


Figure 3. Comparison of longitudinal fits of atomic models of TubZ fit into either the two-stranded reconstruction (in green), or the four-stranded reconstruction (in purple). Structure used for representations in (A) and (B) is PDB 2XKA chain F, with residues from the T3 and H6/H7 loops, as well as some residues at the c-terminus of H11 removed. The angle change between the two models was determined using the difference in the angle between planes of residues 1-383 of the top and bottom chains of each pair. These planes and their angles were generated and measured using UCSF Chimera (26). Insets have the same coloring and show the shortest distance measurement between Aspartate 269 on the T7 loop, and the O3 oxygen of the b-phosphate of GTP.

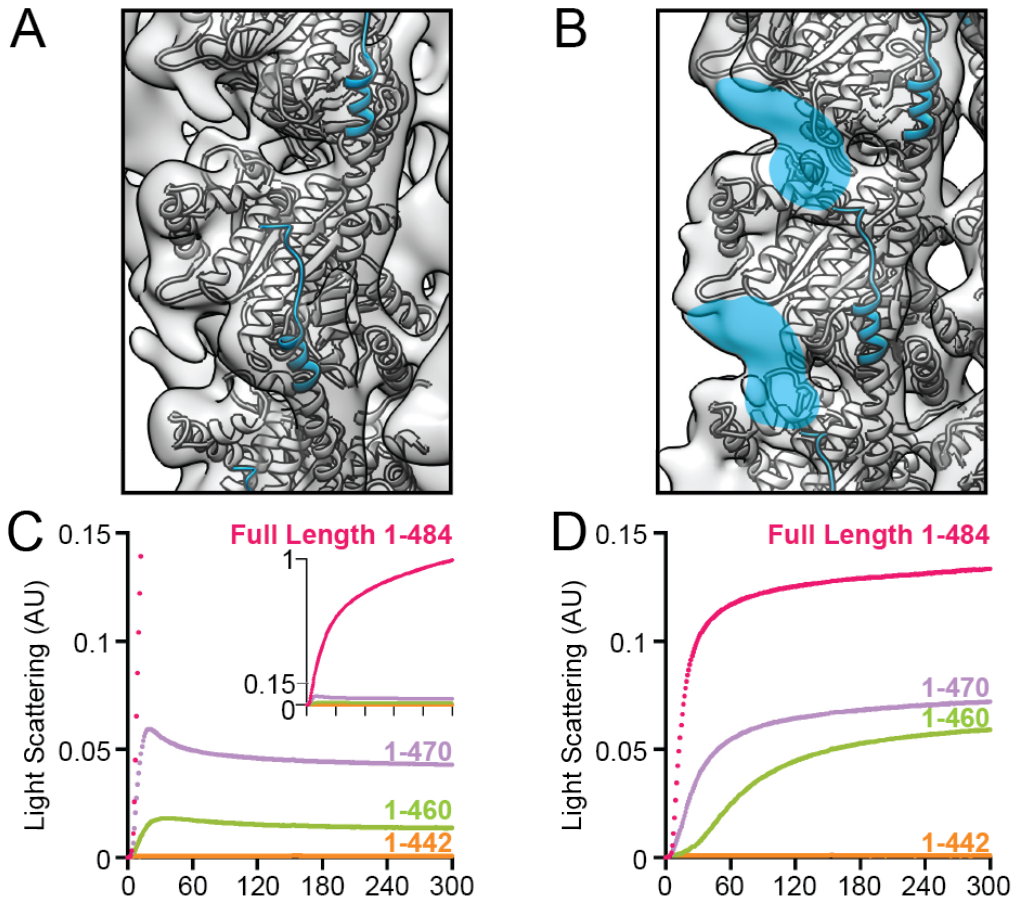


Figure 4. The C-terminal tail of TubZ is important for assembly of both TubZ filament morphologies. (A) Helix H11 is highlighted in blue, with last residues in density (414) shown in spheres. Z-axis has been rotated ~ 19.5 degrees for ease of comparison. (B) Residues 414-421 of Helix H11 are highlighted in blue. Extra density leading from the C-terminal tail is highlighted in blue. Structure used for representations in (A) and (B) is PDB 2XKA chain F, with reconstructions low-pass filtered to 11\AA . (C) and (D) Monitoring polymerization of tail truncations of $3\ \mu\text{M}$ TubZ by 90-degree light scattering. (C) Full length (magenta), 1-470 (purple), 1-460 (green), and 1-442 (orange) untagged TubZ assembled in the presence of GTP. (D) Full length (magenta), 1-470 (purple), 1-460 (green), and 1-442 (orange) untagged TubZ assembled in the presence of GTP γ S.

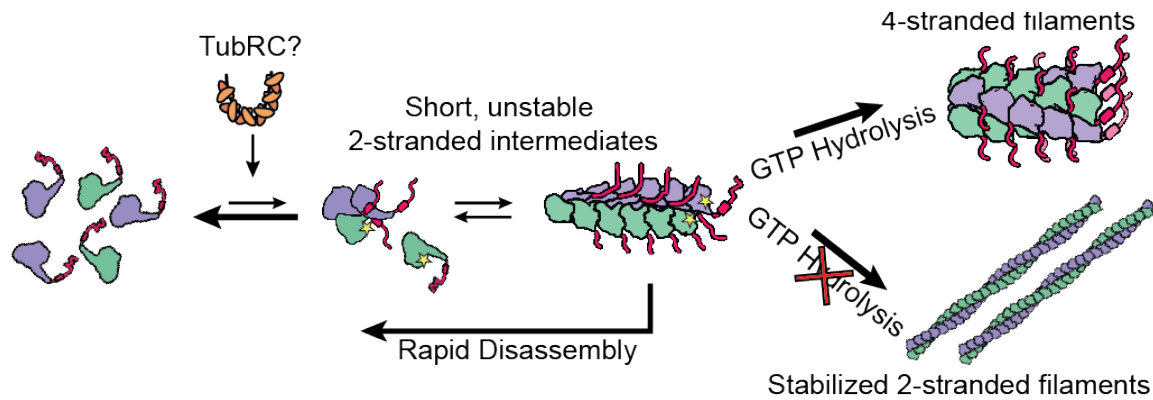


Figure 5 (Model). Model of the polymerization mechanism of TubZ. TubZ monomers assemble into short unstable two-stranded intermediates, and convert into four-stranded mature filaments in the presence of GTP. If nucleotide hydrolysis is blocked either mutationally or chemically, the two stranded filaments are stabilized and able to form long filaments. Formation of four-stranded filaments is diminished, as the conversion from two- to four-strands is slower than the formation of the two-stranded filament.

References:

1. Dutcher SK (2003) Long-lost relatives reappear: identification of new members of the tubulin superfamily. *Curr Opin Microbiol* 6(6):634-640 .
2. Jenkins C, *et al.* (2002) Genes for the cytoskeletal protein tubulin in the bacterial genus *Prostheco bacter*. *Proc Natl Acad Sci U S A* 99(26):17049-17054 .
3. Oliva MA, Martin-Galiano AJ, Sakaguchi Y, & Andreu JM (2012) Tubulin homolog TubZ in a phage-encoded partition system. *Proc Natl Acad Sci U S A* 109(20):7711-7716 .
4. Tang M, Bideshi DK, Park HW, & Federici BA (2006) Minireplicon from pBtoxis of *Bacillus thuringiensis* subsp. *israelensis*. *Appl Environ Microbiol* 72(11):6948-6954 .
5. Tinsley E & Khan SA (2006) A novel FtsZ-like protein is involved in replication of the anthrax toxin-encoding pXO1 plasmid in *Bacillus anthracis*. *J Bacteriol* 188(8):2829-2835 .
6. Aylett CH, Izore T, Amos LA, & Lowe J (2013) Structure of the Tubulin/FtsZ-Like Protein TubZ from *Pseudomonas* Bacteriophage PhiKZ. *J Mol Biol* .
7. Kraemer JA, *et al.* (2012) A phage tubulin assembles dynamic filaments by an atypical mechanism to center viral DNA within the host cell. *Cell* 149(7):1488-1499 .
8. Erickson HP (2007) Evolution of the cytoskeleton. *Bioessays* 29(7):668-677 .
9. Nogales E, Downing KH, Amos LA, & Lowe J (1998) Tubulin and FtsZ form a distinct family of GTPases. *Nat Struct Biol* 5(6):451-458 .
10. Sui H & Downing KH (2010) Structural basis of interprotofilament interaction and lateral deformation of microtubules. *Structure* 18(8):1022-1031 .
11. Erickson HP, Taylor DW, Taylor KA, & Bramhill D (1996) Bacterial cell division

- protein FtsZ assembles into protofilament sheets and minirings, structural homologs of tubulin polymers. *Proc Natl Acad Sci U S A* 93(1):519-523 .
12. Pilhofer M & Jensen GJ (2013) The bacterial cytoskeleton: more than twisted filaments. *Curr Opin Cell Biol* 25(1):125-133 .
 13. Ebersbach G & Gerdes K (2005) Plasmid segregation mechanisms. *Annu Rev Genet* 39:453-479 .
 14. Salje J (2010) Plasmid segregation: how to survive as an extra piece of DNA. *Crit Rev Biochem Mol Biol* 45(4):296-317 .
 15. Larsen RA, *et al.* (2007) Treadmilling of a prokaryotic tubulin-like protein, TubZ, required for plasmid stability in *Bacillus thuringiensis*. *Genes Dev* 21(11):1340-1352 .
 16. Chen Y & Erickson HP (2008) In vitro assembly studies of FtsZ/tubulin-like proteins (TubZ) from *Bacillus* plasmids: evidence for a capping mechanism. *J Biol Chem* 283(13):8102-8109 .
 17. Aylett CH, Wang Q, Michie KA, Amos LA, & Lowe J (2010) Filament structure of bacterial tubulin homologue TubZ. *Proc Natl Acad Sci U S A* 107(46):19766-19771 .
 18. Ni L, Xu W, Kumaraswami M, & Schumacher MA (2010) Plasmid protein TubR uses a distinct mode of HTH-DNA binding and recruits the prokaryotic tubulin homolog TubZ to effect DNA partition. *Proc Natl Acad Sci U S A* 107(26):11763-11768 .
 19. Aylett CH & Lowe J (2012) Superstructure of the centromeric complex of TubZRC plasmid partitioning systems. *Proc Natl Acad Sci U S A* 109(41):16522-16527 .
 20. Egelman EH (2007) The iterative helical real space reconstruction method: surmounting the problems posed by real polymers. *J Struct Biol* 157(1):83-94 .

21. Kollman JM, Polka JK, Zelter A, Davis TN, & Agard DA (2010) Microtubule nucleating gamma-TuSC assembles structures with 13-fold microtubule-like symmetry. *Nature* 466(7308):879-882 .
22. Scheres SH & Chen S (2012) Prevention of overfitting in cryo-EM structure determination. *Nat Methods* 9(9):853-854 .
23. Topf M, *et al.* (2008) Protein structure fitting and refinement guided by cryo-EM density. *Structure* 16(2):295-307 .
24. Ravelli RB, *et al.* (2004) Insight into tubulin regulation from a complex with colchicine and a stathmin-like domain. *Nature* 428(6979):198-202 .
25. Hoshino S & Hayashi I (2012) Filament formation of the FtsZ/tubulin-like protein TubZ from the Bacillus cereus pXO1 plasmid. *J Biol Chem* 287(38):32103-32112 .
26. Pettersen EF, *et al.* (2004) UCSF Chimera--a visualization system for exploratory research and analysis. *J Comput Chem* 25(13):1605-1612 .

Supplementary Information:

SI Methods

Cloning, Protein Expression and Purification

The TubZ gene from plasmid pBtoxis of *Bacillus thuringiensis serovar israelensis* was a kind gift of J. Pogliano (UCSD). The gene was provided cloned into pET28a, and contained the mutation L2V. This mutation was removed by site-directed mutagenesis to generate the C-terminally his-tagged construct used in our studies (WT-TubZ-pET28a). Site-directed mutagenesis on this construct was used to generate the hydrolysis deficient mutant D269A (D269A-TubZ-pET28a). In order to generate the N-terminally tagged construct, TubZ was subcloned into pET151/D-TOPO® (Invitrogen) (WT-TubZ-pET151). This provided a TEV cleavage site, which leaves the residues GIDPFT before the start methionine on the protein after cleavage. Untagged TubZ was then cloned from this construct using inverse PCR to remove all residues before the start methionine of TubZ. The K224A/K227A/K230A mutation and truncations 1-442, 1-460, 1-470 were then made using inverse PCR on the tagless construct (3K-TubZ, TubZ-1-442, TubZ-1-460, TubZ-1-470). All proteins were expressed in either BL21(DE3)star or BL21(RIL) cells, grown at 30° C to OD600 ~0.5, the induced with 1mM IPTG at 16°C overnight. Cells were then pelleted and stored at -80° C until purification.

WT-TubZ-pET28a was purified by lysing a 1 L cell pellet in lysis buffer (100 mM Tris-Cl pH 8.5, 300 mM NaCl), then centrifuged at 35000 x *g* for 45 minutes, and the supernatant was then mixed with NiNTA resin, for 1 h at 4°C. Protein was then eluted (100 mM Tris-Cl pH 8.5, 300 mM imidazole, 100 mM NaCl), and loaded onto an HiTrap Q HP column (100 mM

Tris-Cl pH 8.5, 50-1000 mM NaCl gradient) followed by size exclusion chromatography (S200 16/60, 100 mM Tris-Cl, 150 mM NaCl, 1mM EDTA, 1 mM NaN₃). All protein was dialyzed into HMK100 buffer (50 mM HEPES pH 7.7, 100 mM KAc, 5 mM MgAc₂) prior to biochemistry or electron microscopy.

D269A- TubZ-pET28a was purified by lysing a 2 L cell pellet, resuspended in lysis buffer (50 mM HEPES pH 7.7, 20 mM KAc, cOmplete ® EDTA-free protease inhibitor cocktail (Roche Applied Science), 1 mM DTT), then centrifuged at 35000 x *g* for 45 minutes. The supernatant was then mixed with NiNTA resin, for 1 h at 4°C. Protein was then eluted (50 mM HEPES pH 7.7, 20 mM KAc, 300 mM imidazole), and then run on a size exclusion column (50 mM HEPES pH 7.7, 20 mM KAc).

WT-TubZ-pET151 was purified by lysing a 1 L cell pellet, resuspended in lysis buffer (50 mM HEPES pH 7.7, 300 mM KAc, 5 mM MgAc₂, 10% glycerol, 10 mM thioglycerol), then centrifuged at 35000 x *g* for 40 minutes. The supernatant was then mixed with NiNTA resin, for 1 h at 4°C. Protein was then eluted (50 mM HEPES pH 7.7, 300 mM KAc, 5 mM MgAc₂, 10% glycerol, 10 mM thioglycerol, 300 mM imidazole), and cleaved overnight at room temperature with TEV protease. Protein was then then run on a size exclusion column (50 mM HEPES pH 7.7, 300 mM KAc, 5 mM MgAc₂, 10% glycerol, 10 mM thioglycerol).

Untagged TubZ was purified by was purified by lysing a 1 L cell pellet, resuspended in lysis buffer (50 mM HEPES pH 7.7, 100 mM KCl 5 mM MgCl₂, 1mM DTT), then centrifuged at

~94000 x *g* for 1 hr. Two Ammonium Sulfate cuts were performed, at 25% and 40%. The 40% pellet was resuspended and run over a PD-10 desalting column (GE healthcare) (50 mM HEPES pH 7.7, 100 mM KCl, 10 mM MgCl₂, 1mM DTT). The desalted fraction was then spun at 126,000 x *g* for 15 minutes to remove aggregates. The supernatant was then mixed with 10 mM GTP and then spun again for 15 minutes. The pellet was then resuspended and dialyzed overnight in 1L depolymerization buffer (50 mM HEPES pH 7.7, 20 mM KAc, 5 mM EDTA). Protein was then run on a size exclusion column in same buffer. Collected fractions were then dialyzed against 2L HMK100 buffer (50 mM HEPES pH 7.7, 100 mM KAc, 5 mM MgAc₂) overnight, and then for 4 hours in 2L fresh buffer.

TubZ-1-470 was purified in a manner to similar to wild-type untagged TubZ, but due to its lower ability to polymerize, the polymerization step was inefficient. Both supernatant and pellet of the polymerization were dialyzed overnight, and then run on a size exclusion column followed by a HiTrap Q HP column (50 mM HEPES pH 7.7, 5mM EDTA. 20-1000 mM KAc gradient). Collected Fractions were dialyzed as above.

3K-TubZ, TubZ-1-442, TubZ-1-460 proteins were purified in a similar manner to wild-type untagged TubZ. The first ammonium sulfate cut was performed at 20% for 3K-TubZ, but 25% for all others. After the second cut, the pellet was resuspended and either desalted (3K-TubZ), or dialyzed overnight (TubZ-1-442, TubZ-1-460). The resuspension was then run on a HiTrap Q HP column (50-1000mM KCl or KAc gradient), followed by size exclusion. TubZ-1-442 and TubZ-1-460 were dialyzed as above to remove EDTA from their buffers.

TubZ-Bt Polymerization and Sedimentation Assays

90-degree light scattering experiments were measured using stopped-flow system designed in-house. An excitation wavelength of 530 nm was used. Polymerization was initiated by mixing 2X TubZ protein with 2X nucleotide, or buffer. The final concentration was 3 μ M TubZ, 0.5 mM nucleotide. All proteins, with the exception of D269A-TubZ-pET28a were dialyzed overnight into HMK100 buffer prior to polymerization. Due to its tendency to aggregate in polymerization buffer, reagents were added to D269A-TubZ-pET28a prior to polymerization to match HMK100 buffer.

For sedimentation assays, 6 μ M WT-TubZ-pET28a, WT-TubZ-pET151 or untagged WT-TubZ was assembled with 1 mM GTP or GTP γ S in HMK100 buffer for 10 minutes at room temperature in a 100 μ l volume. The reactions were then centrifuged in a Beckman TLA100 rotor at 55000 rpm for 30 minutes. Pellets were resuspended in loading buffer, and both pellet and supernatant were analyzed on 4-12% SDS-Page with SimplyBlue™ Safe Stain (Invitrogen).

Electron Microscopy

Initial morphology analysis was done using negative stain EM. About 5 μ l sample protein (2-8 μ M) was pre-incubated at room temperature with nucleotide and applied to a glow-discharged carbon coated grid. The exception to this is samples that were incubated on the grid to stabilize two-stranded filaments. In this case, about 4.5 μ l sample protein was applied to the grid, and 0.5 μ l GTP was added, and allowed to incubate for 10-30 seconds

before washing and staining. Samples were negatively stained with 0.75% uranyl formate, and imaged on Tecnai T12 Spirit (FEI Co.) operating at 120 kV.

Cryo-electron microscopy samples were prepared on glow-discharged C-FLAT holey carbon grids that were plunge-frozen in liquid ethane using a Vitrobot (FEI Co.). For the four-stranded reconstruction, wild-type untagged TubZ \sim 8-12 μ M was incubated in the presence of saturating GTP for 4-6 minutes at room temperature before sample application and plunge-freezing. For the two-stranded reconstruction, WT-TubZ-pET151 \sim 8-10 μ M was preheated at 37 degrees, and polymerization was initiated with saturating GTP γ S, and incubated for 30 seconds at room temperature before sample application and plunge-freezing. Cryo-EM data were obtained on a Tecnai F20 operating at 200 kV with an 8k x 8k TemCam-F816 camera (TVIPS, GmbH) with a pixel size of 0.94 Å/pixel for the four-stranded reconstruction, and 1.203 Å/pixel for the two-stranded reconstruction.

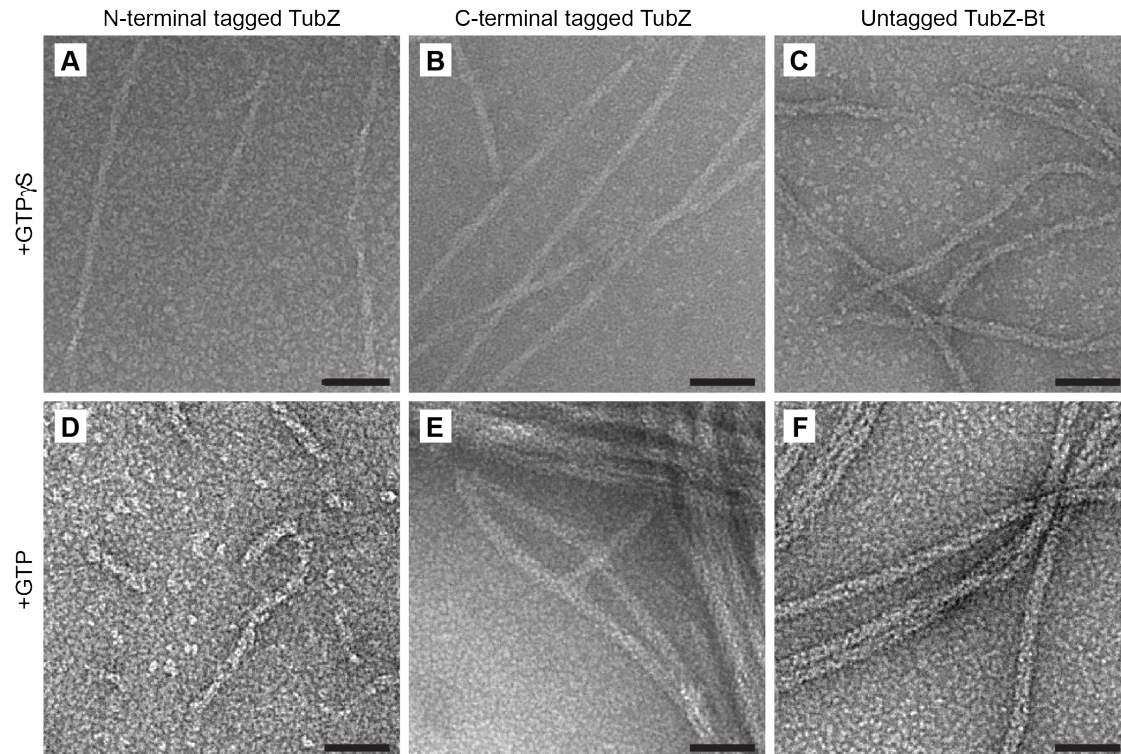
Data processing and Helical Reconstruction for four-stranded reconstruction

In total 414 images were collected. The defocus and astigmatism parameters of the images were determined using CTFFIND3(1), and each micrograph was CTF-multiplied using SPIDER(2), and additionally micrographs were separately corrected using a Weiner filter with in-house software. Particles were boxed out in \sim 481 Å segments, overlapping by \sim 395 Å. Particles were re-centered with respect to the helix axis by integer pixel shifts after several initial rounds of reconstruction. Iterative helical real space refinement was performed via the method outlined in Egelman (3), although modified to use the gold standard method (4). Particle alignment was done with particles boxed from CTF-

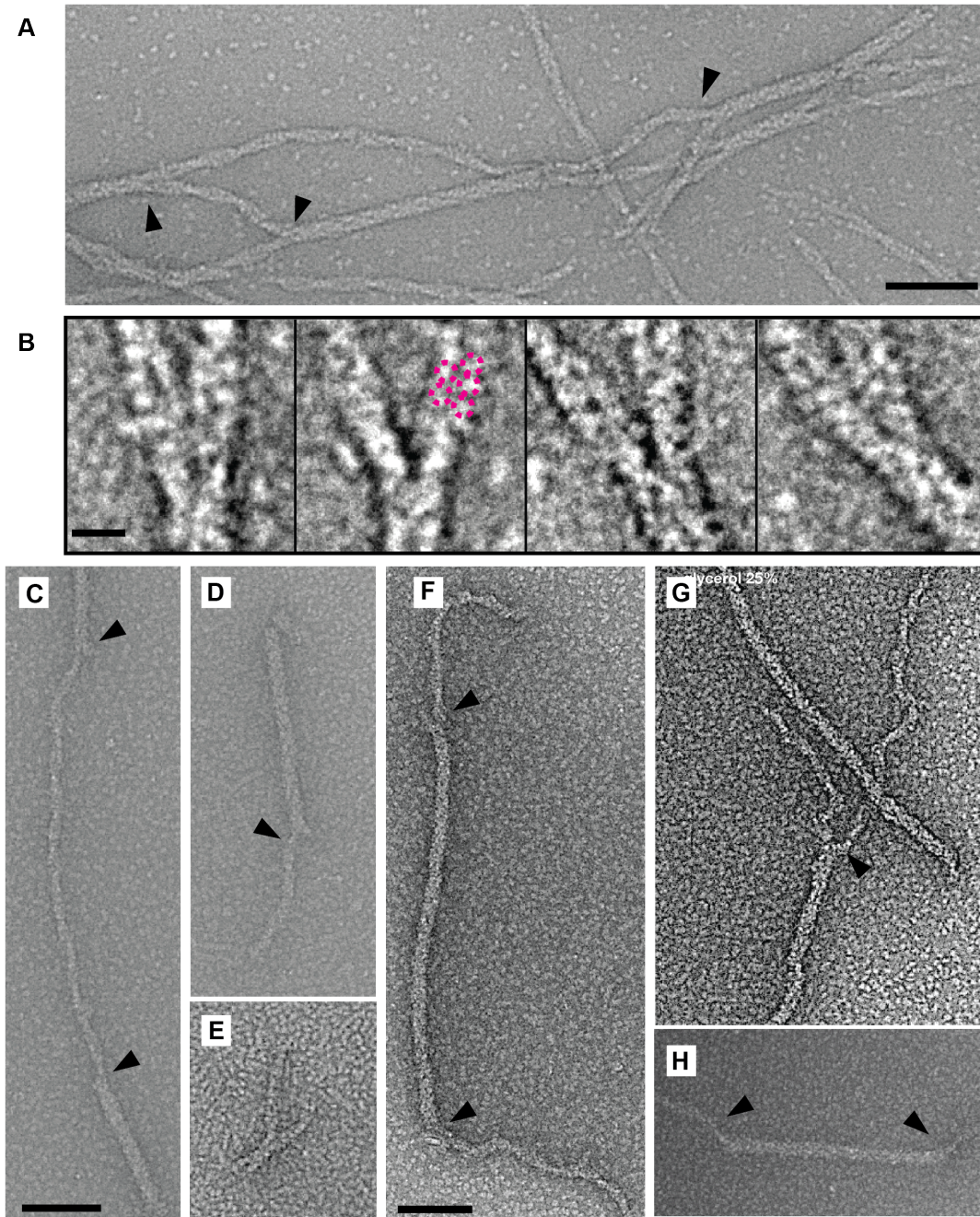
multiplied images, and back-projections were performed using fully CTF corrected particles. Particles that were obviously misaligned based on angle, shifts, or polarity were determined at each round, and not used for the back-projection. (27415/38186) particles were used in the final reconstruction. A low-pass filtered cylinder was used as the initial model. After each round of reconstruction, the volume was both low-pass and high-pass filtered and then used as the reference model for the next round. After several initial rounds were done at 4x bin, particles were re-centered with respect to the helix axis by integer pixel shifts and masked with a cosine-edge mask. Several more rounds of reconstruction were done, and then 2X bin particles were used. The mask and particle size was decreased twice, and then final rounds of refinement of the structure were performed on unbinned particles, only allowing a search of 5 degrees around previously determined alignment parameters. The final box size was ~ 241 Å. The helical symmetry was allowed to refine throughout this process.

Data processing and Helical Reconstruction for two-stranded reconstruction

In total 348 images were collected, and CTF determination and correction and reconstruction were performed essentially as above. The particles were boxed out in ~ 582 Å segments, overlapping by ~ 532 Å. The final box size was ~ 241 Å. (11896/17828) particles were used in the final reconstruction. Most particles that were discarded were because of an inability to align with the correct polarity.

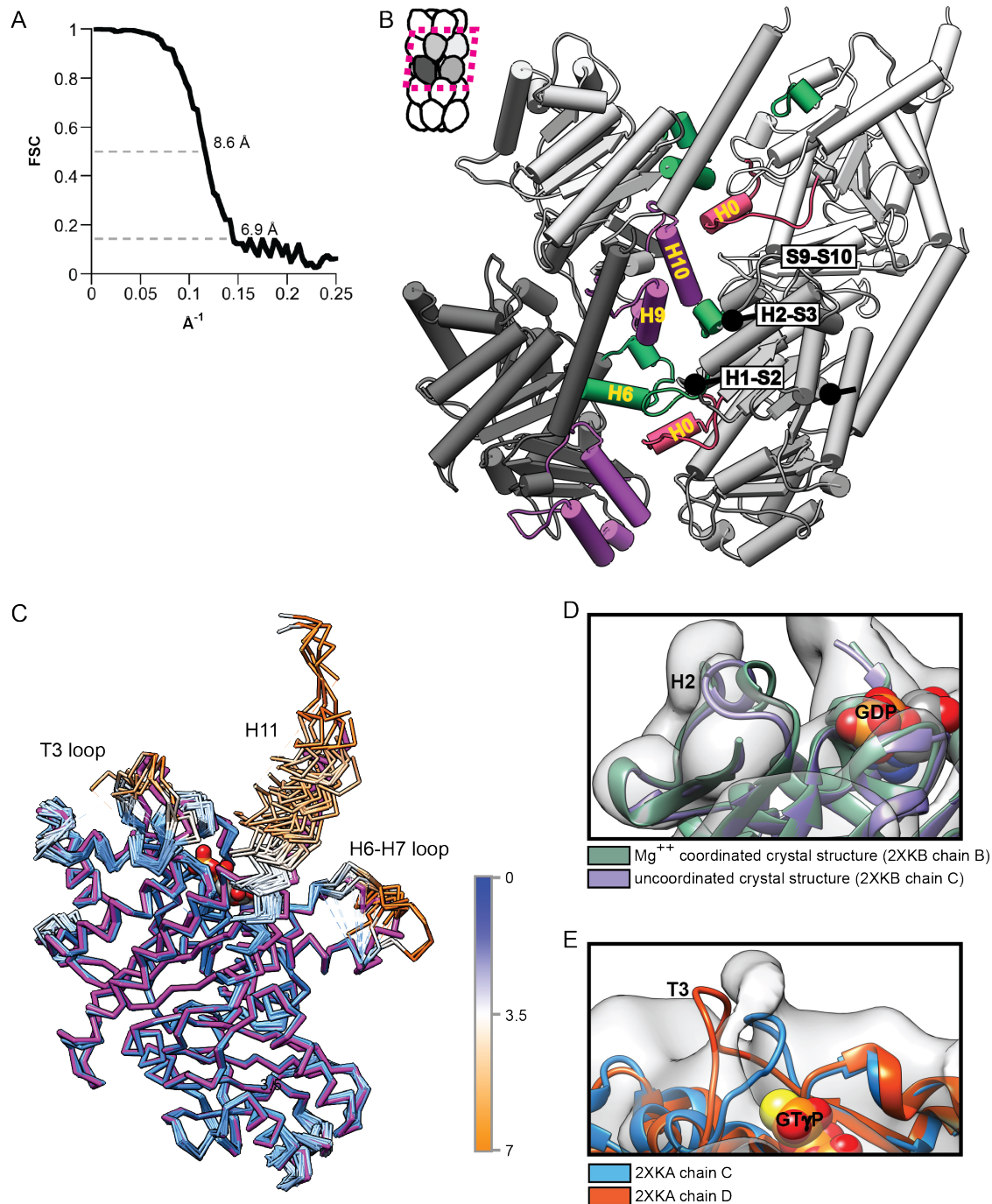


Supplemental Figure 1. Morphology of tagged and untagged TubZ-Bt. Electron micrographs of negative stain EM of N-terminally tagged TubZ in the presence of GTP γ S (A) or GTP (D), C-terminally tagged TubZ in the presence of GTP γ S (B) or GTP (E), or untagged TubZ in the presence of GTP γ S (C) or GTP (F). Scale bar is 500 Å.



Supplemental Figure 2. Examples of the ability of TubZ to convert between filament morphologies. (A) Electron micrograph of negative stain EM of untagged TubZ assembled in the presence of GTP γ S. Scale bar is 500 Å. (B) Boxed particles of the same condition displaying examples of forked transitions from four- to two-strands. Pink circles are

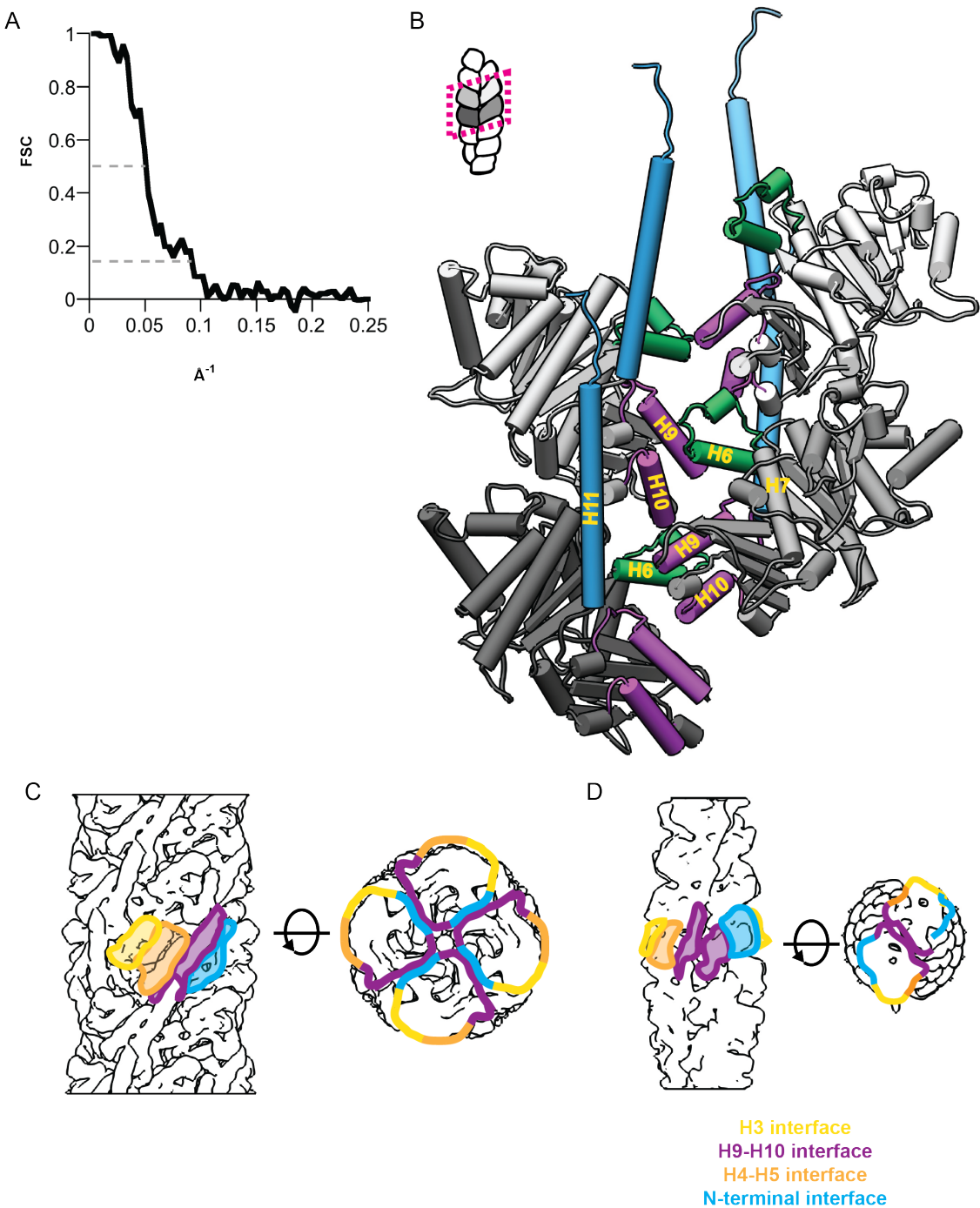
highlights visible puncta that indicate that the two-stranded filaments emerging from forks have the same morphology as free two-stranded filaments. Scale bar is 100 Å. (C)-(E) Electron micrographs of negative stain EM of untagged TubZ assembled in the presence of GTP, grown on the grid for either 10 seconds (C), 20 seconds (D), or 30 seconds (E). (F)-(H) Electron micrographs of negative stain EM of untagged TubZ assembled in the presence of GTP, grown in the presence of 25% glycerol. Scale bar is 500 Å. Black arrows indicate transition points.



Supplemental Figure 3. Analysis of the four-stranded filament reconstruction. (A) FSC curve plotting resolution of the four-stranded filament. Resolution is 8.6 Å at 0.5 cutoff and 6.9 Å at 0.143 cutoff. (B) Highlight of potential interaction interfaces revealed by the pseudoatomic model, using Flex-EM model. (C) Flex-EM model (magenta) overlaid with

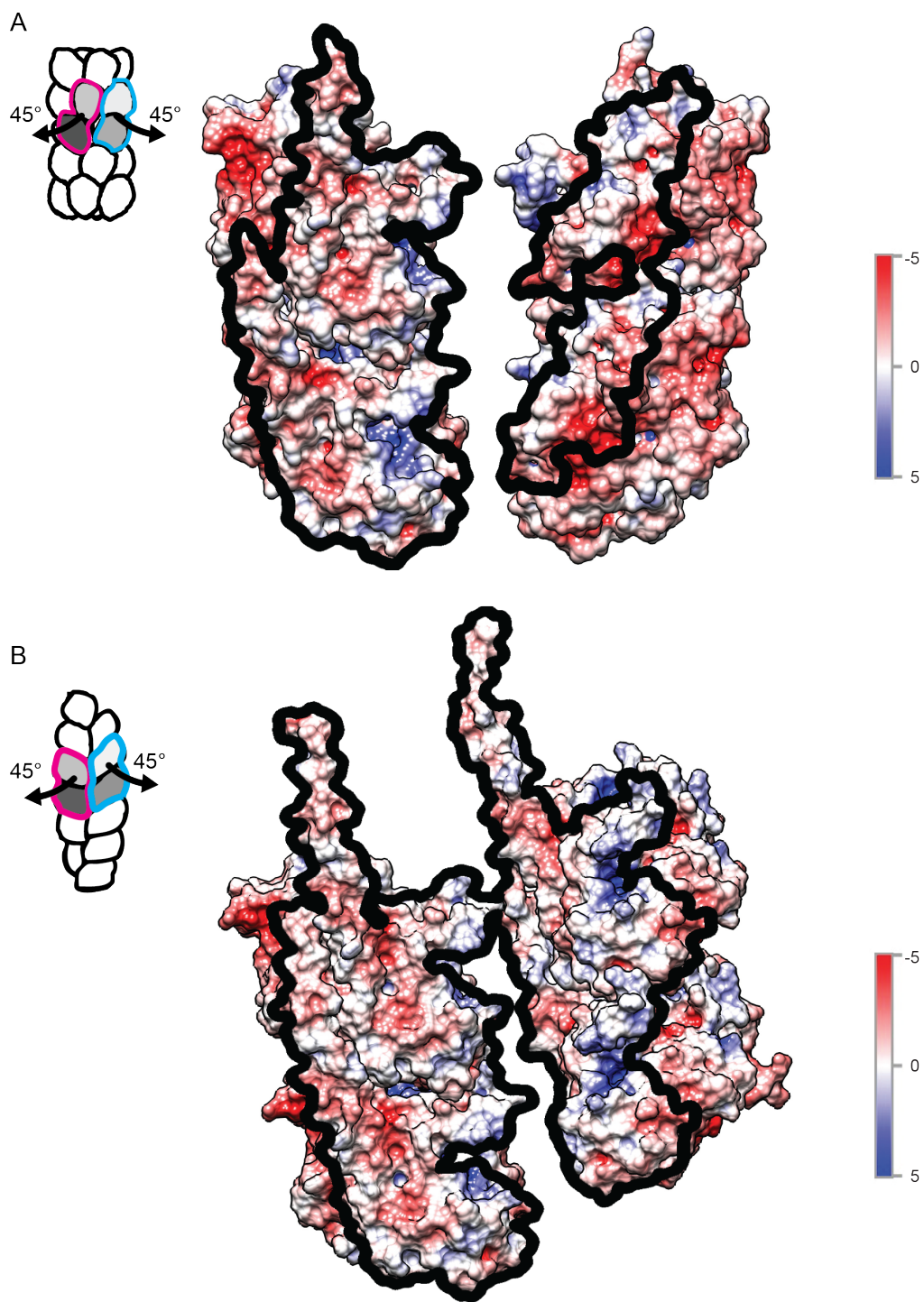
all published chains of TubZ (3M89, 3M8K, 2XKA[A:F], and 2XKB[A:L]). All structures are aligned with chain A of PDB 2XKA. Crystal structures are colored by RMSD from chain A.

(D) Close-up of GTP binding pocket. Fitting of a structure (2XKB:B) in which H2 is coordinated with Mg⁺⁺ (green) in an 'in' position, and of a structure (2XKB:C) in which H2 is uncoordinated with Mg⁺⁺ (purple), in an 'out' position, demonstrating that density corresponds with an uncoordinated 'out' H2. (E) Close up of T3 loop. Fitting of the two T3 loop conformations seen in crystal structures 2XKA:C (blue) and 2XKA:D (orange).

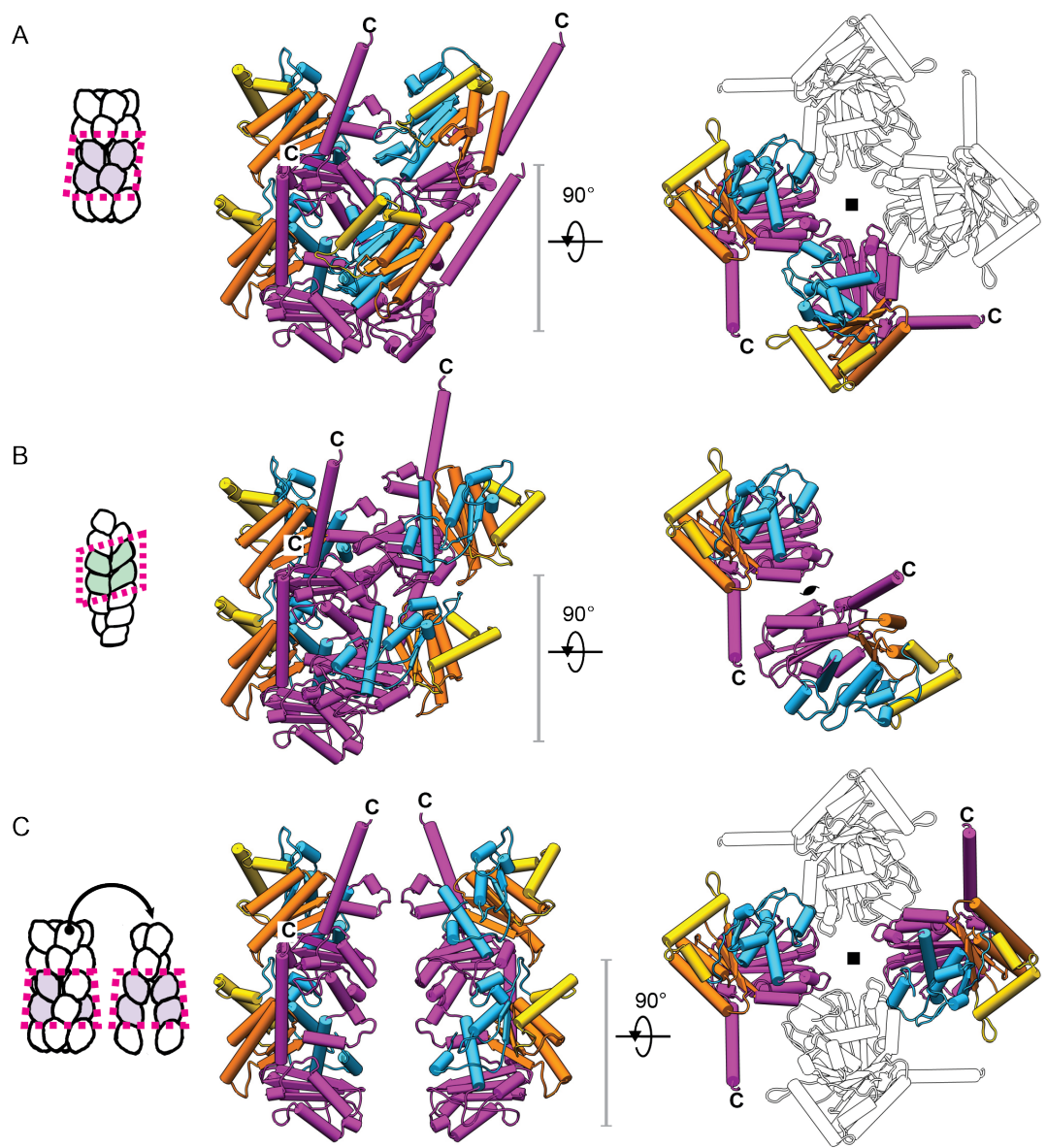


Supplemental Figure 4. Analysis of the two-stranded filament reconstruction. (A) FSC curve plotting resolution of the four-stranded filament. Resolution is 8.8 Å at 0.5 cutoff and 6.6 Å at 0.143 cutoff. (B) Highlight of potential interaction interfaces revealed by the pseudatomic model. (C) Electrostatic surfaces, highlighting the charge of interface in the

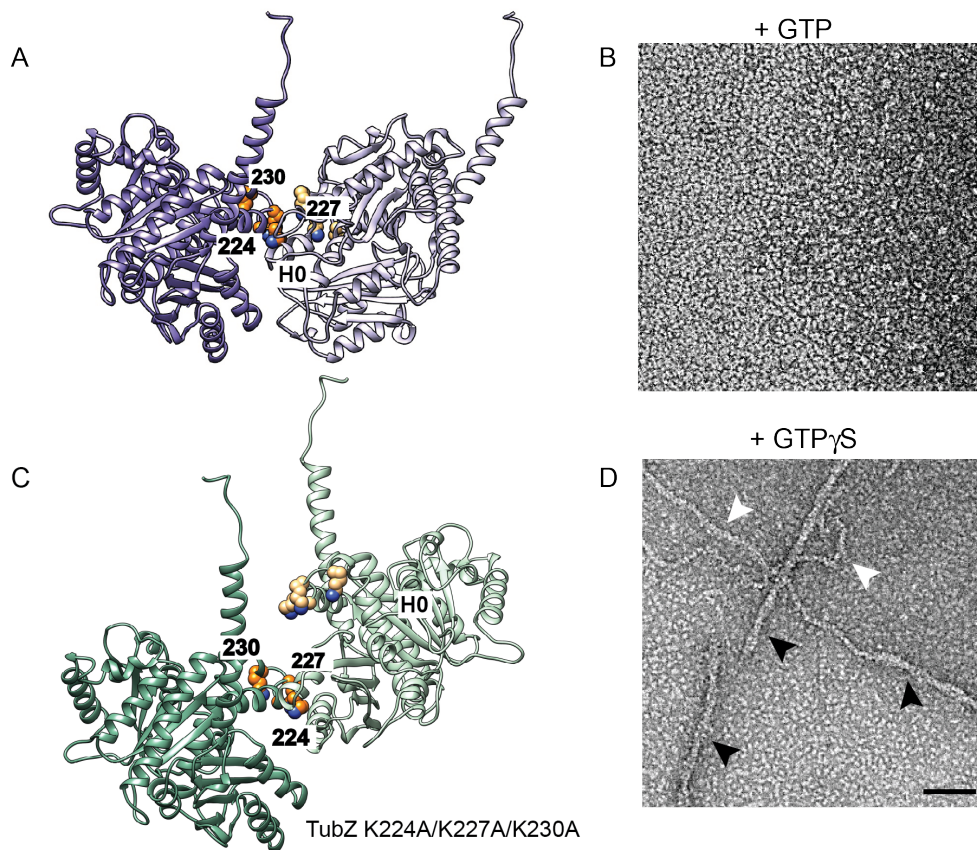
cross-strand interactions of the two-stranded filament. Highlighted are H6-H7 loop (*), H9/H10 (+), and H11 (◇). Structure used for representation in (B) is PDB 2XKA chain F with the residues of the H6-H7 loop built in with the same conformation as the Flex-EM model. (D) and (E) Diagrams of different interfaces observed in the two reconstructions, residues 0-80 and 236-257 are colored in blue, 81-129 in gold, residues 130-212 in orange, and 213-235 and 258-414 in magenta.



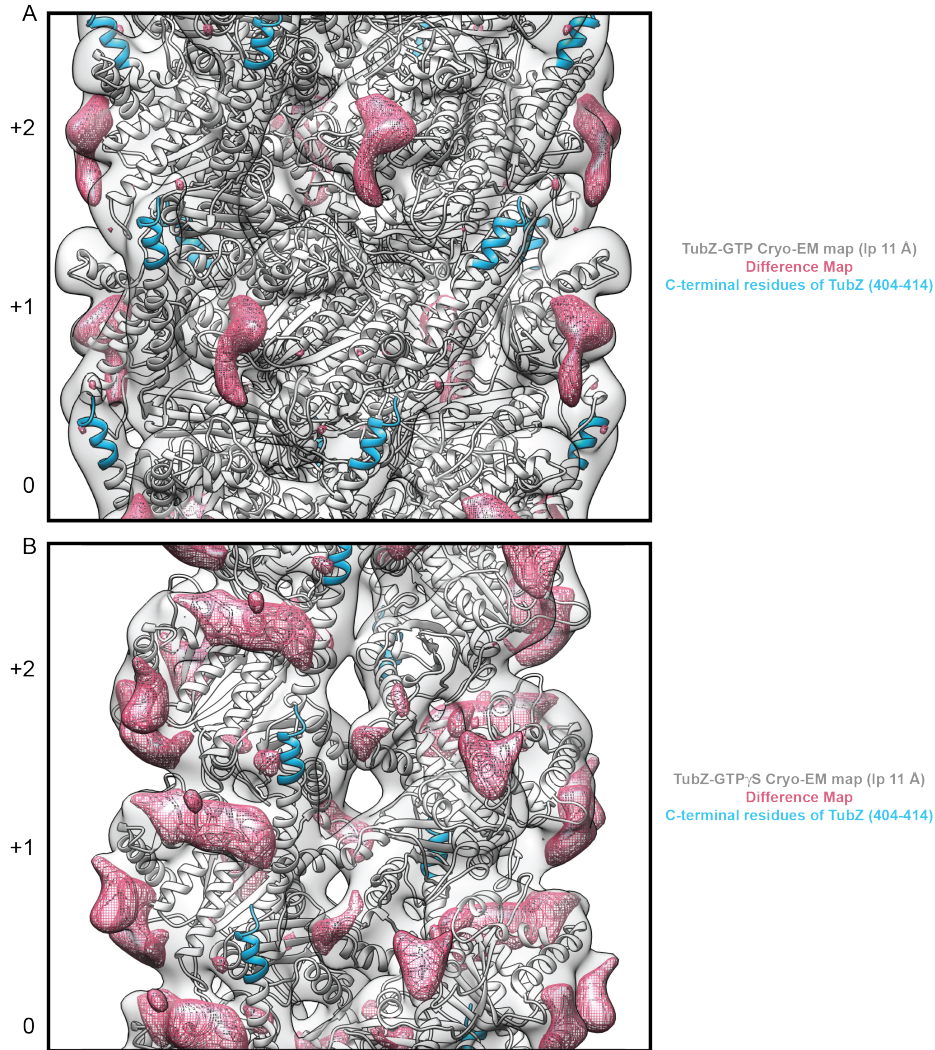
Supplemental Figure 5. Comparison of the interactions of the two and four-stranded interfaces. (A) and (B) four-stranded and two-stranded electrostatic interfaces, respectively, broken apart with each strand rotated outward 45 degrees.



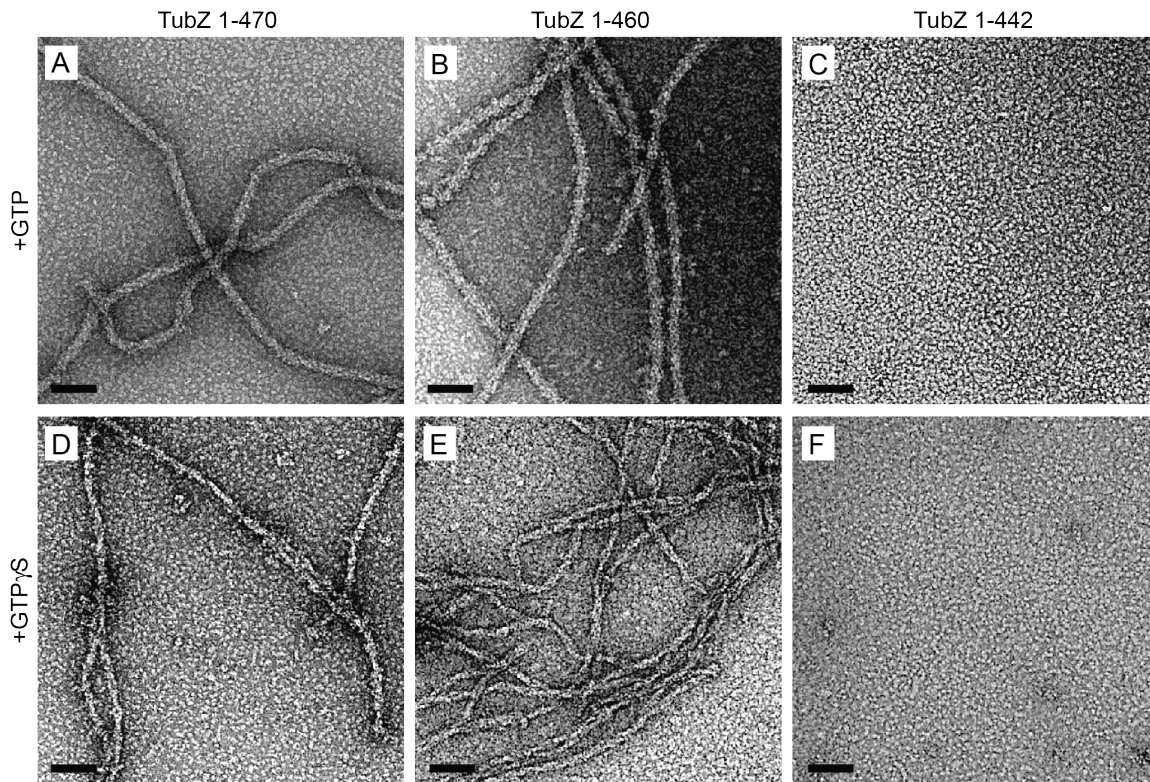
Supplemental Figure 6. Comparison of the lateral interactions of the two- and four-stranded protofilaments. (A) Interaction of adjacent protofilaments in the four-stranded structure. (B) Interaction of two-stranded filament. (C) Interaction of opposite protofilaments of the four-stranded structure/ Structure used for representation for all is the Flex-EM model.



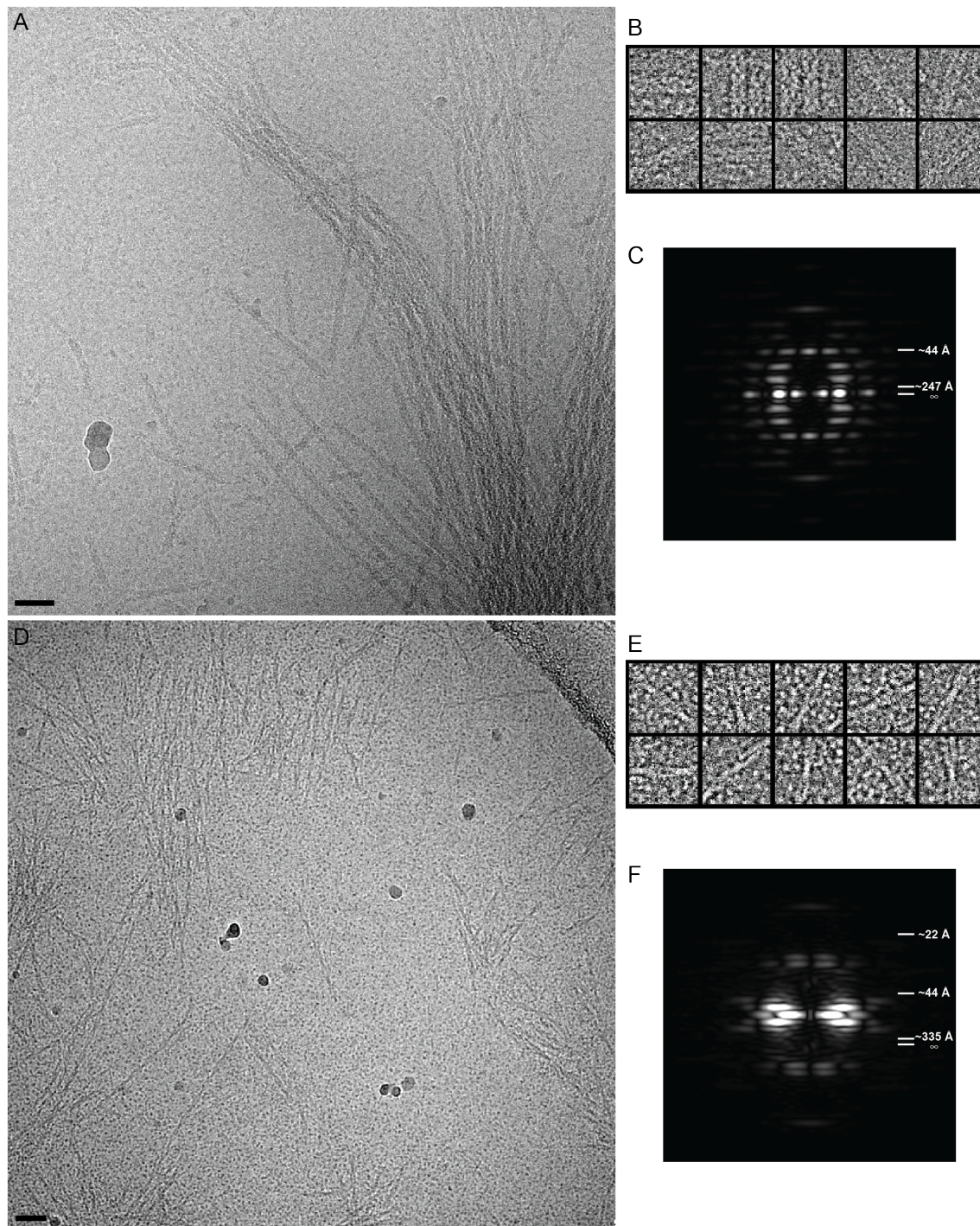
Supplemental Figure 7. Mutants to lateral four-stranded interface mainly affect four-stranded filament formation. (A) Location of K224, K227 and K230 in the four-stranded interface, highlighted in orange spheres. (B) Electron micrograph of negative stain EM of K224AK227AK230A TubZ triple mutant in the presence of GTP, showing no assembly of TubZ filaments. (C) Location of K224, K227 and K230 in the two-stranded interface, highlighted in orange spheres. Structure used for representation in (A) and (C) is PDB 2XKA chain F with the residues of the H6-H7 loop built in with the same conformation as the Flex-EM model. (D) Electron micrograph of negative stain EM of K224AK227AK230A TubZ triple mutant in the presence of GTP γ S, showing assembly of two-stranded TubZ filaments (black arrows), and some single protofilaments (white arrows).



Supplemental Figure 8. Difference maps of four- and two-stranded filament reconstructions highlighting location of C-terminal tail density. (A) Difference map between four-stranded reconstruction and pseudo-atomic map, both filtered at 11 Å. Density differences indicated in pink, and end of C-terminal tail (residues 404-414) indicated in blue. (A) Difference map between two-stranded reconstruction and pseudo-atomic map, both filtered at 11 Å. Density differences indicated in pink, and end of C-terminal tail (residues 404-421) indicated in blue. Pseudo-atomic models were made using the Flex-EM model.



Supplemental Figure 9. Truncations of the C-terminal tail do not affect filament morphology. Electron micrographs of negative stain EM of TubZ 1-470 in the presence of GTP γ S (A) or GTP (D), TubZ 1-460 in the presence of GTP γ S (B) or GTP (E), or TubZ 1-442 in the presence of GTP γ S (C) or GTP (F). Scale bar is 500 Å.



Supplementary Figure 2. Analysis of cryo-EM data collection. (A) Uncorrected cryo-EM micrograph of TubZ:GDP filaments, defocus = $-1.9 \mu\text{m}$, binned 8x, scale bar = 50 nm. (B) Gallery of particles used in TubZ:GDP reconstruction, box size = $\sim 481 \text{ \AA}$. (C) Power Spectra of ~ 6700 averaged particles of TubZ:GDP. (D) Uncorrected cryo-EM micrograph of ~ 6700 averaged particles of TubZ:GDP. (E) Gallery of particles used in TubZ:GDP reconstruction. (F) Power Spectra of ~ 6700 averaged particles of TubZ:GDP.

TubZ:GTP γ S filaments, defocus = -3.4 μ m, binned 8x, scale bar = 50 nm. (B) Gallery of particles used in TubZ:GTP γ S reconstruction, box size = \sim 558 Å. (C) Power Spectra of \sim 6700 averaged particles of TubZ:GTP γ S

Supplementary References:

1. Mindell JA & Grigorieff N (2003) Accurate determination of local defocus and specimen tilt in electron microscopy. *J Struct Biol* 142(3):334-347 .
2. Frank J (1996) *Three-dimensional Electron Microscopy of Macromolecules* (Academic Press, San Diego).
3. Egelman EH (2007) The iterative helical real space reconstruction method: surmounting the problems posed by real polymers. *J Struct Biol* 157(1):83-94 .
4. Scheres SH & Chen S (2012) Prevention of overfitting in cryo-EM structure determination. *Nat Methods* 9(9):853-854 .

Chapter Five

Complementary experiments towards understanding TubZ-Bt filament formation

Introduction

The previous chapter explored the formation of TubZ-Bt filaments, and the structures of the two main morphological states of TubZ-Bt by high-resolution cryo-EM. We have proposed a model in which a two-stranded TubZ-Bt filament is a transitory pre-hydrolysis state, and is on pathway to a four-stranded post-hydrolysis state. This chapter will cover work that is complementary to the work of chapter four, including experiments that are either in preliminary stages or did not fit neatly into the story which chapter four presented.

Results and Discussion

TubZ-Bt:GTP γ S forms 2, 3, and 4 stranded filaments

In chapter four, we were able to see that in the presence of GTP γ S, TubZ-Bt forms two-stranded filaments, were as in the presence of GTP, TubZ-Bt forms four-stranded filaments. It was noted however, that although TubZ-Bt:GTP γ S was mainly two-stranded filaments, a population of thick filament was also seen. In order to compare what we believed were four-stranded TubZ-Bt:GTP γ S with TubZ-Bt:GDP four-stranded filaments, we boxed out overlapping segments of thick filaments and used these particles to perform reference free class-averaging. Surprisingly, two distinct averages arise from this classification of thick filament particles. The smaller of the two classes appears to be nearly identical to averages of four-stranded TubZ-Bt (Figure 1d). The other larger class appears to have an intensity pattern that is reminiscent of that seen for PhuZ-201 filaments, which have been determined to be three-stranded (Elena Zehr, et al, submitted) (Figure 1e). In order to determine the nature of these filaments, we did a cursory IHRSR reconstruction

using only ~1100 particles. Interestingly, this revealed that it was indeed a three-stranded filament. Both half-subunit and full-subunit rises were used as initial guesses, and this revealed that these three-stranded filaments are planar similar to the four-stranded filament, with a very tight twist of 22 degrees, smaller than that of both the two-stranded and four-stranded filaments. It is unclear whether this three-stranded filament is yet another intermediate stage before the formation of the four-stranded filament or if this is just an artifact of spurious filaments stabilized by the GTP analog.

Effects of additional nucleotide analogs on TubZ-Bt filament formation

In previous experiments in chapter four of TubZ filaments were formed in the presence of GTP γ S or with a non-hydrolyzing mutant, D269A. Because with $\alpha\beta$ -tubulin and PhuZ-201, different non-hydrolyzable GTP analogs have different effects on polymerization, we wished to test the effects of two other GTP analogs, GMPCPP and GMPPNP, on TubZ-Bt filament formation. By negative stain EM, we see that TubZ-Bt filaments formed with both GMPCPP and GMPPNP (Figure 2). By eye, it appears that GMPPNP is worse at forming filaments than GTP γ S or GMPCPP, but quantitative assays would have to be performed in order to more clearly understand the effect.

Modeling TubZ-Bt filament nucleation

We wished to understand if there was a difference in nucleus size and steps to formation of a nucleus between filaments formed in the presence of GTP or GTP γ S. If the two-stranded filament were indeed on-pathway to formation of the four-stranded filament, we would predict that they should form a similar nucleus. We used two different methods

to analyze the data. The first method is well known for its use on actin homolog modeling, developed by Oosawa (1-3). It assumes that nucleation is a one-step process and that depolymerization is negligible. The other method has been used for determining nucleus size was developed by Flyvbjerg which allows for determination of the number of steps involved in nucleus formation, and also the number of monomers added at each addition (4). The results from analysis using these methods are shown in table 1. We see for the Oosawa method, that we get a different nucleus size for GTP (4 monomers) versus GTP γ S (5 monomers) filaments. However, using Flyvbjerg's methods, we find that for both, the number of steps is 2, and the monomers added per step are 3 (Figure 3). Because the Oosawa method assumes a two-step process, and we determined by the Flyvbjerg method that it was a two-step process, it would be expected that the nucleus size should be identical, if the assumption made in these models are indeed correct. Unfortunately we do not see agreement between these two models. This is probably the result of a more complicated nucleation process than these two methods model, and more careful analysis of TubZ-Bt polymerization kinetics is needed.

Preliminary attempts towards an orthogonal mutation disrupting four-stranded filaments

We previously tested the effect of a small number of residues N-terminal to TubZ, as well as the mutation of 3 lysines in the H6-H7 loop to alanine, and we determined that these mutations are able to block 4-stranded filament formation. The N-terminal residues provide an effect that is on an orthogonal surface to the interacting surfaces on two-stranded filament, however it is unclear what precisely causes the blockage of the four-stranded filament formation. On the other hand, the 3KA mutation is contained in both the

two-stranded and four-stranded interfaces, and we see that it does in fact have some effect on two-stranded filament formation. We wished to design orthogonal mutations to block four-stranded and potentially also the two-stranded filament formation. We designed and cloned several single mutations guided by the pseudo-atomic models determined by fitting into the cryo-EM reconstructions (Figure 4a). We purified several of these mutants and determined their ability to polymerize in the presence of both GTP and GTP γ S by pelleting assay. We see that the two orthogonal mutations, E9A and D366A have little to no effect on TubZ-Bt polymerization in either nucleotide. Two of the non-orthogonal mutants, K224A and R218A have a limited effect, mainly on polymerization in the presence of GTP. Another non-orthogonal mutant, R342W, which inserts a bulky residue into the four-stranded interface, has a more dramatic effect, almost eliminated polymerization in the presence of GTP, and decreasing polymerization in the presence of GTP γ S (Figure 4b). We also see by negative stain that all of these tested mutations appear to have no effect on the morphology of these filaments (Figure 5). It is unfortunate that none of the orthogonal mutations have thus far been able to break the four-stranded interface in a clear way. The four-stranded interface contains a number of charged residues, and it appears likely to break the surface in a way orthogonal to the two-stranded surfaces that multiple mutations will have to be made. Pending mutations, some of which have been cloned and others that have not are outlined in table 2.

Effects of pH on TubZ-Bt filament formation

Because both two- and four-stranded surfaces are both highly charged with both positive and negative residues, we were curious what the effect of changing the pH of the

buffer used for polymerization. Using negative stain EM, we looked at filament formation at pH 6, 7.7, and 9. In the presence of GTP at pH 6, TubZ-Bt filaments look less organized than at pH 7.7 and 9, but otherwise, this pH range has no dramatic effect on filament morphology (Figure 6). A more quantitative analysis is needed to determine whether there is an overall effect on polymerization amount.

TubZ-Bt filaments with four-stranded interface blockage release GDP rapidly

Previous results (5) had shown that the GDP release rate of TubZ-Bt is quite high for tubulins, at 16-18 GDPs per TubZ per minute. However, the TubZ-Bt construct used in these studies contains additional residues on the N-terminus, which we had determined affect the ability of TubZ-Bt to properly assemble. We wished to determine whether the more stable four-stranded filaments formed by the untagged construct would have a different release rate. We would expect if indeed the two-stranded filament is on pathway to the four-stranded filament that untagged TubZ-Bt would form stable filaments that have a much slower GDP release rate, but if we tested the N-terminal tagged TubZ that we would recapitulate a similar release rate seen before (Figure 7a). To monitor the GDP release rate, we used the established coupled GTPase assay established by Ingerman and Nunnari (6), diagramed in Figure 7c. When we perform this assay on both untagged and N-terminally tagged protein we see that they do in fact have quite different GDP release rates (Figure 7b). The untagged protein has a much slower GDP release rate of ~ 2 GTP/TubZ.min, whereas the N-terminally tagged protein has a similar rate to that previously published (5), of ~ 11 GTP/TubZ.min. These results agree well with our hypothesis that the two-stranded filaments are unstable and if four-stranded filament formation is blocked that they fall

apart, thus releasing GDP. The more stable four-stranded filament retains GDP within the filament so that GDP release is slower. In addition to these studies, and important next step would be to do a phosphate release rate assay, to show that the release rate is not dependent on hydrolysis. We would expect, given our hypothesis, that the phosphate release of both the untagged and N-terminally tagged TubZ-Bt filaments should be the same.

Preliminary efforts to identify location of C-terminal tail by GFP tagging

In chapter four, we discussed how in all the extant crystal structures of TubZ-Bt, that the extended C-terminal has been cleaved (7, 8). We observed that although the constructs we used in our high-resolution cryo-EM studies were both full length TubZ-Bt we did not see density in either structure for the majority of the C-terminal tail. We wished to see if we could further locate the C-terminal tail by tagging TubZ-Bt with cyan fluorescent protein, a homolog of GFP. Using negative stain EM, we collected data of filaments formed by TubZ-Bt-CFP in the presence of either GTP or GTP γ S. Both four-stranded and two-stranded filaments formed similarly to wild-type protein, however filaments had a noticeably 'fuzzy' appearance (Figure 8c,d and 9c,d.) We performed IHRSR on both GTP and GTP γ S data sets, using low-passed reconstructions of the respective wild-type negative stain reconstructions as starting models. Likewise, the refined helical parameters were used as starting guesses for the respective reconstructions. At a higher contour level, both TubZ-Bt-CFP:GTP and TubZ-Bt-CFP:GTP γ S reconstructions look nearly identical to their wild-type counterparts (Figure 8b and Figure 9b). However, when we lower the contour on both reconstructions we begin to see extra density appearing that

could potentially be attributed to the CFP. This extra density is rather weak, indicating that location of the CFP is probably somewhat heterogeneous along the helix. This corresponds with the lack of density that we see in the cryo-EM reconstructions, which indicate the last 60 residues of TubZ are mostly unstructured and are rather floppy. Mutational investigation of the C-terminal tail will be valuable for further understanding what role the C-terminus plays in TubZ-Bt filament formation.

Preliminary efforts towards in vivo tomography of TubZ-Bt

Because previous efforts to understand the morphology of TubZ-Bt filaments *in vivo* in *E. coli* had been interpreted as revealing that TubZ-Bt *in vivo* was two- rather than four-stranded (7), we wished to follow up using a more native organism. Unfortunately, *B. thuringiensis* is a rather large bacterium, unsuitable for this type of tomographic investigation. We were kindly provided with a strain of *B. subtilis* with a genetic modification that constrained its size to be more amenable to tomography by the lab of Dr. Kay Pogliano at UCSD. Dr. Marcella Erb, graduate student of Dr. Joe Pogliano at UCSD transformed these mutant strains with xylose inducible TubZ-Bt and TubZ-Bt-GFP. We attempted tomography of these bacteria several times, but samples picked remained quite thick so that it was unclear whether or not TubZ-Bt was expressed or not (Figure 10a). To follow up, we tested induction by observing induced TubZ-Bt-GFP by fluorescence microscopy, and we are able to clearly see that TubZ-Bt-GFP is clearly overexpressed in the mini *B. subtilis* (Figure 10b). These tomography studies are an important follow-up to the work of the previous chapter. Learning the morphological state of TubZ-Bt filaments is crucial to understanding how TubZRC-Bt performs its function as a plasmid segregation

machine. Tests to determine how to get the thinnest bacteria, or segmentation of *B. thuringiensis* containing native pBtoxis plasmid are necessary for this. Once TubZ-Bt can be clearly seen, tomographic reconstructions such as those done on the BtubA/B filament (9) can be performed to determine the morphological state of TubZ-Bt *in vivo*. Especially important is determining this also in the presence and absence of the TubRC complex.

Preliminary efforts towards observing TubZ-Bt dynamics by TIRF

In order to understand how the TubZRC system works to segregate plasmids, it is important to understand the dynamics of TubZ-Bt filaments in the presence and absence of TubRC complex. In order to do that, we have made constructs with both an N-terminal KCK tag, as well as a C-terminal KCK tag. We can label N-terminal KCK-TubZ-Bt with a maleimide reactive fluorescent dye, such as Alexa Fluor 488. With 10% of labeled protein, we can clearly see TubZ filaments in TIRF (Figure 11). Future experiments should be done using the C-terminally tagged version of this protein, to avoid the effects of the N-terminus on polymerization. With this system we should be able to tease apart the dynamics of TubZ-Bt in the presence and absence of TubRC complex.

Purification and preliminary observation of TubZ from B. megaterium plasmid pBM400

In order to understand the relevance of the morphological change of TubZ from *B. thuringiensis*, we wished to understand how generalizable these nucleotide driven changes were. Previous research has characterized other TubZs (from *B anthracis* and Clostridial phage C-st) as two-stranded helices (5, 10). However, TubZ-Ba was purified with remaining N-terminal residues, so it is possible that this protein was mischaracterized, as was TubZ-

Bt in the same paper. TubZ-Cst is missing the N-terminal helix H0, which lies in the four-fold interface, so we believe that this could lead it to having a unique morphology from other TubZs. We obtained cDNA for TubZ from the *B. megaterium* plasmid pBM400 to further investigate the morphology of the filaments of this new TubZ. We were unable to purify an N-terminally his-tagged protein because of solubility issues, but we were able to purify a small quantity of N-terminally GST-tagged protein through affinity chromatography and SEC (Figure 12). Unfortunately we can see that this protein is still quite contaminated GroEL chaperone (Figure 13). We investigated this protein by negative stain EM in the presence of GTP γ S. The filaments in the images collected are not ideal, but we were able to do rough average of the filaments using the EMAN1.9 program startnrclasses (11). Surprisingly, we see a pattern very similar to that see for PhuZ-201 and the small class of TubZ-Bt three-stranded filaments, suggesting that this as well may be a three-stranded filament. It is important to follow up on this work, both by improving the purification, making untagged constructs of TubZ-Bm and then by further characterizing the nature of these filaments in the presence of both GTP and non-hydrolyzing nucleotide analogs. TubZ-Bm is an especially interesting target for further study because of the recent work on TubR-Bm done by Aylett et al (12), which may be a simple route towards understanding the interaction between TubZs and TubRC complexes, and therefore provides insight into the workings of TubZRC molecular machines.

Methods

Purification of TubZ-Bt mutants

TubZ-Bt-E9A, R218A, K224A, K224A/K227A/K230A, R342W, and D366A proteins were purified in a similar manner to wild-type untagged TubZ (outlined in chapter 4 supplementary methods). The first ammonium sulfate cut was performed at 20% for 3K-TubZ, but 25% for all others. After the second cut, the pellet was resuspended and either desalted (3K-TubZ), or dialyzed overnight (all others). The resuspension was then run on a HiTrap Q HP column (50-1000mM KCl or KAc gradient), followed by size exclusion. Proteins were dialyzed into HMK100 buffer (100 mM KAc, 5 mM MgAc₂, 50 mM HEPES pH 7.7) to remove EDTA from their buffers.

Residues KKCK were mutated into the N-terminus of TubZ-pET151b after the TEV cleavage site, replacing residues that were already remaining after TEV cleavage. KKCK-TubZ-Bt in pET151 was overexpressed and purified in an identical manner to TubZ-Bt-pET151 (described in chapter 4), with the exception that the final buffer included 200 μ M TCEP replacing 10 μ M 1-thioglycerol.

Negative Stain Electron Microscopy

About 5 μ l TubZ-Bt protein sample (2-10 μ M) was pre-incubated at room temperature with nucleotide and applied to a glow-discharged carbon coated grid. Most samples were made using HMK100 buffer, with the exception of the pH experiments, where for pH 6, HEPES pH 7.7 was replaced with MES pH 6.0, and for pH 9, was replaced with Tris-HCl pH 9). Samples were negatively stained with 0.75% uranyl formate, and imaged either on a Tecnai T12 Spirit or a Technai T20 (FEI Co.) operating at 120 kV. Reference free class averages were made using the EMAN1.9 package startnrclasses (11). IHRSR was performed using non-CTF-corrected images via the method outlined in Egelman (13). Images for the three-

stranded reconstruction were selected based on the previous class-average results, and only ~1100 particles were used. TubZ-Bm was visualized using a concentration of 16 μM in the presence of 1 mM GTP γ S.

TubZ-Bt Polymerization and Sedimentation Assays

90-degree light scattering experiments were measured using stopped-flow system designed in-house. An excitation wavelength of 530 nm was used. Polymerization was initiated by mixing 2X TubZ protein with 2X nucleotide, or buffer. TubZ-Bt was used in a range of 2-3.8 μM final protein concentrations and 1.4-3.8 final protein concentration for GTP and GTP γ S experiments respectively. 0.5 mM nucleotide was used for all experiments. Each concentration was polymerized and observed at least 3 times, and these runs were averaged. Each set of concentrations was re-run on three separate days. To analyze the data via the 'Oosawa' method, the initial velocity of polymerization was measured by determining the slope of early time points, and plotting it against concentration. To analyze the data via the 'Flyvbjerg' method, data were scaled using an in-house program called 'tubscl', and the collapsed polymerization curve from this data was used to calculate tenth time and the initial velocity of polymerization.

For sedimentation assays, 6 μM of TubZ-Bt-E9A, R218A, K224A, K224A/K227A/K230A, R342W, or D366A, was incubated with 1 mM GTP or GTP γ S in HMK100 buffer for 5 minutes at room temperature in a 100 μl volume. The reactions were then centrifuged in a Beckman TLA100 rotor at 55000 rpm for 30 minutes. Pellets were resuspended in loading

buffer, and both pellet and supernatant were analyzed on 4-12% SDS-Page with SimplyBlue™ Safe Stain (Invitrogen).

Continuous Coupled Regenerative GTPase assay

The continuous coupled regenerative GTPase assay was performed basically as previously described (6). We used an in-house stopped-flow device monitoring absorbance at 340 nm. A final concentration of 3 μ M TubZ-Bt (either untagged or N-terminally tagged) was used. Final concentration of other components were: 100 U/ml pyruvate kinase, 220 μ M NADH, 1 mM GTP, 2 mM PEP, and 100 U/ml lactate dehydrogenase. Because we were concerned about the signal arising from absorbance of filaments formed, we also ran experiments without pyruvate kinase present, and then subtracted the signals from the actual experiment runs.

Overexpression, light microscopy, and tomography of TubZ-Bt in 'mini'-B. subtilis

Pre-transformed glycerol stocks of TubZ-Bt (strain ME84) or TubZ-Bt-GFP (strain ME80) in 'mini'-*B. subtilis* were streaked onto LB-agar plates, and then overnight cultures with 5 μ g/ml tetracycline were made from colonies picked off plates., and grown at 30 degrees Celsius. For light microscopy, 2 mL of overnight culture of TubZ-Bt-GFP strain ME80 were then added to 1 mL fresh LB and induced with varying concentrations of xylose (0.05% - 0.5%) for 1 hour. 1 mL was removed from each tube, and 0.2 μ L FM464 (a fluorescent membrane dye) was added and agitated. This sample was then spun at 4000 x g for 30 seconds. The supernatant was aspirated and the pellet was resuspended in 900 μ L 1X PBS. Samples were then visualized by using epifluorescence.

For tomography samples, 2 mL of overnight culture of TubZ-Bt strain ME84 were then added to 1 mL fresh LB and induced with 0.2% xylose for 1 hour. This sample was then spun at 4000 x g for 30 seconds. The supernatant was aspirated and the pellet was resuspended in 400 μ L 1X PBS supplemented with 0.2% xylose. 2 μ L of sample was then applied to a glow-discharged holey carbon grid, blotted for 2 seconds, and plunge frozen using a Vitrobot (FEI). Samples were imaged on a FEI Technai Polara at 300 kV. A magnification of 34000 was used, with a 6 μ M defocus, tilting from -60 to 60 degrees. Images were processed using the software PRIISM .

TubZ labeling and TIRF microscopy

KKCK-TubZ-pET151 was labeled by first adding 3-fold excess Alexa Fluor 488 C5-maleimide (Molecular Probes) to protein in buffer. Protein and dye were incubated at room temperature for 10 minutes, then stirred at 25 degrees Celsius at 350 rpm for 3 hrs. 6-fold excess of β -mercaptoethanol was then added to quench the crosslinking reaction. Protein was dialyzed overnight in HMK300 (300 mM KAc, 5 mM MgAc₂, 50 mM HEPES pH 7.7) + 1 mM DTT. Sample was then run over G50 illustra NICK column (GE Healthcare Life Sciences) using the same buffer. Percentage labeling of protein was then calculated using absorbance readings at 280 nm and 494 nm.

For TIRF light microscopy, thawed samples of labeled KKCK-TubZ-pET151 and unlabeled TubZ-Bt-pET151 were spun in a bench top centrifuge at top speed for 10 minutes. Supernatant was removed and concentration and percentage labeling were re-measured using absorbance readings. Either 10% or 20% of labeled KKCK- TubZ-pET151 was mixed with unlabeled TubZ-Bt-pET151 in the presence of 1 mM GTP γ S. 50 μ L of

solution was dropped onto a poly-lysine, plasma cleaned coverslip, incubated for 5 minute at room temperature, aspirated and then flipped over onto a slide with a drop of mounting media, and then imaged by TIRF microscopy.

Purification of TubZ-Bm

cDNA for TubZ from the plasmid pBM400 (14) from *B. megaterium* was a gift of the lab of Dr. Joe Pogliano of UCSD. TubZ-Bm was cloned into a p-GEX6p-2 (GE Healthcare Life Sciences), which contains a PreScission protease cut site, and GST-tag on the N-terminus. GST-TubZ-Bm was transformed into BL21 Star™ (DE3) cells, and grown in the presence of antibiotic at 30 degrees Celsius until an OD600 of ~1. Expression was then induced with 1mM IPTG and incubation temperature was shifted to 16 degrees Celsius overnight.

Thawed pelleted cells from 1 L of growth were resuspended in ~50 mL lysis buffer (300 mM KAc, 50 mM HEPES pH 7.7, 5 mM MgAc₂, 1 μM GDP, 10% glycerol, 1 mM DTT, 1 EDTA-free protease tab (SIGMA)), lysed by Emulsiflex for 10 minutes, and then clarified by centrifugation at 35k x g for 40 minutes. Clarified supernatant was then loaded on to 3 mL bed volume of pre-equilibrated GST-sepharose beads, and incubated with nutation for 3 hrs. Lysate was then allowed to flow-through, and beads were washed with 30 mL wash buffer (300 mM KAc, 50 mM HEPES pH 7.7, 5 mM MgAc₂, 10% glycerol, 1 mM DTT). Protein was then eluted with 3 x 3 mL of elution buffer (300 mM KAc, 50 mM HEPES pH 7.7, 5 mM MgAc₂, 10% glycerol, 1 mM reduced glutathione). Elution buffer was incubated for 5 minutes before elution. Protein was incubated overnight with PreScission protease. Cleaved protein was concentrated and filtered before loading onto a size exclusion column. Fractions contain TubZ-Bm were the concentrated and loaded onto fresh GST-sepharose

and incubated overnight to remove GST contamination and any uncleaved protein. The flow-through was collected and flash-frozen for storage at -80 degrees Celsius.

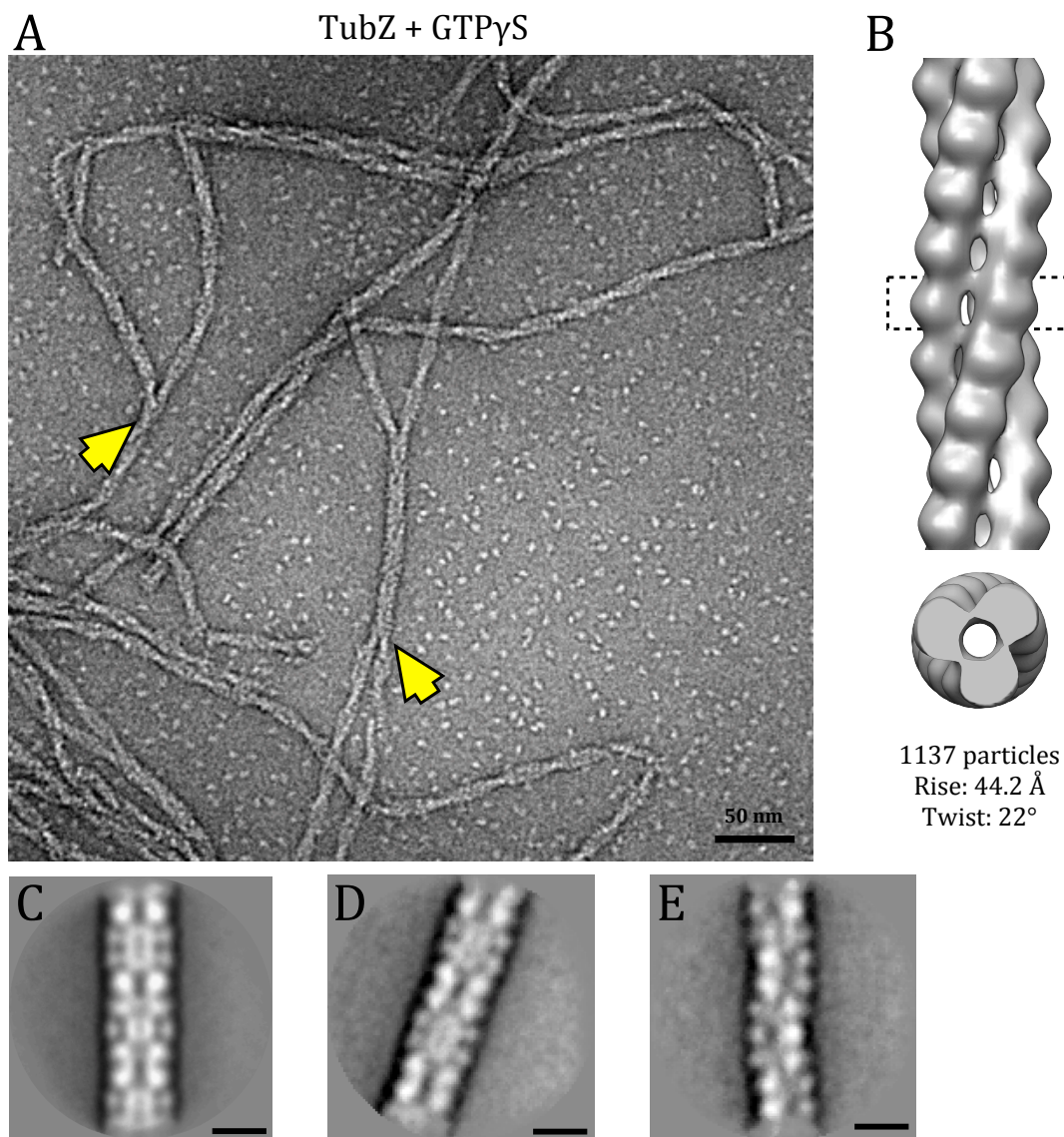


Figure 1. TubZ-Bt:GTP γ S Negative Stain EM reveals 2, 3 and 4 stranded filaments. (A) NS micrograph of TubZ-Bt:GTP γ S showing two-stranded filaments, and thicker filaments highlighted by yellow arrows. (B) Simple NS IHRSR reconstruction of the more abundant subclass of thick filaments, a 3-stranded filament with planar 3-fold symmetry. Class averages of (C) TubZ-Bt:GTP four-stranded filaments, (D) the less populated class of thick filaments in TubZ-Bt:GTP γ S, and (E) the more populated class of thick filaments in TubZ-Bt:GTP γ S. Scale bar is 100Å

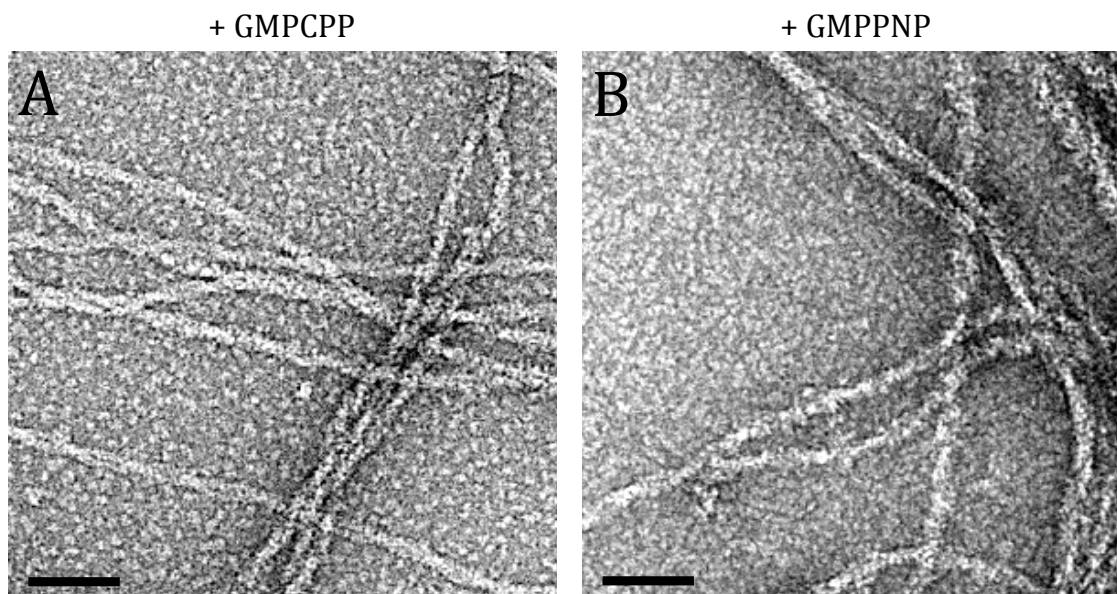


Figure 2. Affects of non-hydrolyzable GTP analogs on TubZ-Bt. NS micrographs of TubZ-Bt grown in the presence of (A) GMPCPP or (B) GMPPNP. Scale bar is 50 nm.

	Oosawa (2 step)	Flyvbjerg: steps	Flyvbjerg: subunits/step	BM: 1 step	BM: 2 step
GTP	~4.94 (5)	~2.82 (3)	~1.96 (2)	4	2/9
GTP γ S	~3.94 (4)	~2.92 (3)	~2.37 (2)	Not calculated	Not calculated

Table 1. Comparison of results of modeling TubZ-Bt nucleation using different methods.

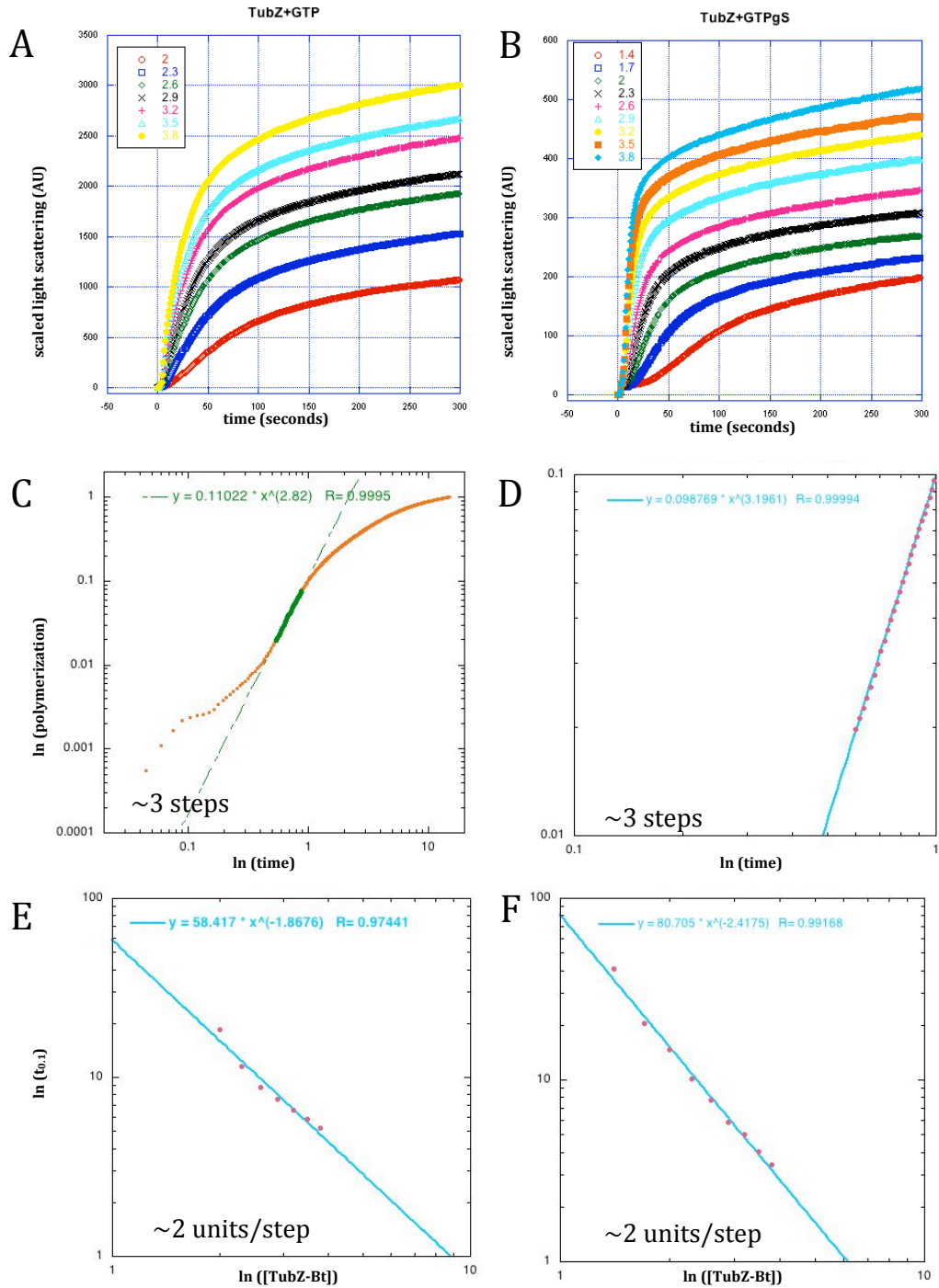


Figure 3. Modeling of TubZ-Bt nucleation via the Flyvbjerg model. Example scaled concentration series of TubZ-Bt with (A) GTP or (B) GTP γ S. Scaled curves (shown in log-log format), and measurement of the initial slope of (C) GTP or (D) GTP γ S. Tenth time vs. TubZ-Bt concentration in log-log format of (E) GTP or (F) GTP γ S.

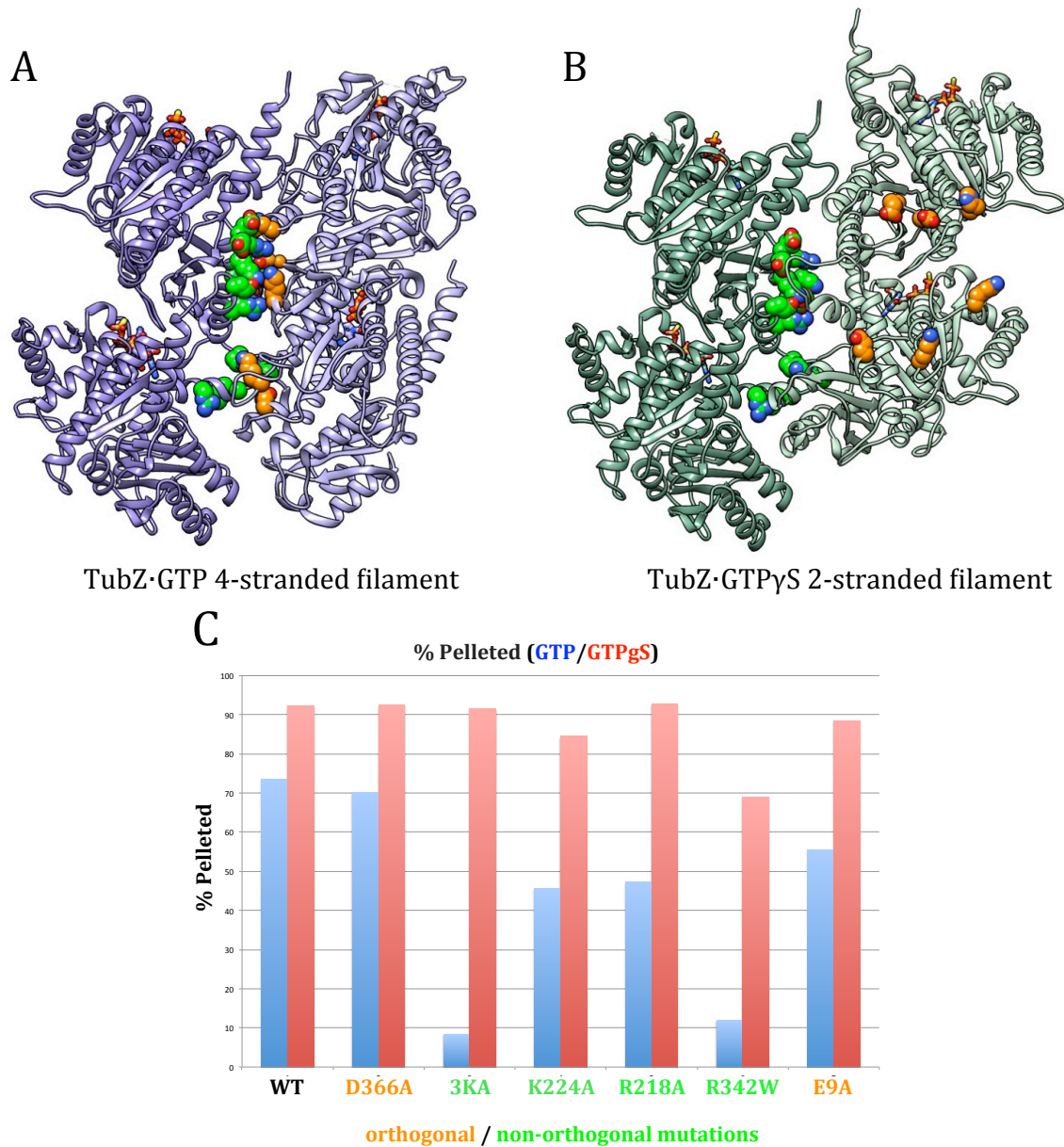


Figure 4. Design of mutants to test filament interfaces. In spheres, charged residues found at the interface of the four-stranded filament on either the (A) four- or (B) two-stranded filament. Green spheres highlight residues found in the interface of both filaments. Orange spheres highlight residues found only in the four-stranded interface. (C) Preliminary filament pelleting assay on select mutants compared to wild-type.

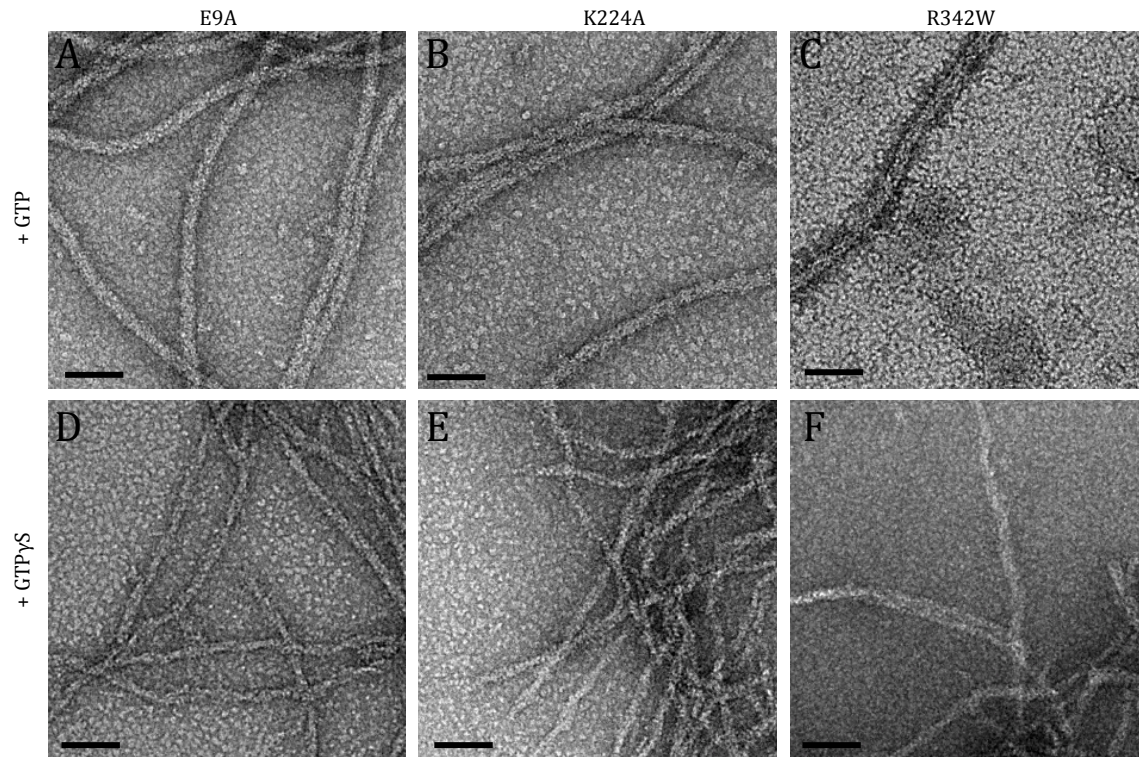


Figure 5. NS electron micrographs of select interfacial mutants. (A),(B),(C) Filaments grown in the presence of GTP of E9A, K224A, and R342W respectively. (D),(E),(F) Filaments grown in the presence of GTP γ S of E9A, K224A, and R342W respectively.

Mutant	Cloned	Purified	Pellet% GTP/GTP γ S	EM change?
WT	yes	yes	73.6%/92.3%	NA
D366A	yes	yes	70.2%/92.5%	no
3K	yes	yes	8.4%/91.6%	Some single protofilaments
K224A	yes	yes	45.6%/84.5%	no
R218A	yes	yes	47.2%/92.8%	no
R342W	yes	yes	11.9%/68.9%	no
E9A	yes	yes	55.6%/88.4%	no
Δ Helix 0	yes	no	x	x
E297A	yes	pellet	x	x
D302A	yes	pellet	x	x
VIV -> A	yes	pellet	x	x
EEGE/D129A	yes	pellet	x	x
EEGE -> A	yes	pellet	x	x
R154A/E155A	yes	pellet	x	x
NSDIK-> A	yes	pellet	x	x
K290A/D292A	yes	pellet	x	x
D201A	yes	pellet	x	x
K227A/K230A	no	x	x	x
E9/H16/K45/K7 3/D366/E366 -> A	no	x	x	x

Table 2. Results of mutagenesis of interfacial and tail residues of TubZ-Bt.

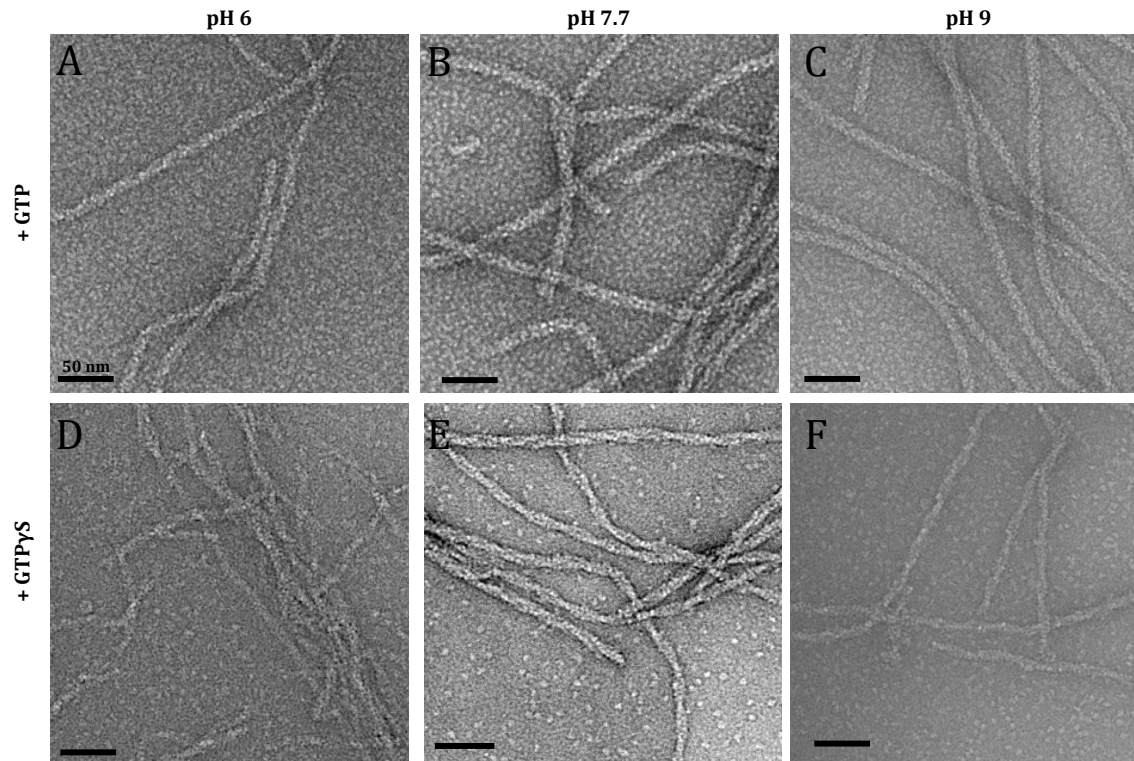
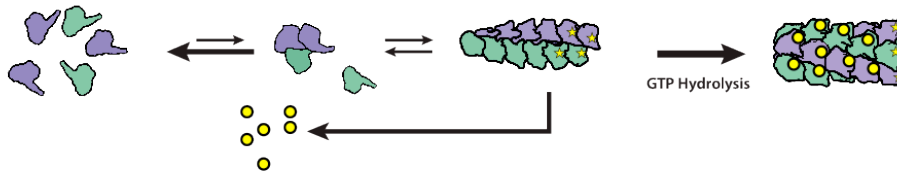
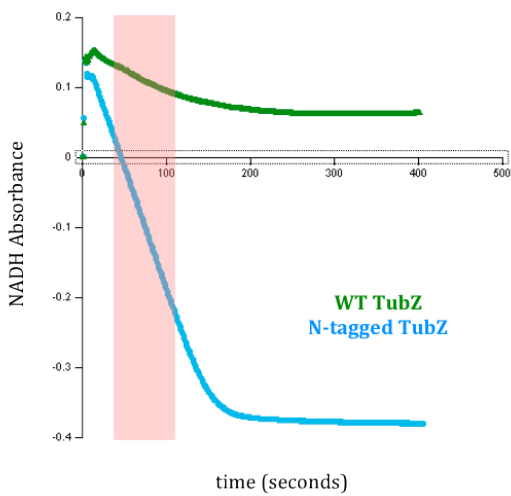


Figure 6. TubZ-Bt filament formation in different pH conditions. NS micrographs of (A) and (D) TubZ-Bt in pH 6 buffer in the presence of GTP or GTP γ S, (B) and (E) TubZ-Bt in pH 7.7 buffer in the presence of GTP or GTP γ S, (C) and (F) TubZ-Bt in pH 9 buffer in the presence of GTP or GTP γ S.

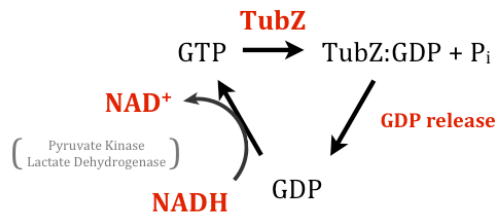
A



B



C Coupled Regenerative GTPase assay:



WT TubZ slope = 1.8 GTP/TubZ·min

N-term tag TubZ slope = 11.3 GTP/TubZ·min

Previously published rate = 16-18/TubZ·min

Figure 7. Coupled Regenerative GTPase assay to determine GDP release rate. (A) Model of expected results; GTP turnover will be high when filaments do not convert to four-stranded morphology, but will be low when they convert as they are trapped within the filament. (B) Preliminary results of assay, red highlight of area of slope measured. (C) Chart of how the assay works and resulting rates.

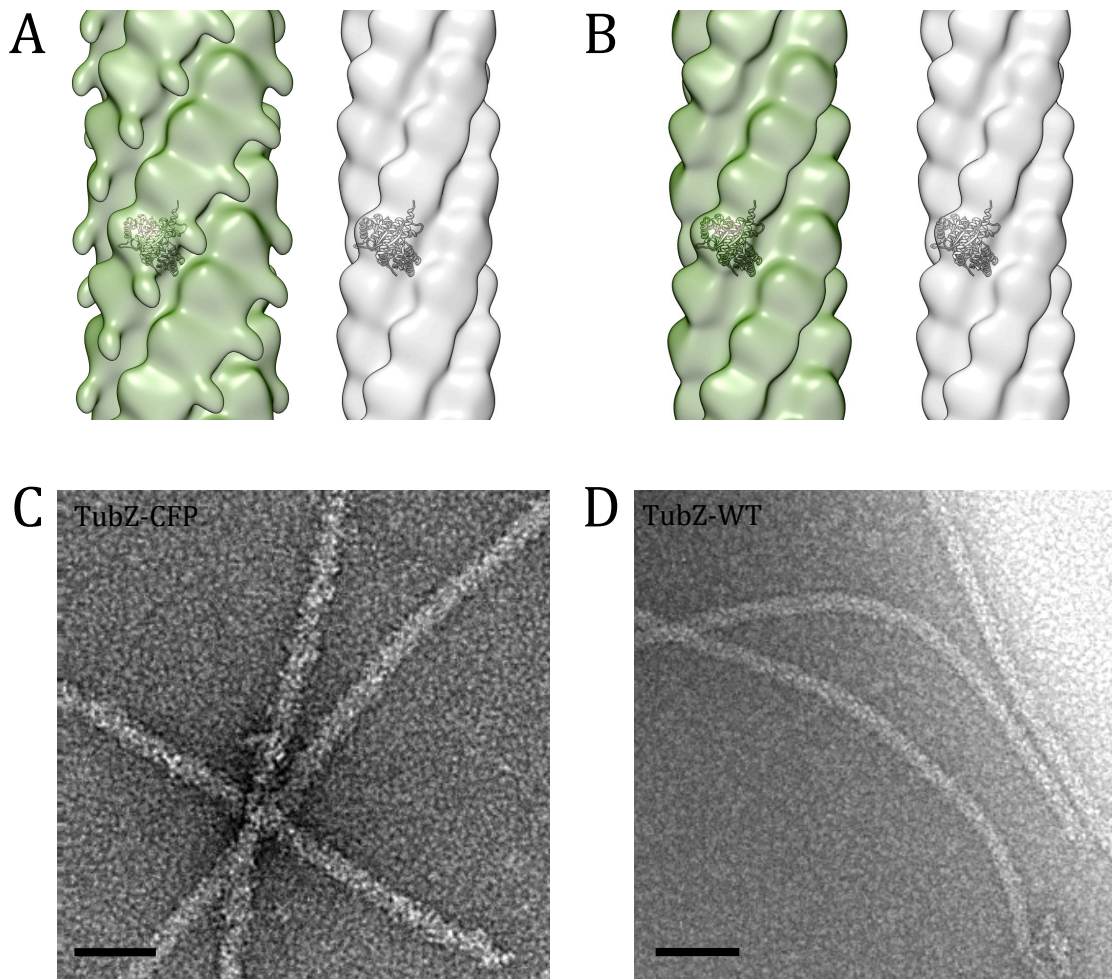


Figure 8. TubZ-Bt with CFP tag on the C-terminus in the presence of GTP. (A) In green, NS reconstruction of TubZ-Bt-CFP vs. gray WT TubZ-Bt at a low contour level (0.05). (B) In green, NS reconstruction of TubZ-Bt-CFP vs. gray WT TubZ-Bt at a higher contour level (0.1). (C) NS Micrograph of TubZ-Bt-CFP in the presence of GTP. (D) NS Micrograph of WT TubZ-Bt in the presence of GTP.

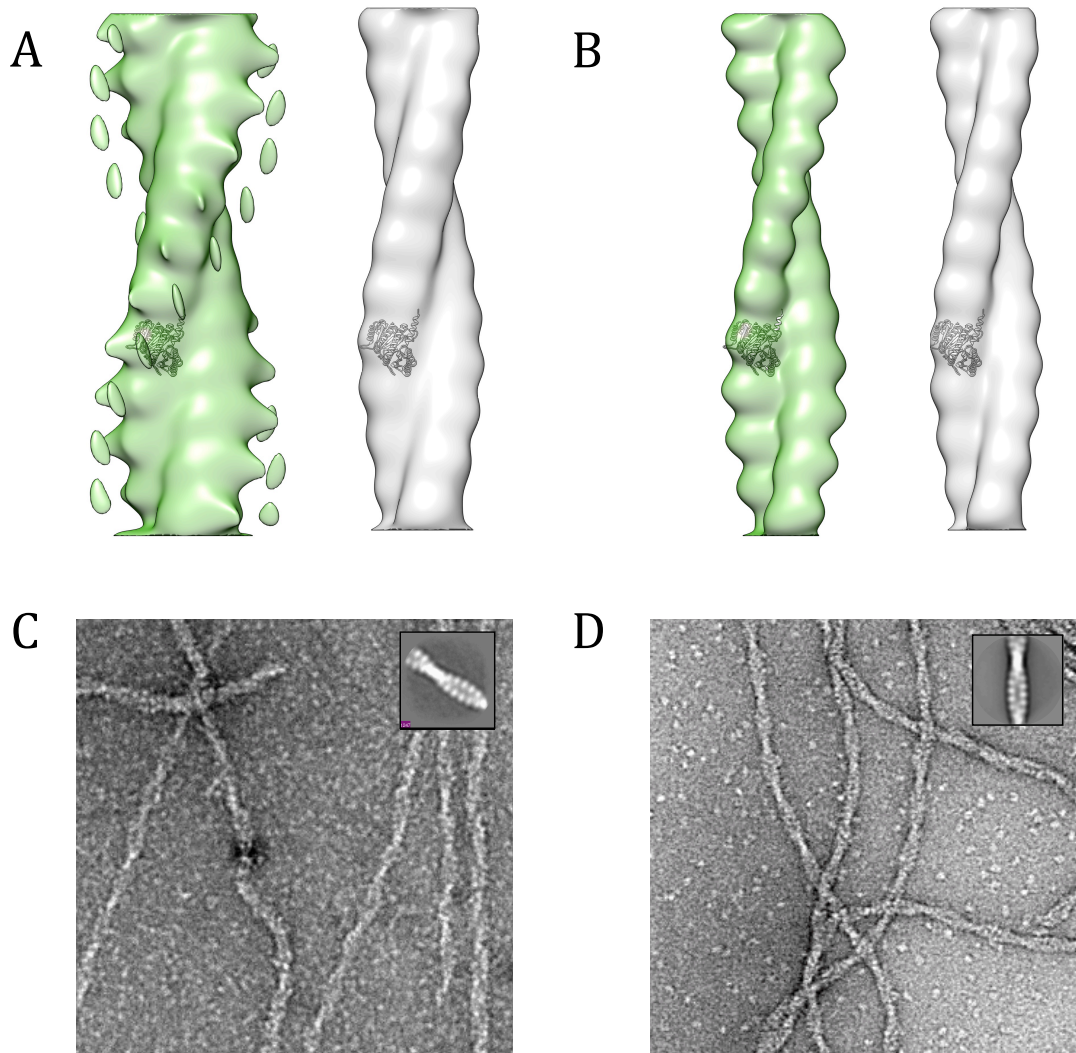
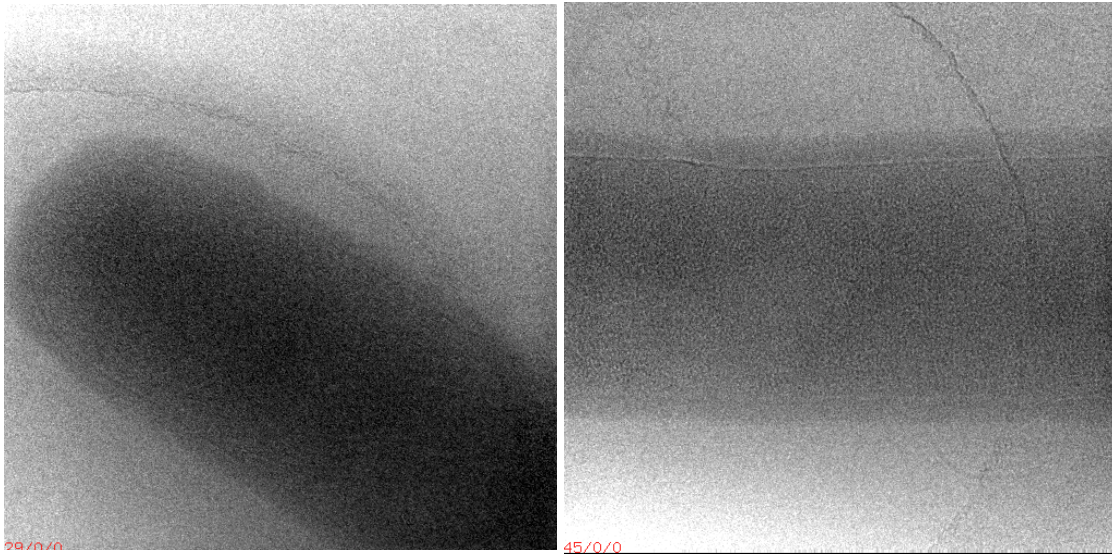


Figure 9. TubZ-Bt with CFP tag on the C-terminus in the presence of GTP γ S. (A) In green, NS reconstruction of TubZ-Bt-CFP vs. gray WT TubZ-Bt at a low contour level (0.005). (B) In green, NS reconstruction of TubZ-Bt-CFP vs. gray WT TubZ-Bt at a higher contour level (0.026). (C) NS Micrograph and class average of TubZ-Bt-CFP in the presence of GTP γ S. (D) NS Micrograph and class average of WT TubZ-Bt in the presence of GTP γ S.

A



B

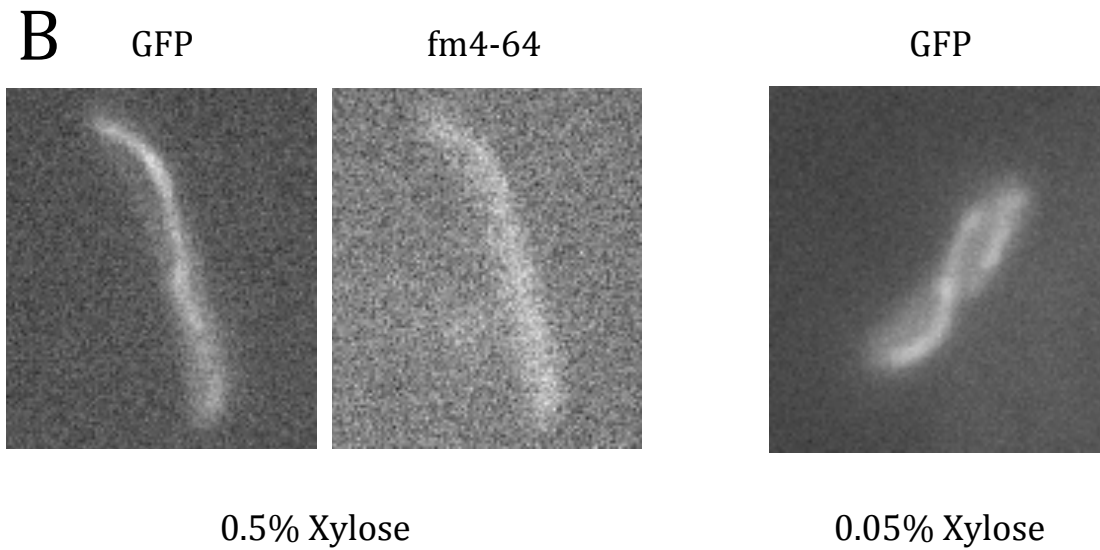


Figure 10. Preliminary results from mini-*Bacillus subtilis* expressing TubZ-Bt. (A) Preliminary tomogram slices of mini-*Bacillus subtilis*. (B) Preliminary results of light microscopy of mini-*Bacillus subtilis* overexpressing TubZ-Bt-GFP or membrane stain fm4-64, with varying expression levels.

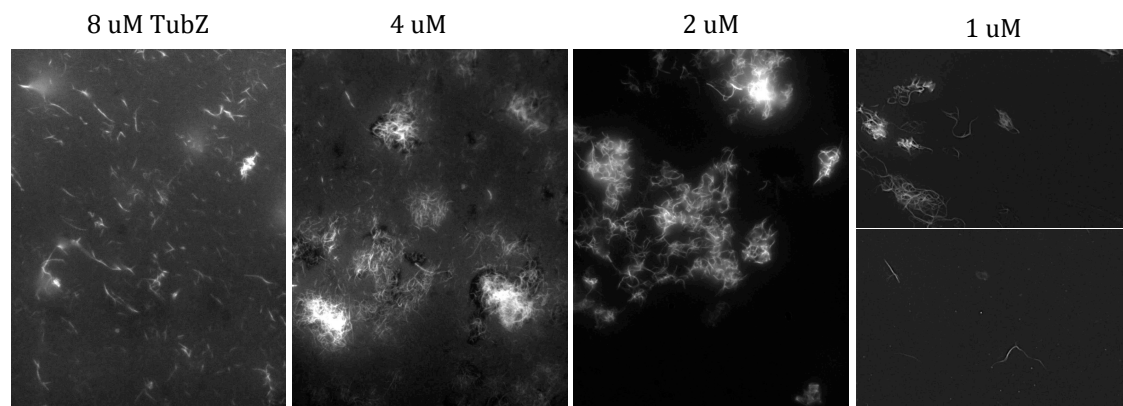


Figure 11. Preliminary light microscopy of TubZ-Bt fluorescently labeled filaments.

10%(8 μ M, 4 μ M, and 2 μ M) or 20% (1 μ M, 0.5 μ M) KKCK-TubZ pET151 labeled with AF488, 90% unlabeled TubZ-pET151, 1 mM GTP γ S, varying concentrations.

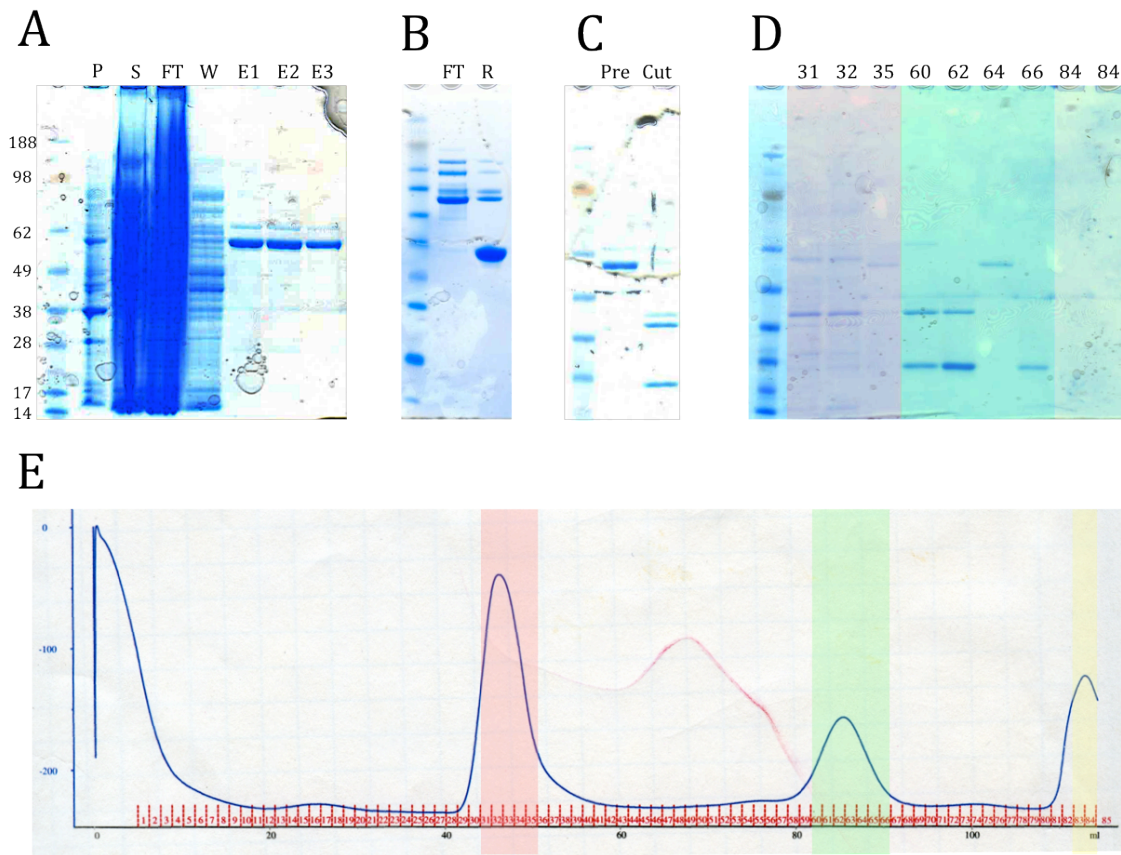


Figure 12. Purification of TubZ-Bm with cleavable GST-tag. (A) SDS-PAGE of lysis through Glutathione affinity column [P: pellet, S: clarified supernatant, FT: flow-through, W: wash, E1-E3:sequential elutions]. (B) SDS-PAGE of flow-through (FT) and protein retained on glutathione sepharose beads (R). (C) Pre- and Post PreScission(r) protease cleavage. (D) SDS-PAGE and (E) chromatogram of size exclusion chromatography (S200). Blue trace is A280.

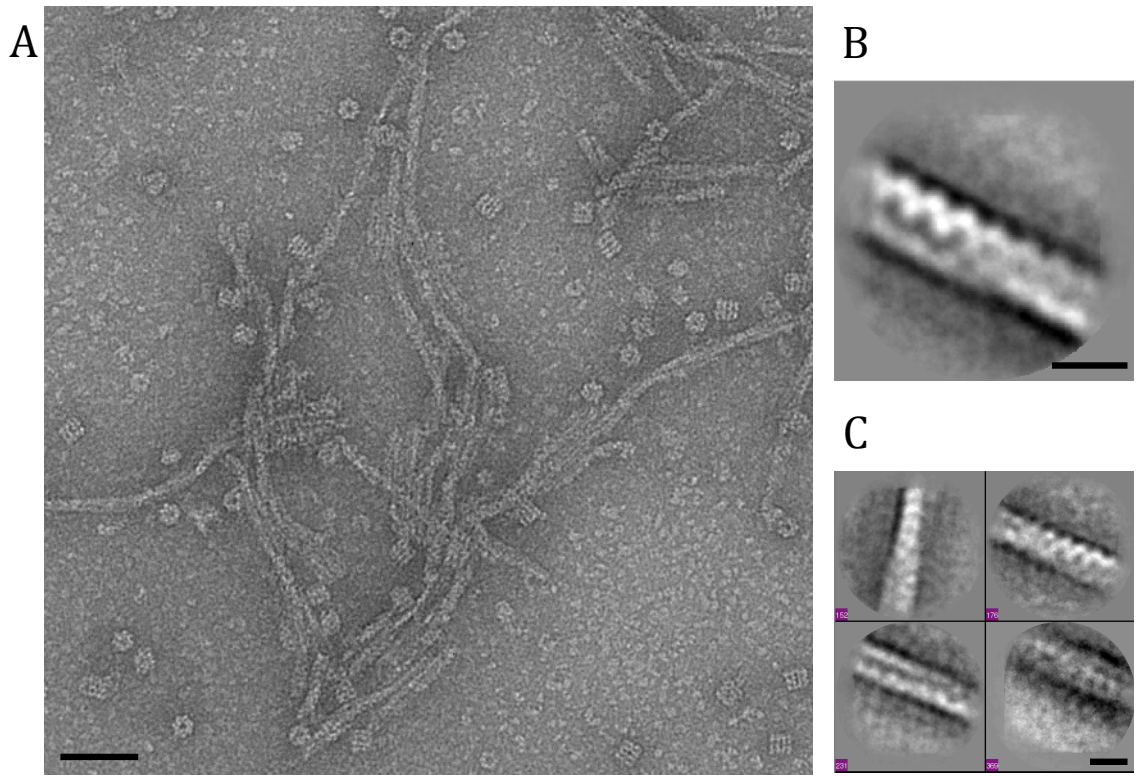


Figure 13. Negative stain EM of TubZ-Bm + GTP γ S. (A) Micrograph of 16 μ M TubZ-Bm. Scale bar 50 nm. (B) and (C) Class-averages of overlapping filament particles, with one or four classes respectively.

References

1. Oosawa F and Asakura S (1975) *Thermodynamics of the Polymerisation of Protein* (Academic Press, London).
2. Kasai M, Asakura S, & Oosawa F (1962) The cooperative nature of G-F transformation of actin. *Biochim Biophys Acta* 57:22-31 .
3. Nishida E & Sakai H (1983) Kinetic analysis of actin polymerization. *J Biochem* 93(4):1011-1020 .
4. Flyvbjerg H, Jobs E, & Leibler S (1996) Kinetics of self-assembling microtubules: an "inverse problem" in biochemistry. *Proc Natl Acad Sci U S A* 93(12):5975-5979 .
5. Chen Y & Erickson HP (2008) In vitro assembly studies of FtsZ/tubulin-like proteins (TubZ) from Bacillus plasmids: evidence for a capping mechanism. *J Biol Chem* 283(13):8102-8109 .
6. Ingerman E & Nunnari J (2005) A continuous, regenerative coupled GTPase assay for dynamin-related proteins. *Methods Enzymol* 404:611-619 .
7. Aylett CH, Wang Q, Michie KA, Amos LA, & Lowe J (2010) Filament structure of bacterial tubulin homologue TubZ. *Proc Natl Acad Sci U S A* 107(46):19766-19771 .
8. Ni L, Xu W, Kumaraswami M, & Schumacher MA (2010) Plasmid protein TubR uses a distinct mode of HTH-DNA binding and recruits the prokaryotic tubulin homolog TubZ to effect DNA partition. *Proc Natl Acad Sci U S A* 107(26):11763-11768 .
9. Pilhofer M & Jensen GJ (2013) The bacterial cytoskeleton: more than twisted filaments. *Curr Opin Cell Biol* 25(1):125-133 .

10. Oliva MA, Martin-Galiano AJ, Sakaguchi Y, & Andreu JM (2012) Tubulin homolog TubZ in a phage-encoded partition system. *Proc Natl Acad Sci U S A* 109(20):7711-7716 .
11. Ludtke SJ, Baldwin PR, & Chiu W (1999) EMAN: semiautomated software for high-resolution single-particle reconstructions. *J Struct Biol* 128(1):82-97 .
12. Aylett CH & Lowe J (2012) Superstructure of the centromeric complex of TubZRC plasmid partitioning systems. *Proc Natl Acad Sci U S A* 109(41):16522-16527 .
13. Egelman EH (2007) The iterative helical real space reconstruction method: surmounting the problems posed by real polymers. *J Struct Biol* 157(1):83-94 .
14. Scholle MD, White CA, Kunnimalaiyaan M, & Vary PS (2003) Sequencing and characterization of pBM400 from *Bacillus megaterium* QM B1551. *Appl Environ Microbiol* 69(11):6888-6898 .

Chapter Six

Initial Studies into the interaction of TubZ-Bt filaments with TubRC centromeric adaptor complex.

Introduction

As previously mentioned in chapters four and five, TubZ-Bt belongs to a three component system, which is thought to be canonical for known plasmid segregation systems (although there have been recent data suggesting that some systems may have evolved to use other proteins (1, 2)). These systems, including TubZ-Bt, all rely on a cytoskeletal NTPase component, a DNA binding protein which serves to link the plasmid and filamentous protein via the third component, a centromeric binding region which often contains palindromic or pseudo-repeat sequences (reviewed in (3)).

TubR-Bt is located upstream of TubZ-Bt and was initially found to bind to a set of 4 12 base pair pseudo-repeat iterons upstream of its coding region (4, 5). It was later shown that the *tubC* centromeric binding region has an additional 3 12 base pair iterons further upstream (6). TubR-Bt was crystallized by the Schumacher group in 2010, and was found to be a winged helix-turn-helix protein with a unique conformation. TubR binding was also found to be to the TubZ-Bt C-terminal region through anisotropy (7). Recently a low-resolution structure of TubR-Bt with DNA was solved by the Löwe group, as well as a higher resolution structure of TubR *sans* DNA from *B. megaterium*. They were unable to locate the *tubC* from *B. megaterium* but they were able to show that TubR-Bm forms circular filaments when bound to *tubC*-Bt DNA as well as pBM400 DNA. Additionally they were able to demonstrate that some TubRC complex binding has a stimulatory effect on TubZ-Bt filament growth (6).

Much of the experiments outlined in this chapter confirm work that has already been published, although the majority of it was done before these publications were communicated. Most of the results are in agreement with the publication data, although

there are some subtle discrepancies. We received the DNA for TubR and the tubZRC operon as a kind gift from Marcella Erb and Dr. Joe Pogliano's Lab at UCSD. We were able to recombinantly purify TubR-Bt with affinity purification but the protein is not especially stable in the absence of *tubC* DNA in buffer compatible with optimal TubZ-Bt polymerization. We were able to show binding of varying length pieces of *tubC* DNA, discovering that TubR dimers bind to extended pieces of DNA, beyond the originally identified *tubC* binding sequence. It appears that the TubR binding is cooperative, and although it needs the *tubC* iteron sequence to bind to DNA but this allows spreading onto non-pseudo repeat sites.

One major goal we had for experiments with the TubRC complex was to understand the mechanism with which it interacts with TubZ filaments, and its relationship to the morphological changes that we observe. Although multiple attempts were made to characterize this, it has proven difficult to get a definitive answer as to where on the filaments the TubR complex preferentially binds. Additionally, TubZRC binding appears to have only a minor effect on the TubZ morphology and it is unclear whether this is a real effect or whether it is due to protein crowding effects. TubRC binds with similar strength to both TubZ:GTP γ S filaments and TubZ:GTP filaments, and appears to stimulate growth of both forms. Further investigation is necessary to understand the interaction between TubZ filaments and the DNA adaptor complex, although some inroads have already been made. Suggestions of future experiments are outlined in chapter 7.

Results and Discussion

Expression and purification of TubR-Bt

We were sent the cDNA for TubR-Bt cloned into the pET28a expression vector (Novagen). This contains an n-terminal 6x-his-tag. We were able to overexpress TubR in *E. coli*. Using the purification scheme for his-tagged TubZ as a starting point, we were able to purify TubR using a combination of Ni-NTA affinity chromatography and size exclusion chromatography to high purity (Figure 1 A-C). Several different sets of purification buffers gave the same results, and all the purification schemes tried will not be outlined. Although the his-tag of this construct is cleavable, for most experiments, the tag was left intact. The protein alone was particularly stable in the HMK100 buffer used for TubZ polymerization or other various buffers (as determined by precipitation) however addition of *tubC* DNA stabilizes the protein in a complex for further experimentation. Additionally a TubR was cloned in expression vector pET29b to give a construct with a c-terminal his-tag, during initial purifications it was apparent that much of this protein was not soluble, so further investigation was halted. Other purifications strategies and constructs that appear to work equally well or better are shown in papers from either the Schumacher group (7) or the Löwe group (6).

Initial characterization of TubR binding to tubC

At the time we started these experiments, only initial characterization of the *tubC* binding sites had been accomplished (4, 5). We first did multi-angle light scattering (MALS) to determine the oligomeric state of TubR in the absence of DNA, and we found that it exists in solution as a dimer (Figure 2). This is confirmed by the crystal structure (7). As part of initial efforts to crystallize TubR in the presence of DNA, we made a number of short

constructs consisting of just the 12 base pairs of the identified pseudo-repeats sequence, or with segments of adjacent sequence, varying from 12-36 base pairs.

Using a DNA gel shift assay, we are able to see that TubR is not able to bind to an oligonucleotide that is just 12 base pairs (Figure 3), indicating that each TubR dimer requires more than just the pseudo-repeat sequence to bind. Further analysis of other oligonucleotides indicate that even 24 base pair oligonucleotides surrounding each iteron sequence have much poorer binding than if you increase the oligonucleotides length up to 32 or 36 base pairs. Additionally it appears that the central iterons have stronger binding than the two oligonucleotides on either end of the 48-bp identified sequence (Figure 3).

To determine how many TubRs bound to these sequences, we performed MALS of TubR + the 48 base pair oligonucleotides, TubR + iteron 2 + 6 base pairs on either side (24 base pairs), and TubR plus a 48 base pair sequence including iterons 2+ 3 surround by 12 base pairs of random sequence on either side. Surprisingly TubR + the 48 base pair oligonucleotide containing all four iterons only bound 2-3 dimers, indicating that a longer sequence was necessary to cover all the DNA. Only one TubR bound to the 24 base pair sequence as expected. Additionally, the 48 base pair oligonucleotide including only iterons 2 + 3 appeared to bind only 1-2 TubRs, indicating that specific sequence is necessary for the extended binding of TubR past this region, perhaps hinting at why binding of iterons 1 and 4 is weaker than 2+3. It should be noted however, that this entire region of pBtoxis is quite AT-rich, as is the pseudo-repeat sequence.

We also wished to see if binding extended beyond the iteron binding sequence. To do this, we used PCR to create oligonucleotides of the TubZRC binding region. We created oligonucleotides of 150, 200, or 300 base pairs centered on the 48 base pair known iteron

sequence. By gel shift, we see that binding occurs when TubR is added to both the 200bp and 300 base pair oligonucleotides, but also that there is an additional shift at greater TubR:DNA ratios, indicating that TubR does in fact bind past the originally identified binding sequence (Figure 6).

In order to characterize the nature of these TubRC DNA:protein complex, we visualized them using negative stain EM. We first visualized complexes of TubR:48 base pair oligonucleotide and TubR:60 base pair oligonucleotide. Confirming the results of the MALS of TubR:48 base pair oligonucleotide, most of the complexes of TubR:48 base pair oligonucleotide had 3 TubR dimers bound (Figure 7A). The TubR:60 base pair oligonucleotide complex comprised of mostly 4 TubR dimers bound, indicating the addition of the flanking nucleotide sequence is necessary for full occupancy (Figure 7B). We further characterized these TubR:60 base pair complexes by class-average. We see that it does not appear to have regular structure, but rather acts as beads on a string.

Additionally we want to understand the binding of TubRC complex made with the extended oligonucleotides. We look by negative stain EM at complexes of TubR:150 base pairs, TubR:200 base pairs, and TubR:300 base pairs. We see that all three oligonucleotides have binding extending past the 4 pseudo-repeat sequences, and the longer the oligonucleotide is, the more TubR dimers are bound (Figure 9). This indicated that either TubR was able to binds cooperatively and/or that there were additional undiscovered binding sequences outside of previously identified ones. We further inspected the sequence to determine if there were additional sites, and it appeared that there were three additional upstream 12 base pair sequences with high similarity to the four previously identified pseudo-repeats (Figure 10). If we inspect our 150 base pair sequence, we see that it only

contains part of one of these extra iterons, and we often see binding of 6-7 TubR dimers by EM (Figure 9A), and the 200 and 300 base pair TubR:oligonucleotide complexes also appear to have more than 7 TubR dimers bound (Figure 9B and C). This indicates that TubR is able to bind cooperatively to DNA, starting binding at the iteron binding sequences, and spreading out along the DNA. These binding sites and the cooperativity of TubR binding to DNA were later confirmed in a paper by the Aylett, et al by DNA fingerprinting and gel shift (6).

Initial characterization of TubRC interaction with TubZ-Bt filaments

To understand how TubZ is able to interface with TubR and the pBtoxis DNA, we wished to determine the structure and binding of TubRC complex to TubZ filaments. It has been previously determined that TubRC binds to TubZ via the C-terminal region (7), but little else has been established about the interaction of these components. Because we had previously observed that nucleotide state affects the morphology of the TubZ filament in chapter 4, we wished to determine if TubRC binding either affected or was affected by these morphological changes. We first determined whether TubRC bound to both forms of filaments by pelleting assay. In this assay, TubZ-Bt filaments are formed in the presence of nucleotide and then spun-down at high speed. If TubRC binds to the filaments, we should see it in the pellet (Figure 11A). We see negligible amounts of TubRC complex in the pellet when it is spun at high speeds alone, or with TubZ in the presence of no nucleotide. However, when we pellet the mixture of TubRC and TubZ in the presence of either GTP or GTP γ S, we see that TubRC does bind to TubZ filaments (Figure 11B). We saw no obvious increase in TubZ-Bt filament formation, however the conditions used in the assay are

already robust conditions for polymerization. We did note, however, that by eye, there was a suggestive difference in the amount of TubRC complex that co-pelleted with the TubZ-Bt filaments – slightly more TubRC complex appeared in the pellet of GTP formed filaments.

To follow up on this observation, we repeated the pelleting assay using several concentrations of TubRC complex to fit a binding curve (Figure 12). From this analysis, we observed only a slight increase in binding to the TubZ-Bt filaments formed in the presence of GTP versus GTP γ S (2 μ M versus 3 μ M K_D). This assay was only performed once, so it bears repeating to see if this difference in binding remains. One flaw in the way this was done is that both GTP and GTP γ S binding were performed using untagged protein. This means that the GTP γ S filaments likely contain four-stranded filaments that will skew the binding results even if the TubRC complex binds preferentially to four-stranded filaments versus two-stranded filaments. This can be avoided by using the N-terminally tagged version of TubZ-Bt that blocks four-stranded filament formation, although these results can then not be directly compared to the GTP results.

We wished to observe whether TubRC complex would stimulate TubZ-Bt filament formation in condition where TubZ-Bt alone would form a limited number of filaments. We did this by observing filament formation by 90-degree light scattering of either TubZ-Bt alone at a low concentration, or in the presence of varying amounts of TubRC complex using a 60 base pair *tubC* oligonucleotide. By this method, it is obvious that TubRC complex does in fact have a stimulatory effect on TubZ filament formation in the presence of GTP (Figure 13A). It appears to have a slight effect on TubZ filament formation in the presence of GTP γ S (Figure 13B), however, this assay needs to be repeated at a lower concentration of TubZ-Bt to understand the real effect of TubRC stimulation of GTP γ S filaments. The

published results from Aylett, et al. confirm this result, and point out another potentially interesting result. They used both 48-base pair oligonucleotides and oligonucleotides with the full-length *tubC* sequence. They noticed a ~2-fold increase in stimulation in polymerization when they used the full-length *tubC* sequence over the shorter oligonucleotide. Our previous results suggest that a 48-base pair oligonucleotide does not provide full binding for all four originally identified sites, so it is unclear whether there would be an increase between the 60-base pair oligonucleotide and the full set of sites, so this experiment should be included in any future directions. Another interesting observation that can be made from this data is that increase the TubRC concentration does not have a linearly increasing effect on TubZ filament formation, suggesting that the complex maybe only needed at a limited number of sites (such as the ends of filaments) to have this stimulatory effect.

Finally, we wished to observe whether TubRC affected the morphology of TubZ-Bt filaments, and whether we could detect where on the TubZ-Bt filaments. To do this we used negative stain EM and a variety of different conditions. We had already observed with light scattering that the relative plateaus of TubZ:GTP and TubZ:GTP γ S in the presence of TubRC were similar to those observed without any complex presence, suggesting that it was unlikely that a dramatic change in morphology would occur. By negative stain EM, we see this is by and large true. TubZ:GTP γ S maintains a majority of two-stranded filaments, without a noticeable increase of thick filaments (Figure 14C). TubZ:GTP filaments are mostly four-stranded, however, we do observe an increase in observed two stranded (Figure 14E) filaments. We also observe an increase in disrupted or 'loose' filaments (Figure 14A, F, H). It is unclear however, whether this is an affect of TubRC binding or

whether it is due to general protein crowding affects – observations should be made in the presence of equimolar amounts of a generic protein such as BSA.

By negative stain, we have also never been able to successfully identify the binding site of TubRC complexes, despite multiple efforts trying to do so. Adding a saturating amount of TubRC complex does not appear to coat either ends or sides of TubZ-Bt filaments, nor does adding a slight amount of the cross-linker gluteraldehyde. Attempts at using gold-labeling on oligonucleotides or on TubR His-tags also did not reveal new information about this and are not shown in this work. In the negative stain EM we are able to see both interesting ends (Figure 14B) and areas that appear to have TubRC lying on top of TubZ-Bt filaments (Figure 14G, I). There are many potential areas of exploration to try and identify these binding sites, so there are many future directions that can be taken here. This is an area of high interest, as none of the TubZ systems have yet been visualized binding their adaptor complexes.

Methods

Cloning of TubR

TubR-pET28a was cloned by the lab of Dr. Joe Pogliano at UCSD. It was cloned using the EcoRI and NdeI restriction sites with an N-terminal his-tag. TubR-pET29b was cloned using directional cloning using the XhoI and NdeI restrictions with a C-terminal his-tag.

Expression and Purification of TubR-Bt-pET28a

TubR-Bt-pET28a was transformed into BL21 Star™ (DE3) (Invitrogen) cells and grown to an OD600 of ~0.5 before induction with 1 mM IPTG. Several different methods of

purification were attempted but outlined is just the purification shown in figure 1. A cell pellet from a 1L overexpression was resuspended by dounce in Hi-Salt buffer (500 mM KCl, 50 mM HEPES pH 8.0, 10% glycerol, 10 uM 1-thioglycerol, 2 EDTA-free protease tabs (SIGMA)) and then lysed for 10 minutes in the using the Emulsiflex-C3 (Avastin). The lysate was then centrifuged at 35k x g for 40 minutes. Imidazole pH 8.0 was added to 10 mM to clarified lysate, and then clarified lysate was loaded onto 2 mL bed volume of NiNTA beads from Qiagen pre-equilibrated with Hi-salt buffer, and incubated with nutation for 1 hr. Resin was then drained and washed with 100 mL buffer (500 mM KCl, 50 mM HEPES pH 8.0, 10% glycerol, 10 uM 1-thioglycerol, 25 mM imidazole). Sample was then eluted 4 times using 2 mL elution buffer (500 mM KCl, 50 mM HEPES pH 8.0, 10% glycerol, 10 uM 1-thioglycerol, 250 mM imidazole). Elutions E2- E4 were loaded onto a S200 16/60 HiLoad column (GE Life Sciences) using S200 buffer (500 mM KCl, 50 mM HEPES pH 8.0, 10% glycerol, 10 uM 1-thioglycerol). Peak fractions were collected and concentrated. In cases where TubR was cleaved, ~30 µl of 10 mg/mL thrombin (SIGMA) was added to eluates and incubated overnight before loading onto the sizing column.

DNA gel shift assays with TubR-Bt

Short oligonucleotides were synthesized by ElimBio or Eurofins MWG Operon, and reverse complementary pairs were formed by heating to 90 degrees C for 5 minutes, and then allowing to slowly cool to RT in pre-heated block. 60-bp oligonucleotide has a sequence of 5' tgtggctaaaggtttaataacagtttaaatttaagtttaactttcagtttacatcacat 3' and 1 + 3, and 2+3 have randomized sequences [taaaggtttaagtggtgtgtgttttaagtttaacgtgtgtgtgtgt, and gcgcgcgcgcgctaacagtttaaatttaagtttaacgcgcgcgcgcgc, respectively). 150, 200 and 300 base

pair oligonucleotides were PCRred from the TubZRC coding region using the following primers :

150 for: ggtttaaatttctgggggttatag

150 rev: cttgagagtggaaaaattcacc

200for: ggacggtttaaatttaaattaat

200rev: ggtaactcccatctgtttaattaa

300for: ggtagacattaagtttatataaa

300rev: ctgcaatttctgcaatgtttaacg

Gel shifts were performed in two ways. Samples were either mixed with ethidium bromide and DNA gel loading dye and run on a 2% agarose gel, or using the EMSA kit from Molecular Probes™ (Invitrogen). This kit uses a 6% DNA retardation gel and SYBR® Green EMSA nucleic acid gel stain.

MALS

Multi-angle Light Scattering was performed using the size exclusion chromatography on the Ettan System (GE Healthcare Life Sciences), followed by the MALS on the Dawn Heleos (Wyatt Technologies). Samples were run in S200 after pre-incubation with oligonucleotides.

Negative Stain Electron Microscopy

About 5 µl sample solution was pre-incubated at room temperature with nucleotide and applied to a glow-discharged carbon coated grid. Samples were negatively stained with 0.75% uranyl formate, and imaged either on a Tecnai T12 Spirit or a Tecnai T20 (FEI Co.)

operating at 120 kV. Grids of oligonucleotide + TubR-Bt were made by imaging various ratios of TubR:DNA, and the best images were selected. Reference free class averages were made using the EMAN1.9 package startnrclasses (8).

For 300 base pair oligonucleotide and plasmid + TubR binding to TubZ filaments, 75 nM TubRC complex (300 base pair) or ~3 nM TubZRC region plasmid-borne DNA was incubated with 3 μ M untagged TubZ-Bt in the presence of GTP before application to grid. For TubRC +TubZ-Bt:GTP γ S grids, 300 nM TubRC complex was incubated with 2.8 μ M untagged TubZ-Bt in an excess of GTP γ S. For gluteraldehyde stabilization, 600 nM TubRC complex and 2 μ M untagged TubZ-Bt were incubated with excess GTP for 10 minutes, and then incubated with 0.1% gluteraldehyde for 3 minutes before applying to grid. For grids with “saturating” TubRC complex, 4 μ M TubZ was pre-incubated with excess GTP for 10 minutes, and then concentrated TubRC complex was added and incubated for an additional 2 minutes before applying to grid.

TubZ-Bt/TubRC-Bt pelleting assays

To perform initial TubZ co-pelleting assays, 3 μ M untagged TubZ-Bt was incubated with either 1 mM GTP or GTP γ S, and 750 nM TubRC complex using the 60bp oligonucleotide. The mixture was incubated at room temperature for 10 minutes, and then spun down in a TLA100.1 (Beckman Coulter) at 55k rpm for 30 minutes. An aliquot of supernatant was removed from top for analysis before decant the remaining supernatant. The pellet was resuspended an equal volume of buffer as the reaction (HMK100: 50 mM HEPES pH 7.7, 5 mM MgAc₂, 100 mM KAc). Pelleting assays used to make binding curves were performed in the same way, except that the TubRC complex amount was allowed to

vary from 125 nM complex (1 μ M TubR) to 1 μ M (8 μ M TubR). Curves were then fit using KaleidaGraph (Synergy Software).

TubZ-Bt/TubRC-Bt light-scattering

90-degree light scattering experiments were measured using stopped-flow system designed in-house. An excitation wavelength of 530 nm was used. For assays, 2.8 μ M TubZ was mixed 1:1 with 300-1200 nM TubRC complex formed with 60bp oligonucleotide, with 1 mM of either GTP or GTP γ S.

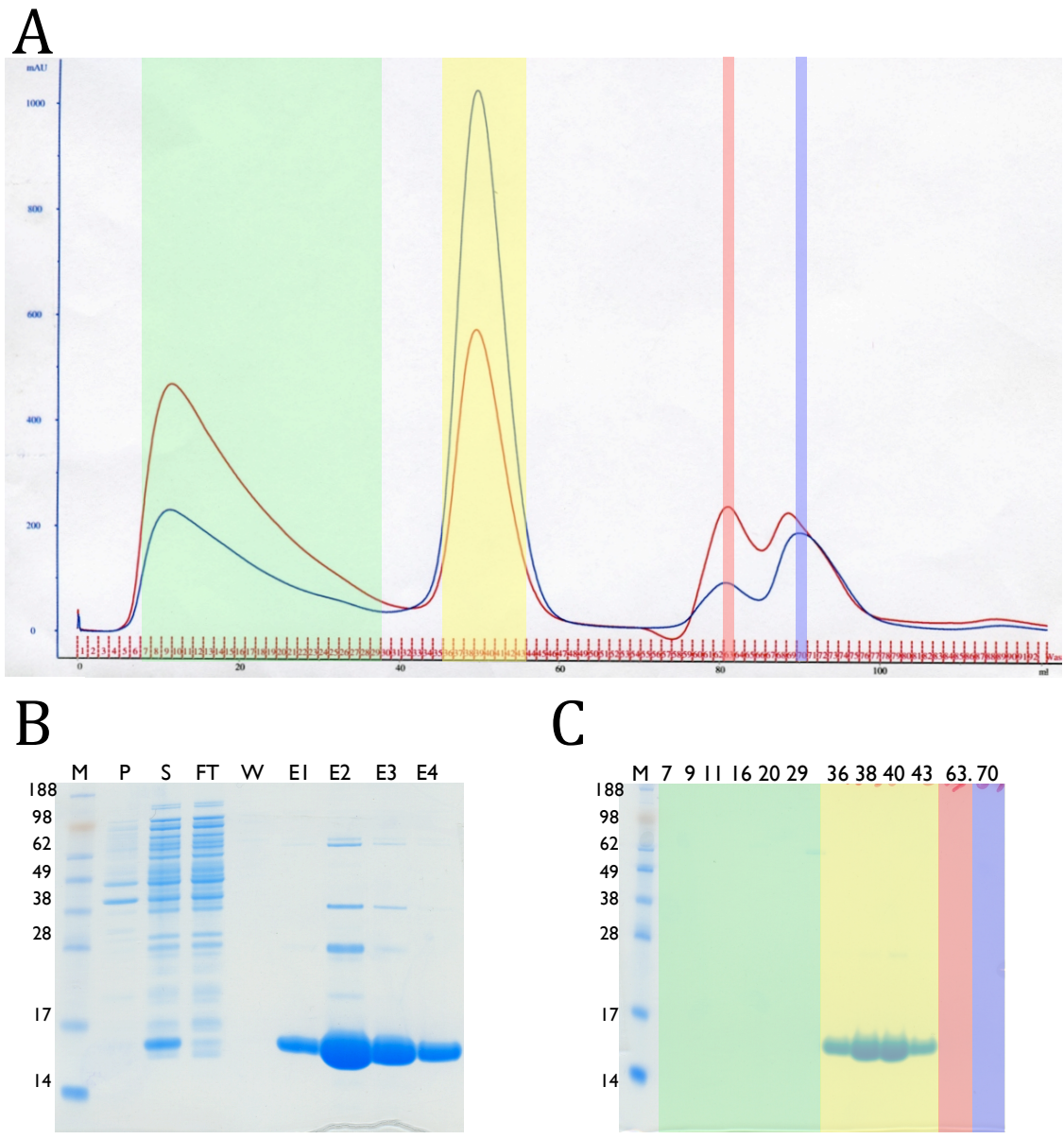


Figure 1. Purification of N-terminally His-tagged TubR. (A) Chromatogram of S200 size exclusion chromatography. Blue trace A280, red trace A260. (B) SDS-PAGE of Ni-NTA affinity chromatography. (C) SDS-PAGE of fractions from (A).

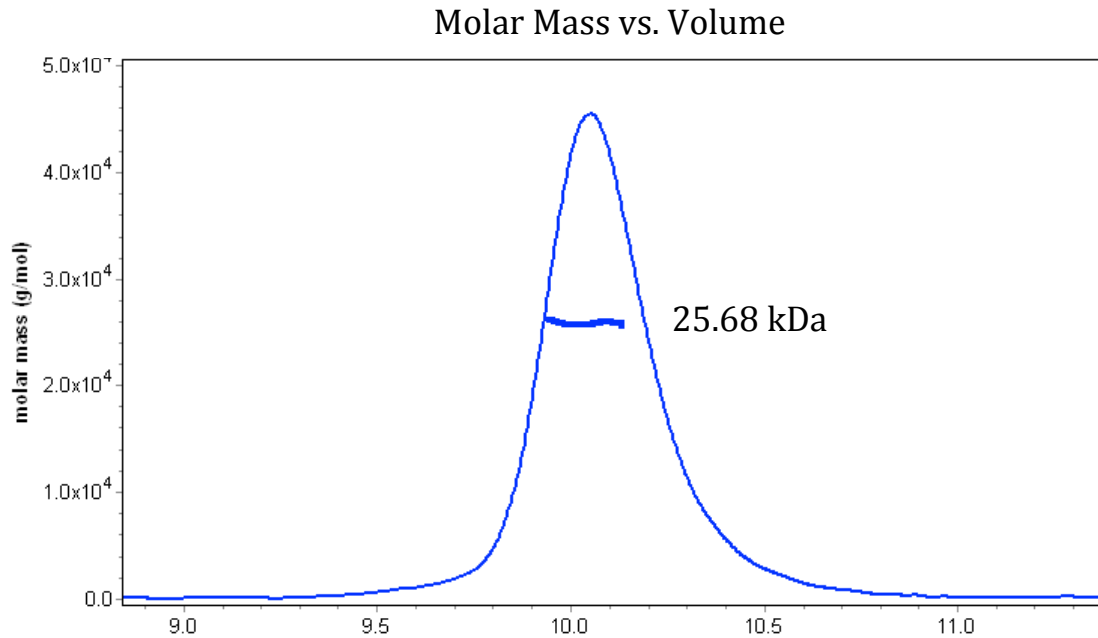


Figure 2. MALS of TubR indicating it is a dimer in solution.

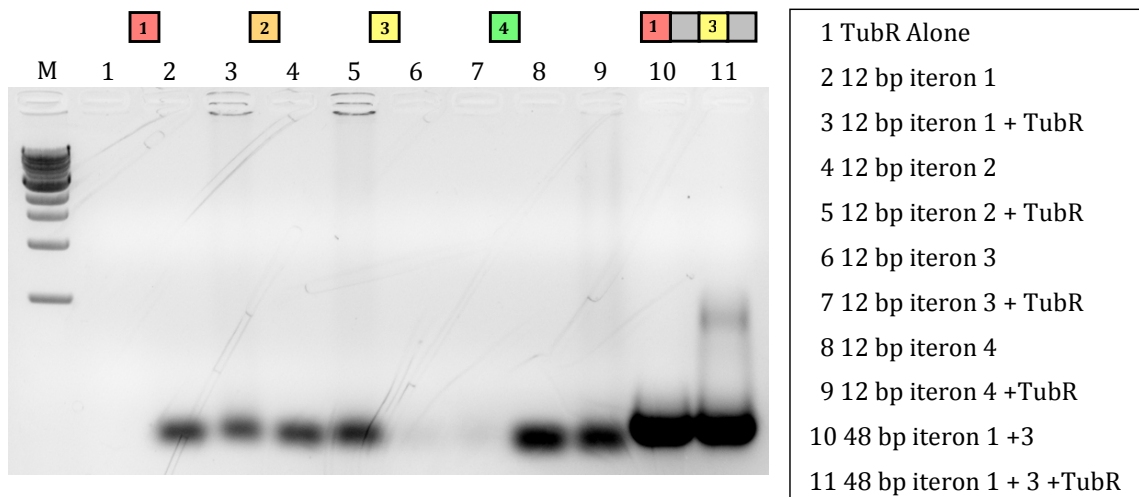


Figure 3. Gel shift assay of short oligonucleotides of the iteron sequences found to be important for TubR binding, indicating that TubR needs an oligonucleotide extended past the repeat sequence to bind.

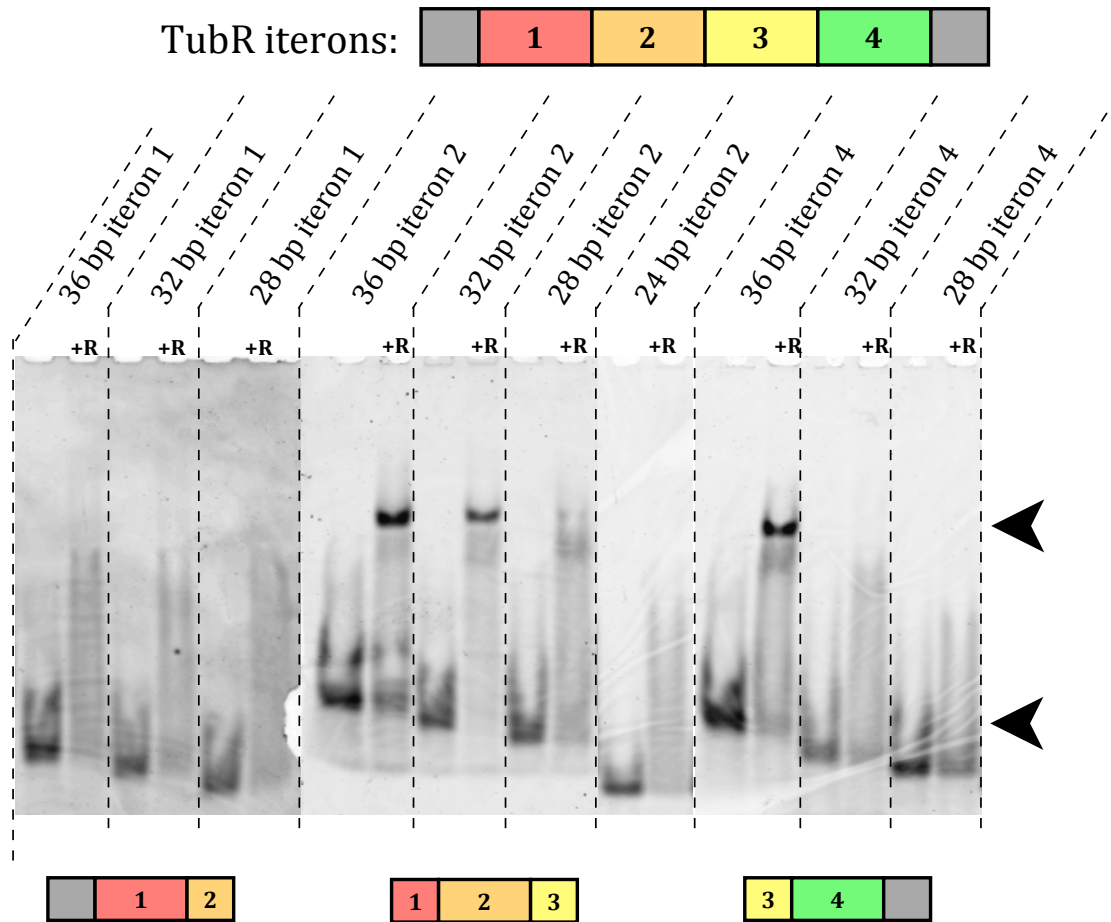


Figure 4. Binding of various lengths of oligonucleotides of the iteron sequences found to be important for TubR binding, indicating that TubR needs flanking residues past the pseudo-repeat sequence for strong binding.

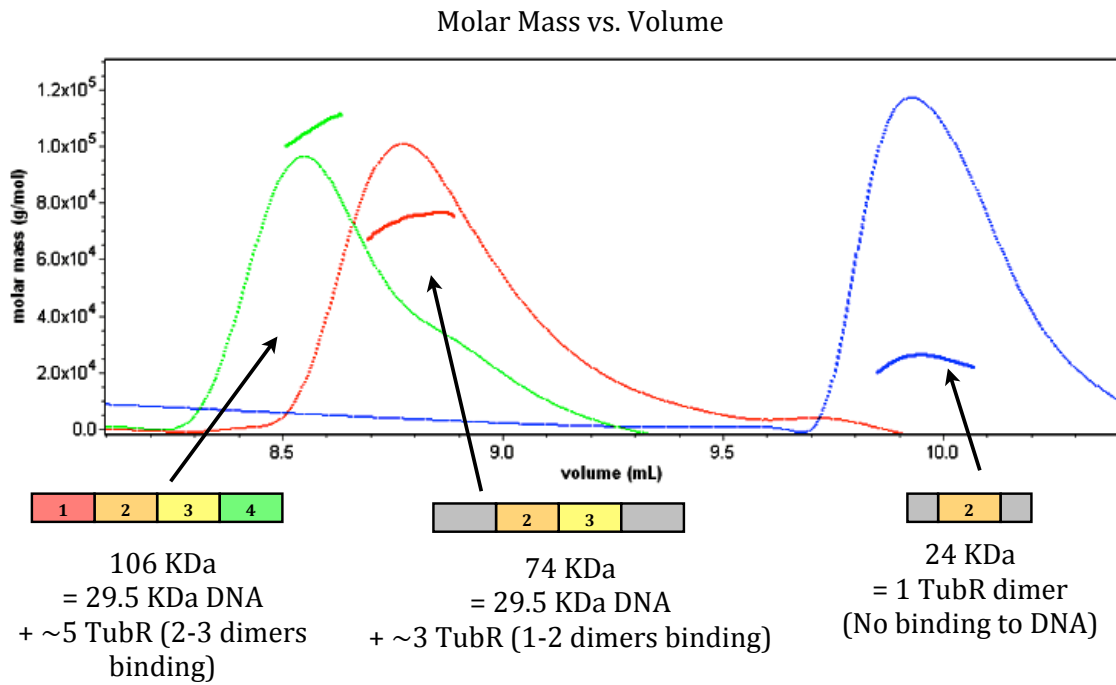


Figure 5. MALS determining number of TubR dimers bound to different *tubC* oligonucleotides.

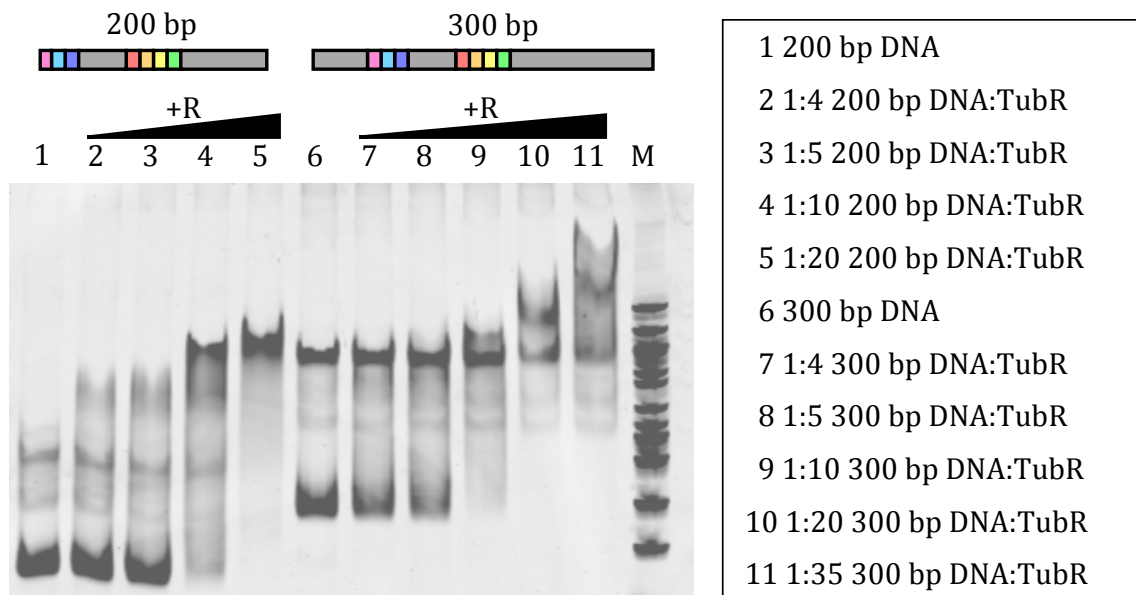


Figure 6. Gel shift assay of TubR binding to longer *tubC* oligonucleotides.

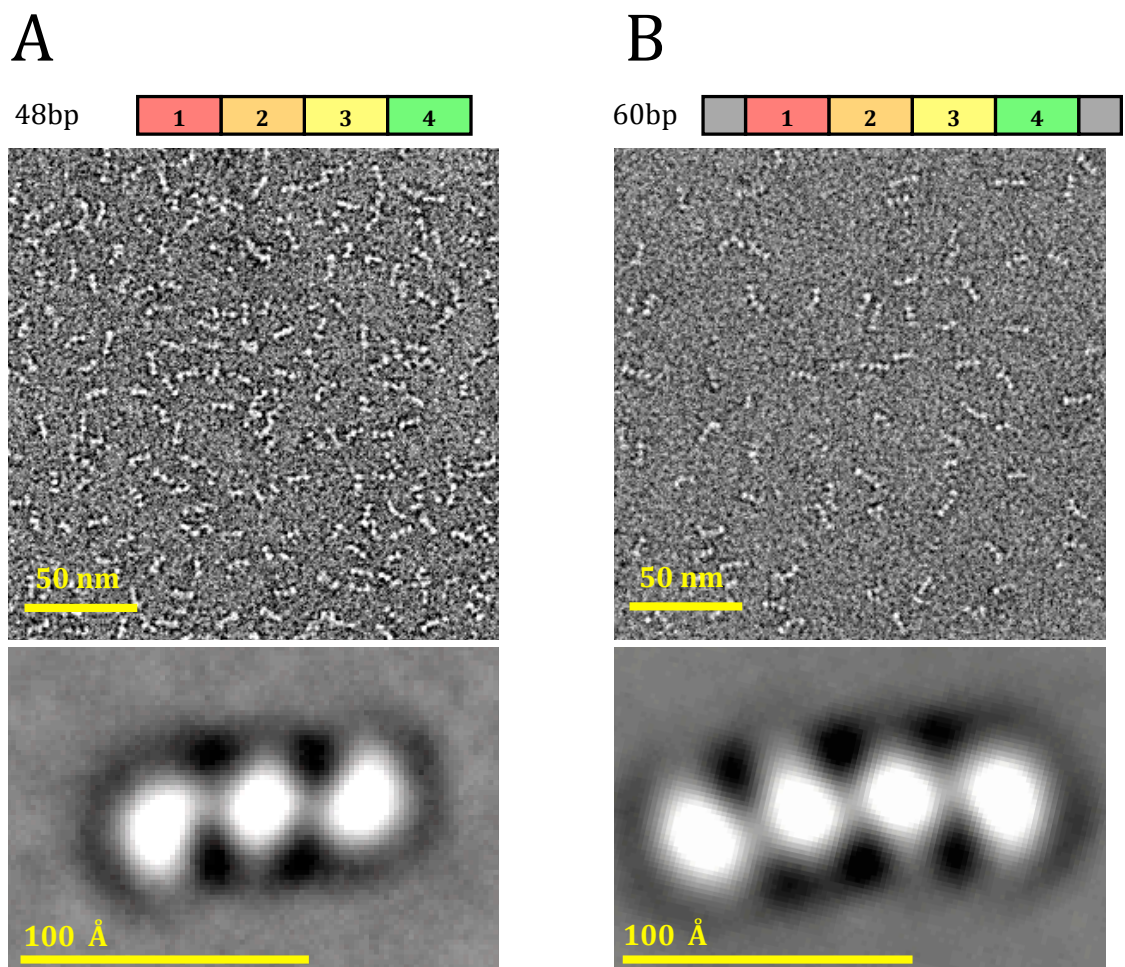


Figure 7. Negative stain EM of TubR dimers binding to 48 or 60 base pair *tubC*. (A) Micrograph and single class average of TubR bound to 48 base pair *tubC* sequence. (B) Micrograph and single class average of TubR bound to 60 base pair *tubC* sequence (48 base pair + 6 base pair flanking).

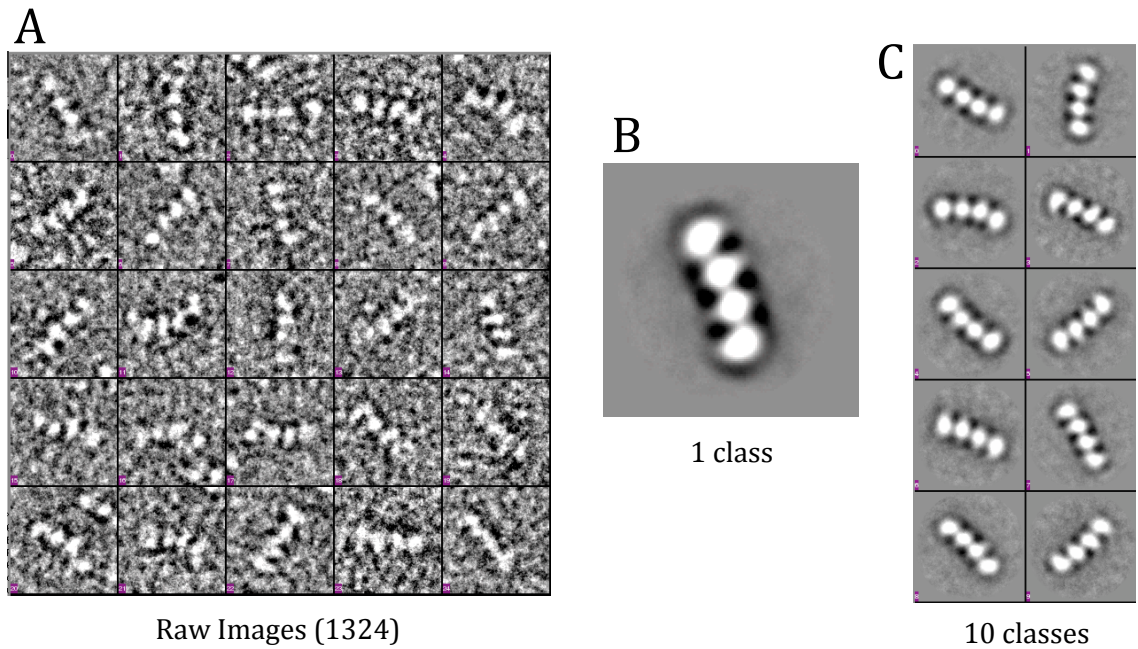


Figure 8. Negative stain EM of TubR dimers binding to 48 bp *tubC*. (A) Select raw images of TubR bound to 60 base pair *tubC* sequence (48 base pair + 6 base pair flanking). (B) Single class average of TubR bound to 60 base pair *tubC* sequence. (C) 10 class averages of TubR bound to 60 base pair *tubC* sequence.

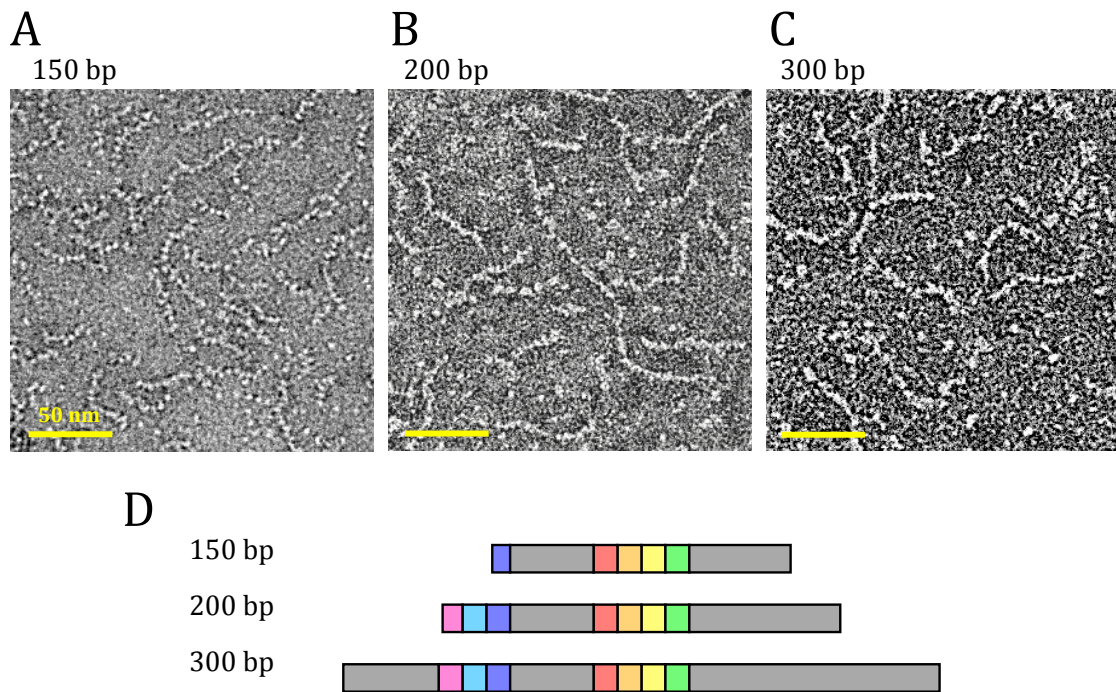


Figure 9. Negative stain EM of TubR dimers binding to longer *tubC* DNA. (A) Micrograph of TubR bound to 150 base pair *tubC* sequence (48 base pairs + 51 base pairs flanking). (B) Micrograph of TubR bound to 200 base pairs *tubC* sequence (48 base pairs + 76 base pairs flanking). (C) Micrograph of TubR bound to 300 base pairs *tubC* sequence (48 base pairs + 126 base pairs flanking). (D) Diagram of different oligonucleotides used vs. found pseudo-atomic repeat regions.

$$\text{Psuedorepeat} = \left(\begin{array}{c} \text{AAAA} \\ \text{TTTCG} \end{array} \text{GTTTAA} \begin{array}{c} \text{AA} \\ \text{CC} \end{array} \right)$$

1 [★] TTAGACATTAAGTTTATATAAATATAGAAG
 31 AATTTTAATAAAAATAAA[★]TAACGGTTTAAA
 61 [★]TTTAAATTTAATTTTAGGGTTTAAATTTCTG
 91 GGGGTTATAGAAAGATATATGTATATCTAG
 121 TGTGGC TAAAGGTTTAAATAACAGTTTAAA
 151 TTTAAGTTTAACTTTTCAGTTTACATACCAT
 181 TCCCAGTGTGATATA^{37bp spacer}AATAGGGTTAGGTGAA
 211 TTTTCCACTCTCA^{dnaA box}AGAATTAATTAACAG
 241 ATGGGAGTTAAACAAT[★]GAATAGGGATCACT
 271 TTTATACGTTAAACATTGCAGAAATTGCAG[★]

[★] Start of TubR/ORF157

Figure 10. Diagram of the sequence surrounding *tubC*, highlighting oligonucleotide limits and other features. Pink stars highlight the limits of the 300 base pair oligonucleotide, green stars denote the limits of the 200 base pair oligonucleotide, and yellow stars denote the end of the 150 base pair oligonucleotide.

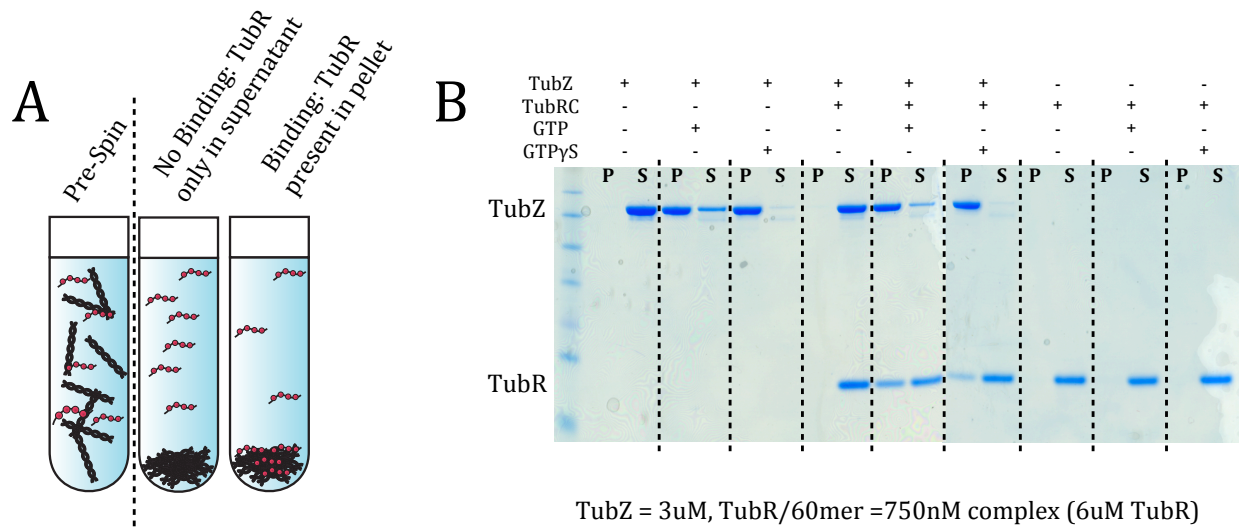


Figure 11. Co-pelleting TubZ-Bt with the TubRC complex. (A) Diagram of expecting results from experiment. (B) Results of pelleting TubRC using 60 base pair *tubC* oligonucleotide with untagged TubZ-Bt.

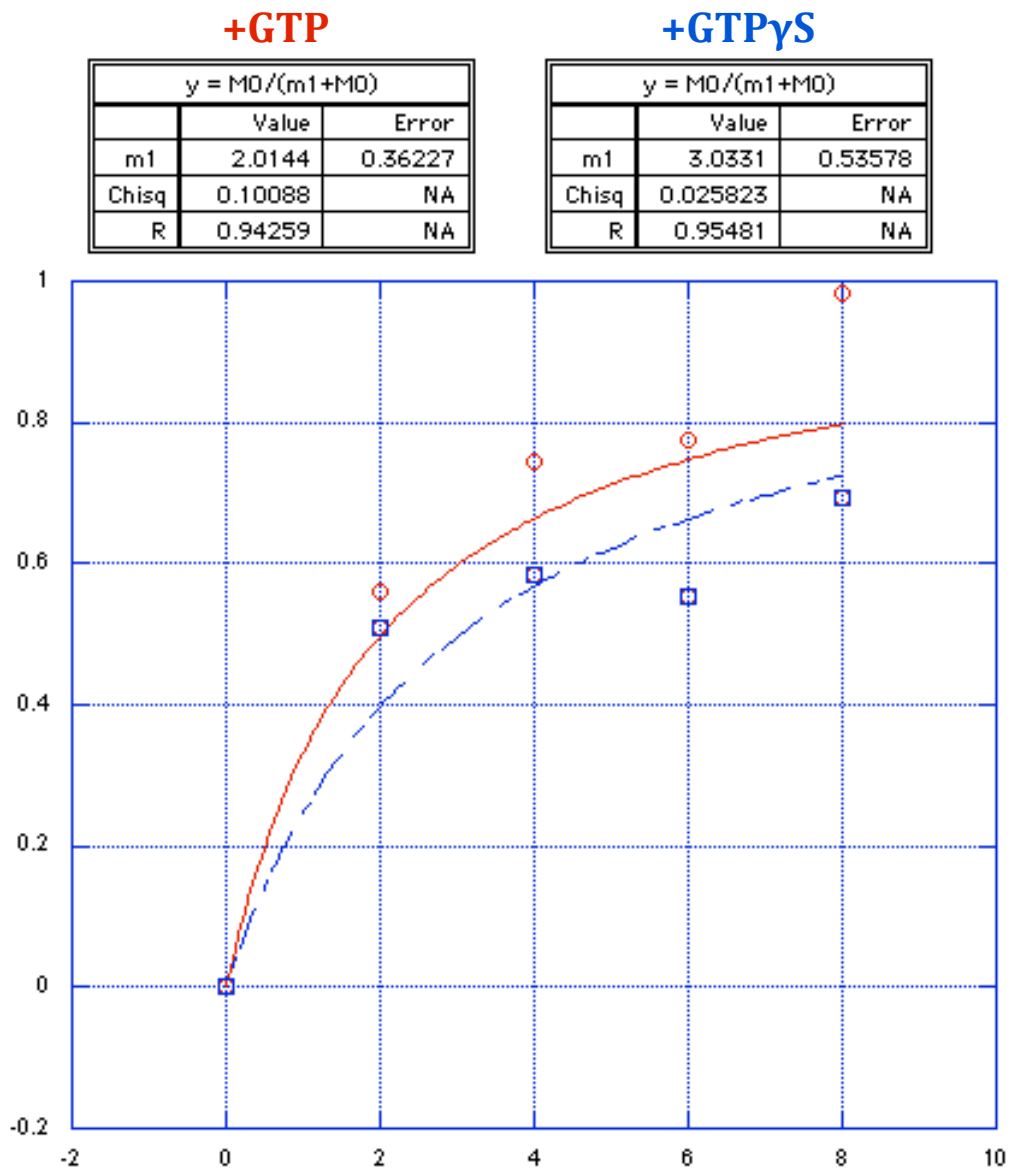


Figure 12. Co-pelleting of untagged TubZ-Bt with TubRC complex (with 60mer). In red, +GTP, in blue +GTPγS.

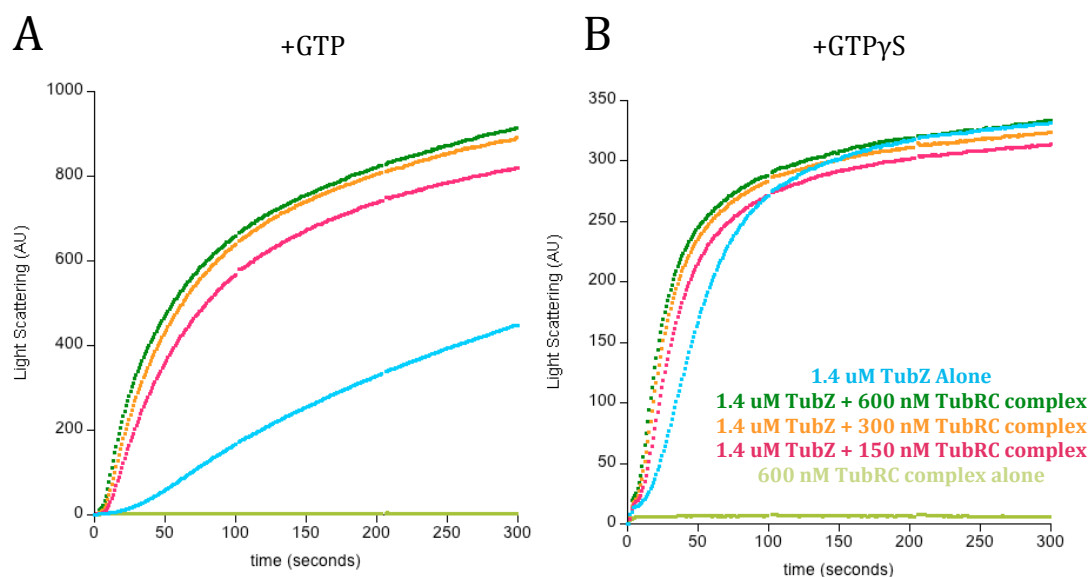


Figure 13. Stimulation of untagged TubZ-Bt polymerization with TubRC-60mer complex.

(A) 90 degree light scattering of 1.4 μ M Untagged TubZ-Bt grown in the presence of GTP alone (blue), or with increasing amounts of TubRC-60mer complex (pink: 150 nM, orange: 300 nM, green: 600 nM), and TubRC-60mer alone (light green). (B) 90 degree light scattering of 1.4 μ M Untagged TubZ-Bt grown in the presence of GTP γ S alone (blue), or with increasing amounts of TubRC-60mer complex (pink: 150 nM, orange: 300 nM, green: 600 nM), and TubRC-60mer alone (light green).

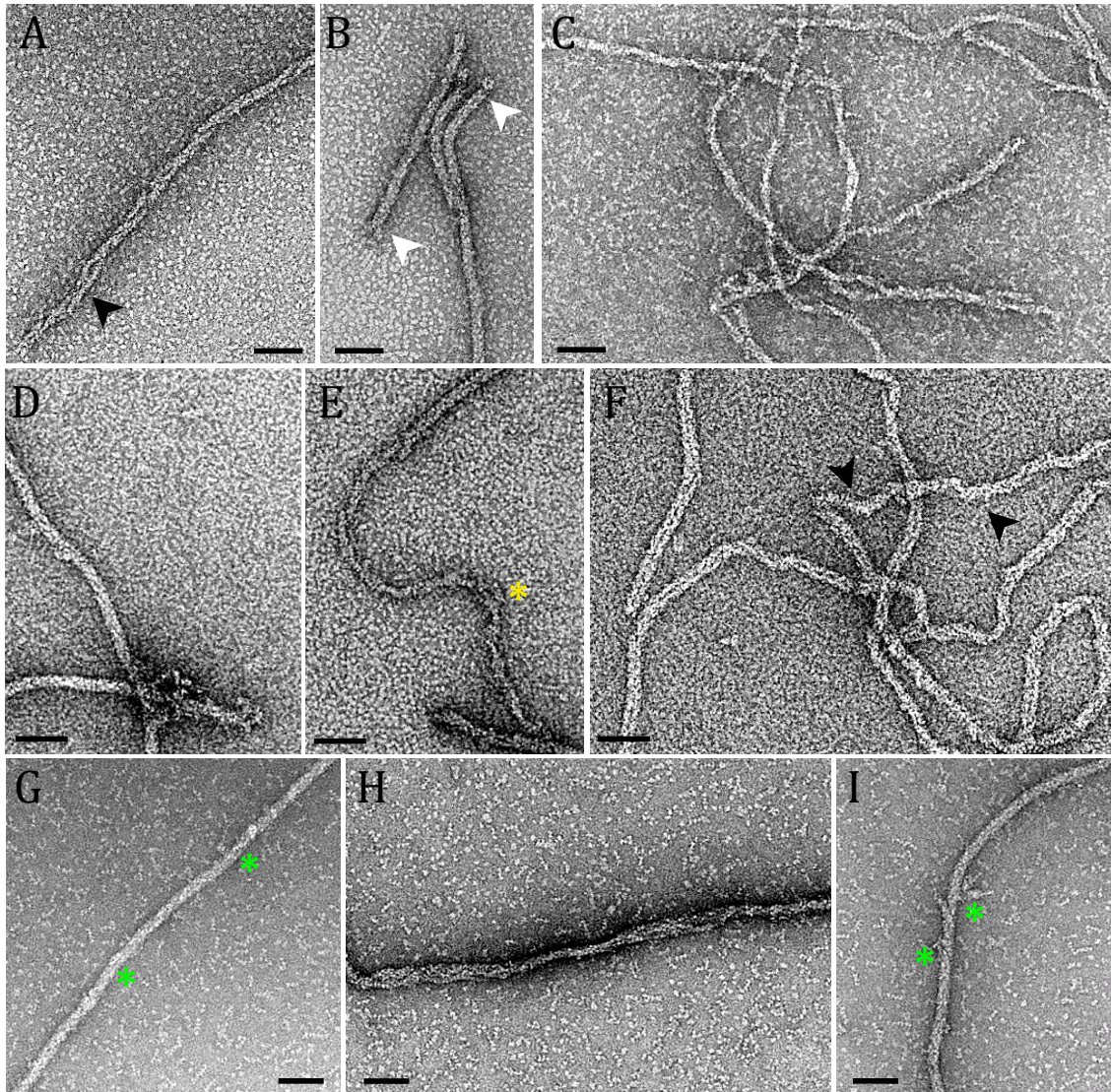


Figure 14. Initial attempts at characterizing the TubRC-TubZ filament interaction. NS EM of (A) TubR:300mer + TubZ:GTP. (B) TubR:plasmid + TubZ:GTP. (C) TubR:60mer + TubZ:GTP γ S. (D-F) Saturating amounts of TubR:60mer +TubZ:GTP. (G-I) TubR:60mer + TubZ:GTP + glutaraldehyde. Scale bar is 50 nm. Black arrows highlight disassembly of TubZ filaments. White arrows show potentially interesting ends. Yellow asterisks show two-stranded filaments in the presence of GTP. Green asterisks highlight potential TubRC complex binding.

References

1. Oliva MA, Martin-Galiano AJ, Sakaguchi Y, & Andreu JM (2012) Tubulin homolog TubZ in a phage-encoded partition system. *Proc Natl Acad Sci U S A* 109(20):7711-7716 .
2. Tanaka T (2010) Functional analysis of the stability determinant AlfB of pBET131, a miniplasmid derivative of bacillus subtilis (natto) plasmid pLS32. *J Bacteriol* 192(5):1221-1230 .
3. Salje J (2010) Plasmid segregation: how to survive as an extra piece of DNA. *Crit Rev Biochem Mol Biol* 45(4):296-317 .
4. Tang M, Bideshi DK, Park HW, & Federici BA (2006) Minireplicon from pBtoxis of *Bacillus thuringiensis* subsp. israelensis. *Appl Environ Microbiol* 72(11):6948-6954 .
5. Tang M, Bideshi DK, Park HW, & Federici BA (2007) Iteron-binding ORF157 and FtsZ-like ORF156 proteins encoded by pBtoxis play a role in its replication in *Bacillus thuringiensis* subsp. israelensis. *J Bacteriol* 189(22):8053-8058 .
6. Aylett CH & Lowe J (2012) Superstructure of the centromeric complex of TubZRC plasmid partitioning systems. *Proc Natl Acad Sci U S A* 109(41):16522-16527 .
7. Ni L, Xu W, Kumaraswami M, & Schumacher MA (2010) Plasmid protein TubR uses a distinct mode of HTH-DNA binding and recruits the prokaryotic tubulin homolog TubZ to effect DNA partition. *Proc Natl Acad Sci U S A* 107(26):11763-11768 .
8. Ludtke SJ, Baldwin PR, & Chiu W (1999) EMAN: semiautomated software for high-resolution single-particle reconstructions. *J Struct Biol* 128(1):82-97 .

Chapter Seven
Future Directions

Introduction

As is the case with much scientific work, the set of experiments presented in this dissertation answer some questions, but from those answers even more questions arise. Much of the work presented will not be published in places other than this dissertation, and there are many avenues that exist to pursue further investigation into the areas opened up here. The field of eukaryotic tubulins has been studied for decades, but there is still much to be discovered. New techniques that have emerged (1-5) will allow more in depth molecular studies of the dynamics and behavior of microtubules to be done. On the other end of the spectrum, most of the prokaryotic and phage tubulins mentioned here have only just been discovered (and much is still unknown about the *in vivo* biology of the most studied prokaryotic tubulin family member, FtsZ). Much work is left to be done to understand both the biological workings and the molecular details of both this new group of tubulin family members and those previously study. Discussed below are some immediate ideas for follow up on the work presented in this dissertation.

Monomeric Eukaryotic Tubulins

Future directions for the study of γ -tubulin

γ -Tubulin remains a very interesting target for study, both to understand the molecular mechanism of other eukaryotic tubulin family members as well as to understand the molecular mechanism of microtubule nucleation. Recently a paper was published demonstrating that GTP hydrolysis is necessary for γ -tubulin function (6). Additional follow-up studies in which we can modify the binding of γ -tubulin as proposed in chapter 3

to preferentially bind a nucleotide other than GTP are still necessary to parse the exact role of hydrolysis in nucleotide.

Attempts to purify yeast γ -tubulin from bacterial cells have been as of yet unproductive, as indicated in this thesis. The best avenues to approach this are to attempt purifying γ -tubulin from a variety of organisms in bacteria, purifying budding yeast γ -tubulin overexpressed in budding yeast, or to purify γ -tubulin from baculovirus/insect cell systems where they have been proven (albeit in low yields). Once a successful system is in place to successfully express and purify γ -tubulin easily in the lab environment, attempts at chemical genetics on the binding site can be attempted.

Future directions for the study of δ - and ϵ -tubulin

δ - and ϵ -tubulin continue to be unstudied *in vitro*, and as of yet there are no known binding partners. In order to pursue an understanding of these proteins' role in forming the B- and C-tubules of centrioles, it is necessary to both establish a method to purify them. As with γ -tubulin, I was unsuccessful in purifying δ - and ϵ -tubulin expressed recombinantly in *E. coli*. Given the similarity of these proteins to γ -tubulin, the best route to successful purification probably lies in using either a baculovirus expression system, or perhaps mammalian cell expression. Alternately you could attempt to purify δ - and ϵ -tubulin from different species other than human, such as those in *Paramecium* or Trypanosomes. These approaches may not be successful, as δ - and ϵ -tubulin may prove to be unstable in the absence of undiscovered binding partners. An important step in understanding their function, and perhaps towards the ability to access biochemical and structural studies is the discovery of potential binding partners. In order to do this, either immunoprecipitation,

from different cell lines, such as human U2OS cells, *Paramecium*, or *C. reinhardtii*. Additionally, these IPs could be performed on extracted centrosomes to enrich for centriolar proteins. New technology using Cas9/CRISPR proteins (7) may also allow us to add affinity tags to δ - and ϵ -tubulin *in vivo* in order to eliminate the need to find an acceptable antibody for immunoprecipitation. Understanding how δ - and ϵ -tubulin function will be an exciting direction in understanding how tubulin family members can form such diverse structures.

Towards an understanding of the plasmid segregation system TubZRC

The main focus of the work presented in this dissertation is on the three-component plasmid segregation TubZRC from pBtoxis found in *B. thuringiensis*. We have made some progress towards understanding this system by revealing an unprecedented morphological change in which the TubZ-Bt filament has an intermediate two-stranded state as an intermediate towards a stable four-stranded filament, which appears to be dependent on hydrolysis state. We have attempted to probe deeper into the interaction between the TubRC DNA-adaptor complex and TubZ, and are able to observe that TubR dimers are able to cooperatively coat *tubC* DNA. Although we have made inroads into understanding how TubZ-Bt works *in vitro*, there are still many aspects of the system that are not understood, and are good avenues for experimentation.

Investigation into the in vitro dynamics of TubZ-Bt

We have been able to investigate both the structure of TubZ-Bt filaments in two different states, and observe the polymerization kinetics of these filaments via bulk

measurements with 90-degree light scattering. However, these bulk measurements may not reveal the true dynamics of TubZ-Bt. Although our current observations would suggest that it is not dynamically unstable like the ParM system (8), it has been reported to treadmill *in vivo* (9). In order to probe the dynamics, we have created c-terminally KCK-tagged TubZ-Bt. This construct can be labeled with both fluorophore and biotin via a maleimide linkage in order to visualize TubZ-Bt under a number of conditions using TIRF microscopy. These observations can be done in the absence and presence of TubRC complex, and should give key insights into how TubZ-Bt moves about the cell in order to segregate plasmids.

Structure of the TubRC complex and its interaction with TubZ-Bt filaments

We were unable to observe any rigid structure to the TubRC complexes observed by negative stain such as has been seen for ParM (10). Aylett and colleagues have observed that TubRC from *B. megaterium* form ring-like structures and propose that perhaps TubRC-Bt needs to bind to TubZ-Bt filaments in order to form a higher order structure (11). In order to probe this, we need to be able to locate TubRC binding along the TubZ-Bt. We have been yet unable to do this, as monitoring by negative stain has proved difficult as it is hard to differentiate TubRC complex from background protein and TubZ filaments. In order to overcome this, we first must apply the TIRF system above, by co-labeling TubR (or *tubC* DNA) with TubZ. We can then monitor the location of TubRC complex along the filament. If it appears that TubRC binds at the end of filaments, we can attempt structural investigation by EM, using methods such as by tomographic sub-averaging, in order to observe the structure of TubZRC. If the complex appears to bind laterally along the TubZ-Bt filament,

we may attempt to observe binding with EM by using gold-labeling onto pieces of *tubC* DNA in order to locate the TubRC complex.

Another possibility for structural observation of the complex is x-ray crystallography or NMR of TubR binding to a peptide of the C-terminal tail of TubZ-Bt. The location at which TubZ-Bt binds to TubRC complex has been characterized to be within the last 80 or so residues (12). However, how and what residues on TubR bind to this region on TubZ is not known.

In addition, it is important to investigate how TubRC affects TubZ filament formation, both by the above investigation using TIRF microscopy to monitor TubZ dynamics, as well as using light scattering to determine whether TubRC complex affects filament nucleation or filament stabilization.

Understanding the mechanism of morphological change between filament states

Although the work presented in chapter four describes the discovery of a unique mechanism by which a four-stranded filament is formed after a transition from transient two-stranded filaments, it remains unclear how this large-scale transition occurs. In order to understand this, higher resolution structures of both the two- and four-stranded structures would be useful. Guidance towards an orthogonal mutation that affects only the two-stranded filament would be of particular use. These higher resolution structures could hopefully be achieved using new EM camera technology, which has already provided higher resolution structures that could be achieved otherwise (13). Additionally it may be intriguing to sort filaments into more subclasses to see if we could capture other transitional steps. It may be possible to target some branched ends to perform tomography

on in hopes of mapping which strands of the four-stranded filament emerge to/from which strands of the two-stranded filament.

Probing the in vivo morphology of TubZ-Bt filaments

Previous tomographic work on TubZ-Bt over expressed in *E. coli* cells indicated that TubZ is a two-stranded helix in cells (14). As we do not have access to the raw data presented in this paper, it is unclear to us whether the data truly indicate this or whether the authors were overly influenced by their assumptions based on their *in vitro* data. Regardless, it is important to understand the morphology of the filaments in the context of their native environment, or at the very least, and a more modest expression level or in the presence of the TubRC complex. One way to approach this problem is to try to perform cryo-tomography in as near native conditions as possible. This can be done by either cryo-sectioning *B. thuringiensis* with native pBtoxis and potentially a low level of overexpressed TubZ, or by whole cell tomography using overexpressed TubZ and TubRC complex in the smaller sized 'mini' *B. subtilis*.

Perhaps a simpler test would be to try to disrupt faithful pBtoxis segregation by overexpression mutants that would disrupt either two- or four-stranded filament formation, using the techniques used previously for testing the hydrolysis dead TubZ D269A (9). TubZ could be overexpressed with several residues or even a GFP or thioredoxin tag on the N-terminus, which should block four-stranded filament formation but not affect two-stranded filament formation. Mutating pBtoxis, which is quite large, can be quite complicated and difficult to do, so even though there are caveats to using simple

overexpression, using many complimentary mutation should help to give us confidence in our results.

TubY: A putative fourth component in plasmid segregation

A study done on a TubZ family protein found in a pseudolysogenic *Clostridial* phage C-st located a putative fourth component to the TubZRC system, which was named TubY. The authors both demonstrated an effect of the TubY protein on the TubZRC system from phage C-st, but also identified putative other TubY proteins in other known TubZRC systems (15). Although the architecture of the TubZRC operon from pBtoxis is not the same as from phage C-st, and it has been shown that the TubZRC region is all that is necessary for pBtoxis segregation (16), it is still possible that TubY may play an interesting complementary role in the pBtoxis segregation machinery. It is most likely trivial to purify the protein identified as a TubY. Although I remain skeptical that this protein plays a role in the TubZRC-Bt system, I believe that TubY-Bt warrants some follow-up investigation.

Comparison with other TubZ family members

It has been suggested in several papers on the TubZRC-Bt system that TubZRC-Bt and the better known ParMRC have reached a convergent evolution (11, 14). Currently published literature shows that TubZ-Bt forms a two-stranded filament (14, 17) that interacts with what may be a helical Adaptor-DNA complex (11). However, as discussed in chapter four, we see that this is in fact not that case, and that at least *in vitro* we see that TubZ-Bt forms predominantly four-stranded filaments in the presence of its native substrate GTP. What is the filament morphology of other TubZ family members? TubZ from

the phage C-st is completely lacking helix H0 which is found in the four-stranded interface, so it remains likely that this in fact a two-stranded filament, as has been reported in the literature (15). However, TubZ from *B. anthracis* was purified with an N-terminal GST tag (17), so that this protein maybe be similarly affected by remaining addition residues. TubZ has also been purified and studied from *B. cereus*. The sequence of this protein is for all intents and purposes identical to TubZ-Ba. The protein purified in the study was not N-terminally tagged, but the negative stain images included in the manuscript do not provide insight into the oligomeric state of the protein (18).

To understand how TubZRC-Bt functions, it is important to understand its similarities and differences from these other TubZ systems. In chapter five, data is shown for preliminary experiments on TubZ from *B. megaterium* indicating that TubZ-Bm filaments may in fact be three stranded. Follow-up work to confirm this and to attempt work with the purified TubRC-Bm complex would be of great interest. Additionally, future work should be done to confirm the oligomeric state of TubZ-Ba/Bc using tagless protein and GTP. Although it would be a nice complement to the work in this dissertation if these proteins were determined to be four-stranded rather than two-stranded, it should not be regarded as evidence of the *in vivo* state of TubZ-Bt if they are not four-stranded.

As evidenced by the variety of bacterial actin homologs such as ParM, AlfA, Alp12 and MamK (discussed in review (19)), these systems can have a high level of diversity. Similar to this diversity, different proteins which have been labeled 'TubZ' can have very similar structures and even operon architecture, but can form a variety of different filaments morphologies and segregate plasmids using wildly different mechanism. Only careful studies both *in vivo* and *in vitro* will reveal the true nature of how proteins classified

as TubZs carry out their role in plasmid segregation machinery, and determine the convergence or divergence of their mechanisms.

References

1. Chacko JV, Zanicchi FC, & Diaspro A (2013) Probing cytoskeletal structures by coupling optical superresolution and AFM techniques for a correlative approach. *Cytoskeleton (Hoboken)* .
2. Howes SC, Alushin GM, Shida T, Nachury MV, & Nogales E (2013) Effects of tubulin acetylation and tubulin acetyltransferase binding on microtubule structure. *Mol Biol Cell* .
3. Johnson V, Ayaz P, Huddleston P, & Rice LM (2011) Design, overexpression, and purification of polymerization-blocked yeast alphabeta-tubulin mutants. *Biochemistry* 50(40):8636-8644 .
4. Mennella V, *et al.* (2012) Subdiffraction-resolution fluorescence microscopy reveals a domain of the centrosome critical for pericentriolar material organization. *Nat Cell Biol* 14(11):1159-1168 .
5. Widlund PO, *et al.* (2012) One-step purification of assembly-competent tubulin from diverse eukaryotic sources. *Mol Biol Cell* 23(22):4393-4401 .
6. Gombos L, *et al.* (2013) GTP regulates the microtubule nucleation activity of gamma-tubulin. *Nat Cell Biol* 15(11):1317-1327 .
7. Jinek M, *et al.* (2013) RNA-programmed genome editing in human cells. *Elife* 2:e00471 .
8. Garner EC, Campbell CS, & Mullins RD (2004) Dynamic instability in a DNA-segregating prokaryotic actin homolog. *Science* 306(5698):1021-1025 .


9. Larsen RA, *et al.* (2007) Treadmilling of a prokaryotic tubulin-like protein, TubZ, required for plasmid stability in *Bacillus thuringiensis*. *Genes Dev* 21(11):1340-1352 .
10. Moller-Jensen J, Ringgaard S, Mercogliano CP, Gerdes K, & Lowe J (2007) Structural analysis of the ParR/parC plasmid partition complex. *Embo J* 26(20):4413-4422 .
11. Aylett CH & Lowe J (2012) Superstructure of the centromeric complex of TubZRC plasmid partitioning systems. *Proc Natl Acad Sci U S A* 109(41):16522-16527 .
12. Ni L, Xu W, Kumaraswami M, & Schumacher MA (2010) Plasmid protein TubR uses a distinct mode of HTH-DNA binding and recruits the prokaryotic tubulin homolog TubZ to effect DNA partition. *Proc Natl Acad Sci U S A* 107(26):11763-11768 .
13. Li X, *et al.* (2013) Electron counting and beam-induced motion correction enable near-atomic-resolution single-particle cryo-EM. *Nat Methods* 10(6):584-590 .
14. Aylett CH, Wang Q, Michie KA, Amos LA, & Lowe J (2010) Filament structure of bacterial tubulin homologue TubZ. *Proc Natl Acad Sci U S A* 107(46):19766-19771 .
15. Oliva MA, Martin-Galiano AJ, Sakaguchi Y, & Andreu JM (2012) Tubulin homolog TubZ in a phage-encoded partition system. *Proc Natl Acad Sci U S A* 109(20):7711-7716 .
16. Tang M, Bideshi DK, Park HW, & Federici BA (2006) Minireplicon from pBtoxis of *Bacillus thuringiensis* subsp. *israelensis*. *Appl Environ Microbiol* 72(11):6948-6954 .
17. Chen Y & Erickson HP (2008) In vitro assembly studies of FtsZ/tubulin-like proteins (TubZ) from *Bacillus* plasmids: evidence for a capping mechanism. *J Biol Chem* 283(13):8102-8109 .

18. Hoshino S & Hayashi I (2012) Filament formation of the FtsZ/tubulin-like protein TubZ from the Bacillus cereus pXO1 plasmid. *J Biol Chem* 287(38):32103-32112 .
19. Ozyamak E, Kollman JM, & Komeili A (2013) Bacterial actins and their diversity. *Biochemistry* 52(40):6928-6939 .

Publishing Agreement

It is the policy of the University to encourage the distribution of all theses, dissertations, and manuscripts. Copies of all UCSF theses, dissertations, and manuscripts will be routed to the library via the Graduate Division. The library will make all theses, dissertations, and manuscripts accessible to the public and will preserve these to the best of their abilities, in perpetuity.

I hereby grant permission to the Graduate Division of the University of California, San Francisco to release copies of my thesis, dissertation, or manuscript to the Campus Library to provide access and preservation, in whole or in part, in perpetuity.

Author Signature  Date 12/18/2013